Multiscale Modeling of Polymer and Ceramic Matrix Composites

by

Christopher Sorini

A Dissertation Presented in Partial Fulfillment
of the Requirements for the Degree
Doctor of Philosophy

Approved November 2021 by the
Graduate Supervisory Committee:

Aditi Chattopadhyay, Chair
Robert K. Goldberg
Yongming Liu
Marc Mignolet
Masoud Yekani-Fard

ARIZONA STATE UNIVERSITY

December 2021

ABSTRACT

Advanced Polymer and Ceramic Matrix Composites (PMCs and CMCs) are currently employed in a variety of airframe and engine applications. This includes PMC jet engine fan cases and CMC hot gas path turbine components. In an impact event, such as a jet engine fan blade-out, PMCs exhibit significant deformation-induced temperature rises in addition to strain rate, temperature, and pressure dependence. CMC turbine components experience elevated temperatures, large thermal gradients, and sustained loading for long time periods in service, where creep is a major issue. However, the complex nature of woven and braided composites presents significant challenges for deformation, progressive damage, and failure prediction, particularly under extreme service conditions where global response is heavily driven by competing time and temperature dependent phenomena at the constituent level. In service, the constituents in these advanced composites experience history-dependent inelastic deformation, progressive damage, and failure, which drive global nonlinear constitutive behavior. In the case of PMCs, deformation-induced heating under impact conditions is heavily influenced by the matrix. The creep behavior of CMCs is a complex manifestation of time-dependent load transfer due to the differing creep rates of the constituents; simultaneous creep and relaxation at the constituent level govern macroscopic CMC creep. The disparity in length scales associated with the constituent materials, woven and braided tow architectures, and composite structural components therefore necessitates the development of robust multiscale computational tools. In this work, multiscale computational tools are developed to gain insight into the deformation, progressive damage, and failure of advanced PMCs and CMCs. This includes multiscale modeling of the impact response of PMCs, including adiabatic heating due to the

conversion of plastic work to heat at the constituent level, as well as elevated temperature creep in CMCs as a result of time-dependent constituent load transfer. It is expected that the developed models and methods will provide valuable insight into the challenges associated with the design and certification of these advanced material systems.

This dissertation is dedicated to my family and friends for their continued and unconditional love and support.

ACKNOWLEDGEMENT

I would like to express my sincere gratitude and appreciation for my advisor, Regents' Professor Aditi Chattopadhyay, who first took me in as an undergraduate volunteer and has since instilled in me a passion for research and teaching, for which I will be forever grateful. I would like to also like to give a special thank you to Dr. Robert K. Goldberg from NASA's Glenn Research Center in Cleveland, OH.

I am also sincerely grateful for the opportunity to work with and learn from the students I have met at my time in the Adaptive Intelligent Materials & Systems (AIMS) Center at Arizona State University (ASU). This includes both past and current students. These people, as well as Dr. Chattopadhyay, have made this experience truly unique, enjoyable, and fun. I would like to give special thanks to the following previous AIMS Center students for their guidance and mentorship when I was an undergraduate volunteer in Dr. Chattopadhyay's lab: Dr. Luke Borkowski, Dr. Jinjun Zhang, Dr. Yingtao Liu.

A special thanks is also extended to Dr. Mike Pereira and Duane Revilock of NASA Glenn Research Center for providing experimental impact test data. I would also like to thank NASA Glenn Research Center for supporting the first portion of my PhD studies through the Harriett G. Jenkins Graduate Fellowship Program Grant #NNX15AU36H, program technical monitor Dr. Robert K. Goldberg.

TABLE OF CONTENTS

Page

LIST OF TABLES

Table Page

LIST OF FIGURES

Figure Page

Figure Page

Figure Page

1 INTRODUCTION

1.1 Background and Motivation

Due to their light weight, high specific strength, stiffness, and toughness, energy absorption capabilities, and elevated temperature stability, advanced woven and braided fiber-reinforced composites are increasingly replacing monolithics in a variety of structural applications with extreme service environments. Two primary examples are the use of braided carbon-fiber reinforced polymer matrix composites (PMCs) in impact-resistant hardwall jet engine fan blade containment structures (Roberts et al., 2009) and the use of woven non-oxide ceramic matrix composites (CMCs) in hot gas path turbine components (Gowayed and Ojard, 2020). The former, per Federal Aviation Agency (FAA) regulations, are required to contain loose fan blades in the event of a blade-out whereas the latter must maintain structural integrity for thousands of hours or more (Naslain, 2004; Lara-Curzio, 1999) in service conditions consisting of many periods/cycles of sustained loading at elevated temperatures followed by intermittent dwell times (i.e., due to repeated use). The weight reduction afforded by the use of braided PMCs over metallic fan cases provides the benefits of increased payload capability, higher thrust to weight ratio, reduced fuel consumption, and ultimately improved aircraft efficiency (Roberts et al., 2009). On the other hand, CMC hot gas path components also provide efficiency benefits, though they do so by operating at the highest possible temperature since turbine thermal efficiency is known to increase with the highest temperature in a cycle (Gowayed and Ojard, 2020). While the plethora of available constituent materials, their many potential architectural/geometric (i.e., woven, braided, etc.) arrangements, and available processing/fabrication methods present the unique opportunity for manufacturers to tailor

these composite systems to meet multiple, and often conflicting, performance requirements, the architectural and thermomechanical constitutive complexity present significant challenges for accurate prediction of deformation, progressive damage, and ultimate failure.

Both PMCs and CMCs exhibit significant macroscopic constitutive nonlinearity and anisotropy due to a combination of damage and/or inelasticity at the constituent level. Damage may appear in the form of tow splitting, fiber/matrix debonding, tow/matrix debonding, and fiber failure. Aerospace epoxies tend to be ductile at high temperatures (relative to the glass transition temperature) and low strain rates and brittle at low temperatures and high strain rates. The elastic properties and saturation stress of the polymer matrix generally increase with decreasing temperature and increasing strain rate. Furthermore, unlike metals, for which plastic deformation is generally considered to be deviatoric (volume preserving), the viscoplastic deformation of polymers is known to be pressure dependent. A manifestation of this pressure dependence is tension-compression asymmetry; the magnitude of the compressive saturation stress is greater than the tensile saturation stress (Kolling et al., 2005; Siviour and Jordan, 2016). As such, inelastic constitutive laws based on the (pressure-independent) von Mises or Hill yield criteria are generally not suitable for plastically dilatant materials, such as polymers, soils, and composites with plastically dilatant matrices. Additionally, high strain rate deformation is not isothermal; as the rate of deformation increases, the rate of heat generation due to plastic deformation is much faster than the characteristic thermal diffusion time, and the thermodynamic condition transitions from isothermal to adiabatic (Garg et al., 2008). For PMCs subjected to ballistic impact events, heat is generated locally within the polymer

matrix due to the conversion of plastic work to heat, but the rapid nature of the impact event does not allow sufficient time for significant heat transfer to occur via conduction, causing adiabatic conditions to prevail. Local deformation-induced temperature rises in an impact event could exceed the matrix glass transition temperature (Johnston et al., 2018), which can lead to substantial thermal softening and subsequent deformation localization if softening effects outweigh strain and strain rate hardening effects (Chiou et al., 2007), and therefore must be accounted for in computational models.

Non-oxide CMCs rely on a weak fiber coating (interphase), typically boron nitride (BN) or pyrolytic carbon (PyC), to deflect matrix cracks and facilitate load transfer between the fibers and matrix, adding pseudo ductility and toughness to what would otherwise be a brittle multiphase material (Gowayed and Ojard, 2020). Damage in woven CMCs can appear at various length scales in the form of intertow and intratow matrix microcracks, fiber-matrix interfacial debonding, and progressive fiber failure. In a woven CMC material subjected to room temperature quasi-static tensile loading, transverse intratow microcracks tend to initiate in the transverse tows at a stress level below the proportional limit (first matrix cracking) stress (Santhosh and Ahmad, 2013). As the load is increased, intertow cracking, splitting, and microcrack growth all contribute to nonlinearity in the stress-strain response before the fibers ultimately fracture, and lead to ultimate failure of the CMC (Santhosh and Ahmad, 2013; Borkowski and Chattopadhyay, 2015). Despite their intrinsic high strength, toughness, quasi-ductility, and ability to maintain structural integrity at elevated temperatures, SiC-fiber-based CMCs are known to creep at temperatures above about 1000-1100℃ (Gauthier and Lamon, 2009; Mital et al., 2018), which is the approximate maximum usage temperature for super alloys (Ohnabe et

al., 1999). Creep is therefore a major source of inelastic deformation in CMCs (Santhosh et al., 2018). In CMCs, when one constituent creeps, it subsequently unloads onto the other more creep-resistant constituents, which can alter any as-produced residual stresses in the composite (Santhosh et al., 2018). Either the fibers or matrix may be the dominant creeping constituent and distinctly different damage modes result depending on whether the fibers unload to the matrix during creep or vice versa.

Both micromechanical and macromechanical approaches have been used to model the nonlinear constitutive behavior of composite materials. In micromechanical approaches, the individual constituents are explicitly modeled; constituent interaction is realized through homogenization, which allows prediction of the effective composite behavior based on the properties, arrangement, and volume fractions of the constituents (Aboudi et al., 2012). The micromechanical approach is advantageous in that it is highly accurate, able to resolve constituent fields, and allows the application of simpler constitutive and damage/failure models (i.e., isotropic) at a more fundamental length scale (constituent level) than the macromechanical approach, which treats the composite as a smeared homogeneous continuum. The macromechanical approach is as advantageous in that it is more computationally efficient than the micromechanical approach and the experimental testing used for model calibration implicitly accounts for all in-situ effects (interface, damage, residual stresses, etc.) (Aboudi et al., 2012). Despite the advantages of macromechanical models, their calibration requires extensive experimental testing (each variation in fiber volume fraction, architecture, orientation, and constituent material properties essentially must be characterized like a new material) and requires the application of more advanced constitutive and damage/failure theories (i.e., anisotropic).

Moreover, the macromechanical approach only tends to work well for fiber dominated loading scenarios and in the linear, isothermal deformation regime (Aboudi et al., 2012).

A practical concern in physics-based computational modeling is the well-known tradeoff between model accuracy and computational efficiency. Multiscale methodologies differ in the way information is passed between the relevant length scales of the problem. This scale-dependent information transfer in computational multiscale modeling is known as scale bridging or "handshaking". Multiscale scale bridging methodologies can be broadly categorized as concurrent, hierarchical, or synergistic (Aboudi et al., 2012; Pineda et al., 2017). Hierarchical models are characterized by an uncoupled one-way ("bottom-up" or "top-down") flow of information across length scales and are the most computationally efficient, but least accurate. Examples of hierarchical scale bridging include: i) effective property determination for subsequent input into finite element (FE) software ("bottom-up"); ii) determination of local/constituent stresses and strains based on FE integration point strain-time histories as a postprocessing step ("top-down"). Despite the efficiency, the uncoupled nature and lack of two-way information transfer between length scales precludes the consideration of path-dependent material nonlinearity, limiting the hierarchical approach to linear elastic constitutive behavior (Aboudi et al., 2012). Concurrent multiscale models represent all constituents in a single model (i.e., concurrently) and involve simultaneous computation at all length scales, resulting in the highest accuracy but lowest computational efficiency of the three scale bridging techniques. Synergistic models provide a compromise between fidelity and efficiency via a two-way flow of information between length scales. Multiscale methodologies, whether hierarchical, synergistic, or concurrent, may be further categorized as analytical (Reuss,

1929; Voight, 1887), semi-analytical (Aboudi et al., 2012), or fully numerical (Feyel, 1999). Analytical methods offer the highest computational efficiency and lowest accuracy whereas numerical methods offer the highest fidelity and lowest efficiency. Semi-analytical micromechanics-based multiscale methods represent a compromise between analytical and numerical approaches and therefore a balance between fidelity and efficiency.

Some of the earliest micromechanics-based multiscale models (analytical linear and semi-analytical nonlinear) were developed by Chamis et al. (Chamis, 1984; Murthy and Chamis, 1986; Chamis and Hopkins, 1988). These models provide simplified micromechanics equations for the prediction of strength, fracture toughness, impact resistance, and environmental effects of multiphase materials in a very computationally efficient manner owing to their simplifying assumptions. The semi-analytical generalized (Paley and Aboudi, 1992; Aboudi, 1995) method of cells (Aboudi, 1989) (GMC), high-fidelity GMC (HFGMC), and their respective efficient reformulations (Pindera and Bednarcyk, 1999; Bansal and Pindera, 2004; Arnold et al., 2004) are micromechanics theories proposed for nonlinear thermomechanical two-scale analyses of thermo-viscoelastic-viscoplastic heterogeneous materials with arbitrary microstructures and are the basis of NASA GRC's MAC/GMC micromechanics analysis code (Bednarcyk and Arnold, 2002). The core of these theories is the determination of strain concentration matrices that relate global strains to local subcell-level strains through enforcement of displacement and traction continuity conditions (in an average sense) between adjacent subcells and adjacent unit cells, the latter of which enforces periodicity. Once global strains are localized to the subcell/constituent level, an arbitrary constitutive law may be used to compute the subcell

stresses, which are homogenized to determine the global stresses. The GMC employs first order subcell field (e.g., displacement and/or temperature) expansions, which result in: i) constant subcell-level stresses, strains, and temperatures; ii) lack of normal-shear coupling in the sense that adjacent subcells do not transfer load to one another via shear. The HFGMC addresses the lack of normal-shear coupling in GMC by employing second-order subcell field expansions (Aboudi et al., 2012), resulting in linearly varying stress, strain and temperature fields at the subcell level. However, the higher accuracy afforded by HFGMC comes at a significant computational expense and additionally results in a mesh size dependence similar to that of the FE method, necessitating a finer spatial discretization to ensure convergence and therefore a higher computational cost. Therefore, based on computational efficiency considerations, GMC is more often used as a constitutive model in continuum-scale progressive damage and life prediction tools due to its computational efficiency despite its lack of normal-shear coupling.

The multiscale GMC (MSGMC) (Liu, 2011; Liu et al., 2011) is a generalization of the GMC to an arbitrary number of length scales, facilitating efficient multiscale analyses of composites with more complex material architectures, such as woven and braided composites. While the lack of normal-shear coupling in MSGMC has been stated to not present significant problems (Aboudi et al., 2012), this is questionable when there are more than two analysis length-scales. For example, when modeling a woven or braided material, MSGMC would not account for normal-shear coupling at the weave/braid level, implying an undulating tow would not experience any shear deformation at the point of undulation when a normal deformation is applied to the woven repeating unit cell (RUC). To circumvent the lack of normal-shear coupling in MSGMC, multi-step homogenization

procedures (Liu, 2011; Liu et al. 2011; Borkowski and Chattopadhyay, 2015) have been employed, the determination of which may not be apparent a-priori. Despite this, MSGMC has been successfully applied to efficiently predict progressive damage and inelastic deformation in woven PMC (Liu et al., 2011) and CMC (Aboudi et al., 2012; Liu et al., 2011; Borkowski and Chattopadhyay, 2015; Skinner and Chattopadhyay, 2021) material systems.

The research presented in this dissertation is focused on the development of robust and computationally efficient multiscale computational models/tools applicable to braided and woven composites under extreme service environments. Particularly, the research is focused on the high strain rate behavior of braided PMCs and elevated temperature CMC creep.

1.2 Objectives

The principal objectives of this work are as follows:

- Develop a robust and computationally efficient synergistic multiscale modeling framework to simulate the architecturally dependent impact response of advanced braided PMCs; approximate heterogeneity at the highest analysis length scale; model effects of local matrix adiabatic heating due to the conversion of plastic work to heat and subsequent thermal softening on macroscopic response
- Develop a thermodynamically consistent polymer constitutive formulation for use in multiscale analyses of PMCs under impact loading that has the following features: 1) Strain rate, temperature, and pressure dependence; 2) Ability to account for tension-compression asymmetry; 3) Nonnegative plastic dissipation (thermodynamic consistency); 4) Exhibits physically realistic plastic flow; 5) Suitable for calibration

against experimental tests conducted over a range of strain rates, temperatures, and loading conditions

- Implement developed PMC constitutive models into commercial transient dynamic FE code LS-DYNA (Hallquist, 2006) to facilitate simulation of PMC coupons and structural components
- Investigate effects of time-dependent constituent load transfer on CMC creep
- Investigate effects of creep-induced constituent stress redistribution on room temperature CMC proportional limit (first matrix cracking) stress level

1.3 Outline

The document is structured as follows:

Chapter 2 discusses the development of a rate-, temperature-, and pressure-dependent unified thermo-viscoplastic constitutive formulation. A new plastic potential function is proposed, and elementary loading conditions are utilized to determine relations between model constants to ensure the potential function is nonnegative, which is shown to guarantee nonnegative plastic work, a necessary thermodynamic requirement. Expressions for the tensile and compressive plastic Poisson's ratios are derived and used to determine bounds on the model constants to ensure physically realistic plastic flow. The components of the inelastic strain rate tensor are modified to explicitly depend on temperature based on the Arrhenius equation for nonisothermal processes. A procedure for the determination of the model constants based on neat epoxy test data is presented. Temperature rises, due to the conversion of plastic work to heat, and subsequent thermal softening are computed via the adiabatic heat energy equation.

In Chapter 3, the unified thermo-viscoplastic polymer constitutive formulation developed in Chapter 2 is implemented into the GMC micromechanics framework (Aboudi et al., 2012) to investigate the effects of matrix adiabatic heating on unidirectional (UD) PMC response. A micromechanics-based multiscale approach is taken used to allow adiabatic heating to be modeled at the constituent level, where it has been experimentally observed to be predominant in resin-rich regions in PMC flat panel impact tests (Johnston et al., 2018). Simulation results indicate significant adiabatic heating in matrix dominated deformation modes. The micromechanics model, including the developed thermo-viscoplastic polymer constitutive formulation, is implemented into the commercial transient dynamic FE code LS-DYNA (Hallquist, 2006) as a user defined material (UMAT) subroutine. An existing subcell-based approach to approximate the heterogeneity of the triaxially braided architecture at the highest analysis length scale is extended to facilitate synergistic multiscale analysis. A methodology to identify and partition the mesoscale composite RUC into an assemblage of mesoscale UD composite subcells, with stacking sequences determined from the braid architecture, is discussed. Serial sectioning and optical microscopy is performed to identify the dimensions and fiber volume fractions of UD plies in the mesoscale subcells. The UMAT is used in the context of the subcell-based approach to simulate quasi-static and flat panel impact experiments conducted on a triaxially braided PMC, using available experimental data for model calibration and validation.

In Chapter 4, a three-dimensional orthotropic viscoplasticity model is formulated based on the Norton-Bailey/Nutting (Norton 1929, Bailey 1935, Nutting 1921, Nutting 1943) creep law, the orthotropic Hill (1948) plastic potential, and the Arrhenius equation

for nonisothermal processes. The three-dimensional viscoplacitity formulation is then used as a constitutive model in the GMC micromechanics framework to simulate the creep deformation of SiC/SiC microcomposites for which experimental data is available in the literature (Rugg et al., 1999). The viscoplasticity formulation is then used to investigate the effects of time-dependent constituent load transfer, fiber-matrix creep mismatch ratio (Holmes and Chermant, 1993), and fiber volume fraction on CMC creep deformation. Lastly, a computational study is conducted to investigate the effects of creep-induced constituent load redistribution on the room temperature proportional limit stress.

The final chapter discusses the contributions made in this dissertation as well as plans for future work.

2 STRAIN RATE, TEMPERATURE, AND PRESSURE DEPENDENT UNIFIED VISCOPLSATIC POLYMER CONSTITUTIVE MODEL

2.1 Introduction

Due to their excellent energy absorption capability, carbon fiber reinforced PMCs are often used in aerospace applications such as jet engine fan blade containment systems that are subjected to high velocity impact loading in the event of blade-out. The energy is absorbed through various complicated deformation and damage mechanisms, some of which are difficult to detect experimentally. A thorough understanding of the material response under dynamic conditions is therefore required for the assurance of structural reliability and safety of composites in such mission critical components. To this end, physics based constitutive models that span the relevant length scales and capture key deformation, damage, and failure mechanisms in an impact event are indispensable tools that could expedite the design and certification timeline of impact resistant PMC structures.

The development of predictive computational models for PMCs under impact loading conditions is complicated by the inherent material heterogeneity and anisotropy, the multiscale nature (i.e., disparity of length scales associated with constituent materials, tows, braid/weave architecture, and structural components), and complex interactions between the fiber reinforcement and the strain rate, temperature, and pressure dependent polymer matrix. Unlike metals, for which inelastic deformation is generally considered to be deviatoric (volume preserving and pressure independent), the inelastic deformation of polymers, and therefore of PMCs, is known to be pressure dependent (Kolling et al., 2005; Siviour and Jordan, 2016). Additionally, high rate deformation is not isothermal, as is often erroneously assumed. It is well known that a portion of the work required to inelastically

deform polymeric materials is dissipated as heat (Chou et al., 1973; Arruda et al., 1995; Rittell, 1999; Garg et al., 2008), particularly at high strain rates. Under quasi-static conditions, where the duration of loading is large compared to the characteristic thermal diffusion time, heat generated locally due to plastic dissipation has sufficient time to diffuse throughout (and convect away from) the deforming body, which remains in an isothermal condition. As the rate of deformation increases, the rate of heat generation gradually exceeds the rate of heat loss due to conduction/convection, resulting in a gradual temperature rise in the material. Under high rate deformation, where the duration of loading is negligible compared to the characteristic thermal diffusion time, there is insufficient time for significant heat transfer to occur. Adiabatic conditions can therefore often be assumed for dynamic loading (Li and Lambros, 2001; Kendall and Siviour, 2013; Trojanowski et al., 1997; Garg et al., 2008; Chou et al., 1973). Local adiabatic temperature rises, which could exceed the matrix glass transition temperature (Johnston et al., 2018), cause thermal softening (Arruda, et al. 1995, Garg et al. 2008, Rittell 1999) and a potentially substantial effect on the high rate constitutive behavior of polymers and PMCs if the effects of thermal softening outweigh the effects of strain and strain rate hardening (Li and Lambros, 2001; Chiou et al., 2007; Walley et al., 1989).

To model the high strain rate behavior of PMCs, Thiruppukuzhi and Sun (1998) used a three-dimensional (3D) pressure-dependent quadratic plastic potential, assuming transverse isotropy and no plasticity in the fiber direction. The potential is characterized by one parameter. Rate dependence is accounted for by using a three-parameter power law viscoplasticity model. It is noted that, though the 3D plastic potential function is pressure dependent, the assumption of transverse isotropy results in a pressure-independent

potential (Thiruppukuzhi and Sun, 1998). Weeks and Sun (1998) used the Chen and Sun (1993) 3D plastic potential to develop two 3D rate-dependent plasticity models. The authors assume no plasticity in the fiber direction and transverse isotropy, which reduces the potential to that used by Thiruppukuzhi and Sun (1998). Rate dependence was modeled using both a two-parameter power law model and a viscoplasticity model similar to the Johnson-Cook (Meyers, 1994) model. Robinson et al. (1994) and Robinson and Binienda (2001) extended the isotropic unified viscoplastic Bodner-Partom (Bodner and Partom, 1975) model to account for transverse isotropy and hydrostatic stress dependence by proposing an effective stress that depends on pressure and other invariants that reflect transverse isotropy. Bounds on material constants were determined by considering natural stress states for the model. While pressure-dependent, none of the aforementioned models are able to account for the tension-compression asymmetry characteristic of polymeric deformation since they are all based on quadratic plastic potential functions that are even functions of hydrostatic stress.

Yokozeki et al. (2007) proposed a simple extension to the one-parameter Sun and Chen (1989) model to incorporate tension-compression asymmetry. This was done by adding a hydrostatic pressure term (and an associated model constant) to the effective stress given by Sun and Chen (1989). An extra term was also added into the square root term in the effective stress to enforce nonnegativity of the plastic potential. The model (Yokozeki et al., 2007) is applicable to quasi-static plane stress loading conditions. Starting with a generalized anisotropic yield function, Wang and Xiao (2017a) took a similar approach to Yokozeki et al. (2007) and extended the one-parameter Sun and Chen (1989) model to capture tension-compression asymmetry. The model, which incorporates a parameter

representing the ratio of transverse tensile to transverse compressive yield stress, is rate dependent, but is limited to plane stress conditions. The model was later extended by the authors to be fully 3D (Wang and Xiao, 2017b).

In addition to the well known strain rate-, temperature- and pressure-dependence of polymeric deformation, experimental results have indicated significant heat generation can accompany the high rate deformation of polymers. While Kolsky (1949) and Davies and Hunter (1963) were some of the first researchers to investigate the effects of dynamic loading on polymeric material response, the work of Chou et al. (1973) is largely regarded as the first attempt at measuring heat generation in polymers due to mechanical deformation. Chou and coworkers (Chou et al., 1973) tested four hard plastics across a range of strain rates and measured deformation-induced temperature rises using thermocouples. Rittell (1999) used embedded thermocouples to investigate temperature rises due to inelastic deformation of polycarbonate at high strain rates, reporting temperature rises up to 40°C. Garg et al. (2008) used infrared imaging techniques to measure temperature rises in an amorphous thermoplastic and a thermoset epoxy during high strain rate compression, reporting a significant portion of post yield work to be dissipated as heat. These results imply the high rate deformation of polymers is not isothermal, as is often erroneously assumed. Despite the aforementioned experimental studies, the effects of thermomechanical coupling and subsequent thermal softening on the high-rate deformation of PMCs is still not well understood. In one available study, Johnston and coworkers (Johnston et al., 2018) conducted a series of flat panel impact tests (ASTM, 2017) on two [0°/60°/–60°] triaxially braided PMC material systems, T700/PR520 and T700/3502. The two material systems, which consisted of the same high-strength Toray T700

triaxially braided carbon fiber reinforcement, exhibited drastically different behavior under impact conditions due to the different thermoset matrix materials; PR520 is a ductile resin with a thermoplastic toughening phase whereas 3502 is a more brittle, untoughened material system. The T700/PR520 material exhibited highly localized damage near the impact zone accompanied by significant local adiabatic heating in resin rich regions; local temperature rises greater than the matrix glass transition temperature were observed. However, the T700/3502 material system exhibited a much more diffuse damage morphology and more modest temperature rises for similar impact velocities. Though there was less visible impact damage in the T700/3502 material, post impact test C-scan results (Johnston et al., 2018) indicated the T700/3502 system exhibited drastically more barely visible impact damage (BVID), indicating a widespread shattering of the 3502 matrix. Additionally, while the T700/PR520 system exhibited higher in-plane strengths than the T700/3502 system under quasi-static loading, the T700/3502 exhibited a higher ballistic limit, and therefore is capable of absorbing more energy than the T700/PR520 system under impact conditions. It is evident that there are competing hardening and softening mechanisms at play; the material response is highly dependent on whether the effects of strain and strain rate hardening outweigh thermal softening in the matrix material. Given these nonintuitive results, physics based multiscale computational models are necessary to gain a better understanding of the role of deformation-induced heating in PMCs under impact conditions. The work of Johnston et al. (2018) largely motivated the work presented in the current and next chapter of this dissertation.

Since the mechanical properties of carbon fiber are much less sensitive to rate and temperature compared to typical polymer matrix materials, the rate and temperature

dependence of carbon fiber reinforced PMCs is primarily a manifestation of the rate and temperature dependence of the matrix constituent. Moreover, given the aforementioned experimental evidence regarding deformation-induced heat generation, the dynamic behavior of polymers and therefore PMCs is clearly not isothermal. Thus, in order to develop predictive models for the high strain rate response of PMCs, it is necessary to accurately model heat generation in the polymer matrix due to the conversion of plastic work to heat. However, multiscale modeling approaches that consider local deformation-induced heat generation on the high rate deformation of PMCs are significantly missing from the literature. In one available study, Bednarcyk et al. (2019) developed a higher-order two-way thermomechanically coupled multiscale micromechanics model to investigate the impact response of carbon/epoxy and SiC/Ti composites, where the Bodner-Partom (Bodner and Partom, 1975) viscoplastic model was employed to model the viscoplastic response of the epoxy and Ti matrices, respectively. The Bodner-Partom (Bodner and Partom, 1975) model has a single isotropic state variable to represent isotropic hardening and uses an effective stress based on the J_2 flow potential and is, therefore, pressure independent and incapable of simulating tension-compression asymmetry of the epoxy matrix of the carbon/epoxy composite considered (Bednarcyk et al., 2019). Additionally, Bednarcyk et al. (2019) report negative plastic work, which is thermodynamically inconsistent (Allen, 1991; Chow and Lu, 1989; Faria et al., 1998; Kawai et al., 2010; Laudau et al., 1960).

Goldberg et al. (2005) extended the Bodner-Partom (Bodner and Partom, 1975) model to include hydrostatic stress effects to enable simulation of the strain rate and pressure dependent viscoplastic deformation of polymers, including tension-compression

asymmetry. The description of this model (Goldberg et al., 2005) is intentionally kept brief here, as it is described in detail later in this chapter.

In this chapter, several improvements are made to the Goldberg model (Goldberg et al., 2005) to facilitate its use in a multiscale framework to investigate the effects of local adiabatic heating on the high strain rate behavior of PMCs. The model is extended to i) incorporate temperature-dependent viscoplastic flow; ii) more accurately account for the tension-compression asymmetry observed in the response of polymeric materials; iii) ensure physically realistic plastic flow (plastic Poisson's ratios); iv) ensure thermodynamic consistency (nonnegative plastic dissipation). A new plastic potential function is proposed, where two newly introduced constants control the level of influence of hydrostatic stress on viscoplastic deformation. Elementary loading conditions are utilized to derive relations between these hydrostatic constants to enforce the thermodynamic requirement of nonnegative plastic power density, which are then used to derive bounds on thermodynamically admissible values of the plastic Poisson's ratio. The proposed plastic potential function allows independent specification of the tensile and compressive plastic Poisson's ratios and is capable of simulating the nonisochoric plastic deformation characteristic of polymers. This allows calibration of the extended model against pure shear, uniaxial tensile, and uniaxial compressive test data, which is generally not possible in the original Goldberg model (Goldberg et al., 2005). Based on the Arrhenius equation for nonisothermal processes, the components of the inelastic strain rate tensor are modified to explicitly capture temperature dependence. A calibration procedure is described to facilitate identification of all model parameters. The constitutive model is then calibrated against available Epon 862 (E862) epoxy resin pure shear, uniaxial tensile, and uniaxial

compressive data (Gilat et al., 2007; Littell, 2008; Littell et al., 2008) from tests conducted over a range of strain rates and temperatures. Temperature rises due to the conversion of plastic work to heat are computed via the adiabatic heat energy equation, where the proposed model extensions are demonstrated to preclude thermodynamically inconsistent predictions of negative plastic power density; i.e., the thermodynamic consistency introduced via the proposed extensions guarantees plastic deformation can only lead to an increase in temperature. A methodology based on shifting neat resin DMA data with strain rate and temperature is used to approximate the rate and temperature dependence of elastic properties, which allows the simulation of thermal softening (i.e., reduction in elastic properties) due to adiabatic heating. The ability of the modified constitutive model to capture thermal softening associated with plastically deforming polymers at high rates of strain is demonstrated by simulating the high strain rate pure shear, uniaxial tensile and uniaxial compressive response of E862 epoxy over a range of strain rates and temperatures.

2.2 Description of the Goldberg Viscoplastic Constitutive Model

The unified Bodner-Partom (Bodner and Partom, 1975) state variable viscoplastic constitutive model, which was originally developed to model viscoplastic deformation in metals above one half of their melting temperature, was modified by Goldberg et al. (2005) to include hydrostatic stress effects. As aforementioned, a manifestation of this pressure dependence is the difference in tensile and compressive saturation stresses (Siviour and Jordan, 2016). The Goldberg model (Goldberg et al., 2005) is unified in the sense that no distinction is made between creep strain and plastic strain (Bhattachar and Stouffer, 1993); instead, a single (unified) inelastic strain that is assumed to be very small during elastic deformation is used for all levels of stress. Unlike classical rate-independent plasticity

models, unified viscoplasticity models do not employ a defined yield surface or load-unload conditions. Instead, rate dependent saturation and nonlinearity is controlled by the evolution of state variables that are defined represent the average effects of various deformation mechanisms. The governing equations of the Goldberg (Goldberg et al., 2005) model are shown below to facilitate discussion of the extensions made in this chapter.

$$\dot{\varepsilon}_{ij}^{I} = 2D_0 exp\left[-\frac{1}{2}\left(\frac{Z}{\sigma_e}\right)^{2n}\right]\left(\frac{s_{ij}}{2\sqrt{J_2}} + \alpha\delta_{ij}\right) \tag{2.2-1}$$

$$f = \sqrt{J_2} + \alpha\sigma_{kk} \tag{2.2-2}$$

$$\sigma_e = \sqrt{3}f = \sqrt{3J_2} + \sqrt{3}\alpha\sigma_{kk} \tag{2.2-3}$$

$$\dot{Z} = q(Z_1 - Z)\,\dot{e}_e^I \tag{2.2-4}$$

$$\dot{\alpha} = q(\alpha_1 - \alpha)\,\dot{e}_e^I \tag{2.2-5}$$

$$\dot{\varepsilon}_e^I = \dot{e}_e^I = \sqrt{\frac{2}{3}\dot{e}_{ij}^I\dot{e}_{ij}^I} \tag{2.2-6}$$

$$\dot{e}_{ij}^I = \dot{\varepsilon}_{ij}^I - \frac{\dot{\varepsilon}_{kk}^I}{3}\delta_{ij} \tag{2.2-7}$$

$$J_2 = \frac{1}{2}s_{ij}s_{ij} \tag{2.2-8}$$

$$s_{ij} = \sigma_{ij} - \frac{\sigma_{kk}}{3}\delta_{ij} \tag{2.2-9}$$

In Equations 2.2-1 through 2.2-9, $\dot{\varepsilon}_{ij}^I$ are the components of the inelastic strain rate tensor, f is the plastic potential function, n is a constant that controls strain rate sensitivity, D_0 is a constant that represents the maximum inelastic strain rate, α is a time-dependent state variable that controls the influence of hydrostatic stress effects, Z is a time-dependent state variable that represents the resistance to internal stress (captures strain hardening), q is a material constant that controls the hardening rate, σ_{ij} are the components of the Cauchy stress tensor, $\dot{\varepsilon}_{kk}^I$ is the trace of the inelastic strain rate tensor, $\dot{e}_{ij}^I$ are the components of

the deviatoric inelastic strain rate tensor, σ_e is the effective stress, and $\dot{\varepsilon}_e^I = \dot{e}_e^I$ is the effective deviatoric inelastic strain rate. Summation convention on dummy indices is assumed to apply. It is noted that the expression for the effective inelastic strain rate $\dot{\varepsilon}_e^I$ was determined (Goldberg et al., 2005) via the principal of the equivalence of plastic power density, i.e., $\dot{W}^I = \sigma_{ij}\dot{\varepsilon}_{ij}^I = \sigma_e\dot{\varepsilon}_e^I$, which states that the tensor product (full contraction) of the Cauchy stress tensor and the inelastic strain rate tensor must be equal to the product of the scalar effective stress and effective inelastic strain rate. The symbol $\dot{e}_e^I$ is utilized to indicate the effective inelastic strain rate in the Goldberg (Goldberg et al., 2005) model is only a function of the deviatoric inelastic strain rate tensor components. While the original Bodner-Partom (Bodner and Partom, 1975) model is based on the pressure-independent J_2 flow potential, the extension proposed by Goldberg (Goldberg et al., 2005) accounts for pressure-dependence via the $\alpha\sigma_{kk}$ term in the plastic potential (Equation 2.2-2) and the $\alpha\delta_{ij}$ term in the expression for the inelastic strain rate tensor components (Equation 2.2-1). The state variables Z and α evolve in time with the effective deviatoric inelastic strain rate, $\dot{e}_e^I$, according to Equations 2.2-4 and 2.2-5. The hydrostatic state variable, α, allows the model to capture the tension-compression asymmetry typical in polymeric deformation by allowing the plastic potential function to take on different values in tension and compression. Overall, the model requires the determination of seven state variables, D_0, n, Z_0, Z_1, q, α_0, and α_1. Further details of the model and its derivation can be found in Goldberg et al. (2005).

While the Goldberg model has been shown to be capable of predicting the rate dependent response over a variety of thermoset epoxies over a range of strain rates, several extensions are required to facilitate its use to predict local matrix adiabatic heating in a

PMC impact problem. First, the model in its current state is isothermal. However, temperature dependence is necessary because regions associated local adiabatic heating in PMCs subjected to impact loading are unknown a-priori. In a numerical simulation, these temperatures must be computed based on the local stress state, the inelastic strain rate as well as thermal properties (density and specific heat). These local adiabatic temperature rises due to the conversion of inelastic work to heat result in thermal softening of the elastic properties as well as the inelastic properties. As such, explicit temperature dependence must be incorporated. The second issue that must be addressed is that, once the model (Goldberg et al., 2005) is calibrated based on experimental pure shear and uniaxial tensile stress-strain data, there is no way to characterize the model to match compressive stress-strain data; the model is capable of modeling tension-compression asymmetry, but there is no way to independently control the magnitudes of the tensile and compressive saturation stresses due to the single hydrostatic state variable. An implication of this that will be discussed in greater detail later in this chapter is that physically realistic values of the tensile plastic Poisson's ratio correspond to physically unrealistic values of the compressive plastic Poisson's ratio and vice-versa. Lastly, and of most importance for the present goal of predicting local matrix adiabatic heating, it was discovered that, under certain loading conditions, negative plastic work density could result. This is problematic because, according to the second law of thermodynamics, the inelastic work rate density must be nonnegative (Allen, 1991; Chow and Lu, 1989; Faria et al., 1998; Kawai et al., 2010; Laudau et al., 1960). Negative plastic dissipation implies a decrease in temperature due to inelastic deformation, which is nonphysical. It is therefore essential to prevent this

possibility to ensure thermodynamic consistency of the model for general multiaxial loading. These extensions are described in the next section.

2.3 Improved Viscoplastic Model Formulation

2.3.1 Isothermal Governing Equations

A new piecewise plastic potential function that is dependent upon the first invariant of the Cauchy stress tensor, $I_1 = \sigma_{kk}$, and the second invariant of the deviatoric stress tensor, J_2, is defined as follows:

$$f = \begin{cases} \sqrt{J_2} + A\sigma_{kk} & if\ \sigma_{kk} \neq 0\ and\ J_2 \neq 0 \\ \sqrt{J_2} & if\ \sigma_{kk} = 0\ and\ J_2 \neq 0 \\ A\sigma_{kk} & if\ \sigma_{kk} \neq 0\ and\ J_2 = 0 \end{cases} \tag{2.3-1a}$$

where $$A = (\sqrt{\gamma} sign(\sigma_{kk}) + \xi) \tag{2.3-1b}$$

In Equation 2.3-1b, γ & ξ are constants that control the influence of hydrostatic stress on plastic deformation. The hydrostatic constant γ is defined to be nonnegative whereas the sign of the hydrostatic constant ξ is not restricted. The implications of positive, negative, and zero valued ξ is discussed later in this chapter. As in the Goldberg model (Goldberg et al., 2005), an associative flow rule is used, where the components of the inelastic strain rate tensor, $\dot{\varepsilon}_{ij}^{I}$, are assumed to be equal to the product of the partial derivative of the plastic potential function, f, with respect to the components of the Cauchy stress tensor, σ_{ij}, and the scalar rate of the plastic multiplier, $\dot{\lambda}$, as follows:

$$\dot{\varepsilon}_{ij}^{I} = \dot{\lambda} \frac{\partial f}{\partial \sigma_{ij}}. \tag{2.3-2}$$

Evaluating the partial derivative of the plastic potential function with respect to the components of the Cauchy stress tensor shown in Equation 2.3-2 results in the following:

$$\frac{\partial f}{\partial \sigma_{ij}} = \begin{cases} \frac{s_{ij}}{2\sqrt{J_2}} + A\delta_{ij} & if\ \sigma_{kk} \neq 0\ and\ J_2 \neq 0 \\ \frac{s_{ij}}{2\sqrt{J_2}} & if\ \sigma_{kk} = 0\ and\ J_2 \neq 0 \\ A\delta_{ij} & if\ \sigma_{kk} \neq 0\ and\ J_2 = 0 \end{cases} \tag{2.3-3}$$

In Equation 2.3-3, s_{ij} are the components of the deviatoric stress tensor and δ_{ij} is the Kronecker delta. The reason for employing a piecewise plastic potential function is because the partial derivative of $\sqrt{J_2} + A\sigma_{kk}$ with respect to σ_{ij} is not defined for pure shear, $\sigma_{kk} = 0$ and $J_2 \neq 0$, (derivative of sign function is undefined when its argument is zero: $\frac{\partial A}{\partial \sigma_{ij}} = \frac{\partial}{\partial \sigma_{ij}}(\sqrt{\gamma} sign(\sigma_{kk}) + \xi) = 0$ when $\sigma_{kk} \neq 0$) or purely hydrostatic loading, $\sigma_{kk} \neq 0$ and $J_2 = 0$ (division by $J_2 = 0$). The piecewise definition of the plastic potential also prevents plastic dilation under pure shear loading. The rate of the plastic multiplier, $\dot{\lambda}$, is obtained by substituting Equation 2.3-3 into Equation 2.3-2 and taking the tensor product of the inelastic strain rate tensor with itself. The result is shown in Equation 2.3-4.

$$\dot{\lambda} = \begin{cases} \sqrt{\frac{2\dot{\varepsilon}^I_{ij}\dot{\varepsilon}^I_{ij}}{1 + 6A^2}} & if\ \sigma_{kk} \neq 0\ and\ J_2 \neq 0 \\ \sqrt{2\dot{\varepsilon}^I_{ij}\dot{\varepsilon}^I_{ij}} & if\ \sigma_{kk} = 0\ and\ J_2 \neq 0 \\ \sqrt{\frac{\dot{\varepsilon}^I_{ij}\dot{\varepsilon}^I_{ij}}{3A^2}} & if\ \sigma_{kk} \neq 0\ and\ J_2 = 0 \end{cases} \tag{2.3-4}$$

In Equation 2.3-4, $\dot{e}^I_{ij}$ and are the components of the deviatoric inelastic strain rate tensor, $\dot{e}^I_{ij} = \dot{\varepsilon}^I_{ij} - \frac{1}{3}\dot{\varepsilon}^I_{kk}\delta_{ij}$, and $\dot{\varepsilon}^I_{kk}$ is the trace of the inelastic strain rate tensor. Next, the effective stress is defined as:

$$\sigma_e = \sqrt{3}f = \begin{cases} \sqrt{3J_2} + \sqrt{3}A\sigma_{kk} & if\ \sigma_{kk} \neq 0\ and\ J_2 \neq 0 \\ \sqrt{3J_2} & if\ \sigma_{kk} = 0\ and\ J_2 \neq 0 \\ \sqrt{3}A\sigma_{kk} & if\ \sigma_{kk} \neq 0\ and\ J_2 = 0 \end{cases} \quad (2.3\text{-}5)$$

It is evident from Equation 2.3-5 that, under pure shear loading, or if the hydrostatic constants γ and ξ are both equal to zero, the effective stress simplifies to the classical definition of $\sqrt{3J_2}$, which reduces to the applied stress for uniaxial tensile loading and to the absolute value of the applied stress for uniaxial compressive loading. The effective inelastic strain rate, $\dot{\varepsilon}_e^I$, is determined through the principle of the equivalence of plastic work rate density:

$$\dot{W}^I = \sigma_{ij}\dot{\varepsilon}_{ij}^I = \sigma_e\dot{\varepsilon}_e^I \geq 0 \quad (2.3\text{-}6)$$

By combining Equations 2.3-2 and 2.3-3, substituting the result as well as the effective stress (Equation 2.3-5) into Equation 2.3-6, the effective inelastic strain rate is determined and is shown in Equation 2.3-7.

$$\dot{\varepsilon}_e^I = \begin{cases} \sqrt{\dfrac{2\dot{\varepsilon}_{ij}^I\dot{\varepsilon}_{ij}^I}{3(1+6A^2)}} & if\ \sigma_{kk} \neq 0\ and\ J_2 \neq 0 \\ \sqrt{\dfrac{2}{3}\dot{\varepsilon}_{ij}^I\dot{\varepsilon}_{ij}^I} & if\ \sigma_{kk} = 0\ and\ J_2 \neq 0 \\ \dfrac{\sqrt{\dot{\varepsilon}_{ij}^I\dot{\varepsilon}_{ij}^I}}{3|A|} & if\ \sigma_{kk} \neq 0\ and\ J_2 = 0 \end{cases} \quad (2.3\text{-}7)$$

Note that if the hydrostatic constants are set to zero, the value of A given by Equation 2.3-1b is also zero. In this case, $\dot{\varepsilon}_e^I$ should be set to zero for the $\sigma_{kk} \neq 0$ and $J_2 = 0$ case in a numerical code to avoid division by zero in the third expression of Equation 2.3-7. By defining

$$\frac{\sqrt{3}}{2}\dot{\varepsilon}_e^I = D_0 exp\left[-\frac{1}{2}\left(\frac{Z}{\sigma_e}\right)^{2n}\right] \tag{2.3-8}$$

based on the work of Bodner and Partom (1975) and Bodner (2001), substituting the rate of the plastic multiplier back into Equation 2.3-2, and simplifying, the inelastic strain rate tensor components are obtained:

$$\dot{\varepsilon}_{ij}^I = \begin{cases} 2D_0 exp\left[-\frac{1}{2}\left(\frac{Z}{\sigma_e}\right)^{2n}\right]\left(\frac{s_{ij}}{2\sqrt{J_2}} + A\delta_{ij}\right) & if\ \sigma_{kk} \neq 0\ and\ J_2 \neq 0 \\ 2D_0 exp\left[-\frac{1}{2}\left(\frac{Z}{\sigma_e}\right)^{2n}\right]\left(\frac{s_{ij}}{2\sqrt{J_2}}\right) & if\ \sigma_{kk} = 0\ and\ J_2 \neq 0 \\ 2D_0 exp\left[-\frac{1}{2}\left(\frac{Z}{\sigma_e}\right)^{2n}\right]\left(A\delta_{ij}\right) & if\ \sigma_{kk} \neq 0\ and\ J_2 = 0 \end{cases} \tag{2.3-9}$$

In Equations 2.3-8 and 2.3-9, n is a constant that controls strain rate sensitivity (as n increases, rate dependence decreases), D_0 is a constant scale factor that represents the maximum inelastic strain rate, and Z is a scalar state variable that represents the resistance to internal stress (captures isotropic hardening). The state variable Z evolves from its initial value of Z_0 to its final value of Z_1, where $Z_1 > Z_0$, according to the following expression:

$$\dot{Z} = q(Z_1 - Z)\dot{\varepsilon}_e^I \tag{2.3-10}$$

It is noted that an effective stress of zero implies no inelastic deformation; to prevent division by zero (in Equation 2.3-9) in a numerical code, the components of the inelastic strain rate tensor (Equation 2.3-9) should be set to zero in this case. The expressions for the inelastic strain rate given by Equation 2.3-9 are isothermal. The next section discusses the nonisothermal extension of the model.

2.3.2 Nonisothermal Governing Equations - Temperature Dependent Viscoplastic Plastic Flow

To account for the temperature dependence of the saturation stress, the components of the inelastic strain rate tensor are modified to explicitly capture temperature dependence based on the Arrhenius equation for nonisothermal processes (Bhattachar and Stouffer, 1993), which states that the inelastic strain rate is proportional to the exponential of the dimensionless expression $\left(\frac{-\mathrm{Q}}{\mathrm{KT}}\right)$, as follows

$$\dot{\varepsilon}^{I} \; \alpha \; exp\left(\frac{-Q}{KT}\right) \tag{2.3-11}$$

where Q is the activation energy, K is Boltzmann's constant, and T is the absolute temperature. By inserting the dimensionless expression $\left(\frac{-\mathrm{Q}}{\mathrm{KT}}\right)$ into the exponential term in the original expression for the components of the inelastic strain rate tensor (Bhattachar and Stouffer, 1993), Equation 2.3-9, and defining a new state variable $\bar{\mathrm{Z}}$ as

$$\bar{Z} = \frac{QZ}{K}, \tag{2.3-12}$$

the new temperature-dependent components of the inelastic strain rate tensor are expressed as

$$\dot{\varepsilon}_{ij}^{I} = \begin{cases} 2D_0 ex\,p\left[-\frac{1}{2}\left(\frac{\bar{Z}}{T\sigma_e}\right)^{2n}\right]\left(\frac{S_{ij}}{2\sqrt{J_2}} + A\delta_{ij}\right) & if\ \sigma_{kk} \neq 0\ and\ J_2 \neq 0 \\ 2D_0 ex\,p\left[-\frac{1}{2}\left(\frac{\bar{Z}}{T\sigma_e}\right)^{2n}\right]\left(\frac{S_{ij}}{2\sqrt{J_2}}\right) & if\ \sigma_{kk} = 0\ and\ J_2 \neq 0 \\ 2D_0 ex\,p\left[-\frac{1}{2}\left(\frac{\bar{Z}}{T\sigma_e}\right)^{2n}\right]\left(A\delta_{ij}\right) & if\ \sigma_{kk} \neq 0\ and\ J_2 = 0 \end{cases} \tag{2.3-13}$$

where $\bar{\mathrm{Z}}$ is a temperature-dependent state variable that controls the resistance to internal stress at a given temperature, and the other parameters were defined previously. The

components of the inelastic strain tensor are computed by integrating the components of the inelastic strain rate tensor (Equation 2.3-13) forward in time. Even though polymers can exhibit large deformations, especially at low strain rates and at temperatures close to or above their glass transition temperature, infinitesimal strain theory has been assumed to apply, which permits the additive decomposition of the total strain tensor into its respective elastic, inelastic, and thermal components. This is justified because the intended application for the unified viscoplastic constitutive formulation is multiscale modeling of the high-rate deformation of PMCs, where finite strains in the matrix are not expected. Based on the work of Bhattachar and Stouffer (1993) it is assumed that $\bar{Z}$ evolves in the same way as Z, that is,

$$\dot{\bar{Z}} = q(\bar{Z}_1 - \bar{Z})\dot{\varepsilon}_e^I \tag{2.3-14a}$$

which can be integrated in time to yield

$$\bar{Z} = \bar{Z}_1 - (\bar{Z}_1 - \bar{Z}_0)exp\,(-q\varepsilon_e^I), \tag{2.3-14b}$$

where q is a constant that controls the hardening rate and $\bar{Z}_0$ & $\bar{Z}_1$ are the temperature-dependent initial and final values of $\bar{Z}$, respectively. Under isothermal conditions, Equations 2.3-14a and 2.3-14b are identical. However, under nonisothermal conditions, Equation 2.3-14b should be used instead of Equation 2.3-14a to allow the value of $\bar{Z}_0$ to change with temperature (Bhattachar and Stouffer, 1993; Bhattachar, 1991). It is noted that the dimension of the hardening state variable Z in the Goldberg model (Goldberg et al., 2005) is stress whereas the dimension of $\bar{Z}$ is stress times absolute temperature (Kelvin).

2.3.3 Bounds on Hydrostatic Constants

By examining Equation 2.3-7, it is apparent that the effective inelastic strain rate, $\dot{\varepsilon}_e^I$, is always nonnegative. According to the second law of thermodynamics, plastic power density (Equation 2.3-6) must be nonnegative (Allen, 1991; Chow and Lu, 1989; Faria et al., 1998; Kawai et al., 2010; Laudau et al., 1960). Since plastic power density (Equation 2.3-6) is equal to the product of the scalar effective stress (Equation 2.3-5) and scalar effective inelastic strain rate (Equation 2.3-7), a relationship between γ and ξ must be determined to ensure the effective stress is also nonnegative. To this end, hydrostatic tensile and compressive load cases are considered. For hydrostatic tensile loading ($\boldsymbol{\sigma} = \text{diag}([\sigma, \sigma, \sigma])$), the effective stress is:

$$\sigma_e = 3\sqrt{3\gamma}\sigma + 3\sqrt{3}\xi\sigma \geq 0 \tag{2.3-15}$$

For hydrostatic compressive loading ($\boldsymbol{\sigma} = \text{diag}([-\sigma, -\sigma, -\sigma])$), the effective stress is:

$$\sigma_e = 3\sqrt{3\gamma}\sigma - 3\sqrt{3}\xi\sigma \geq 0 \tag{2.3-16}$$

According to Equations 2.3-15 and 2.3-16, the effective stress, and therefore the plastic power density (Equation 2.3-6), will always be nonnegative as long as the following condition is satisfied:

$$-\sqrt{\gamma} \leq \xi \leq \sqrt{\gamma} \tag{2.3-17}$$

The next section explains the implications of the inequality given by Equation 2.3-17 in regards to thermodynamically admissible values of plastic Poisson's ratios.

2.3.4 Plastic Poisson's Ratios

To obtain physically realistic transverse plastic strains in uniaxial tensile and compressive loading, it is useful to derive expressions for the tensile and compressive

plastic Poisson's ratios. For *uniaxial* loading in the 1-direction, the plastic Poisson's ratio is defined as:

$$\nu^p = \frac{-\dot{\varepsilon}_{22}^i}{\dot{\varepsilon}_{11}^i} = \frac{-\dot{\varepsilon}_{33}^i}{\dot{\varepsilon}_{11}^i} = -\frac{\left(\frac{s_{22}}{2\sqrt{J_2}} + A\right)}{\left(\frac{s_{11}}{2\sqrt{J_2}} + A\right)} \tag{2.3-18}$$

Since the signs of the hydrostatic stress and deviatoric stress components are opposite for uniaxial tensile and compressive loading, the tensile and compressive plastic Poisson's ratios, $\nu^{p,T}$ and $\nu^{p,C}$, can, in general, be different and are defined as follows:

$$\nu^{p,T} = -\frac{\left(\frac{s_{22}^{UT}}{2\sqrt{J_2}} + A_{UT}\right)}{\left(\frac{s_{11}^{UT}}{2\sqrt{J_2}} + A_{UT}\right)} = \frac{\sqrt{3} - 6A_{UT}}{2\sqrt{3} + 6A_{UT}} \tag{2.3-19a}$$

$$A_{UT} = \sqrt{\gamma} + \xi \tag{2.3-19b}$$

$$\nu^{p,C} = -\frac{\left(\frac{s_{22}^{UC}}{2\sqrt{J_2}} + A_{UC}\right)}{\left(\frac{s_{11}^{UC}}{2\sqrt{J_2}} + A_{UC}\right)} = \frac{\sqrt{3} + 6A_{UC}}{2\sqrt{3} - 6A_{UC}} \tag{2.3-20a}$$

$$A_{UC} = -\sqrt{\gamma} + \xi \tag{2.3-20b}$$

In Equations 2.3-19 and 2.3-20, "UT" denotes uniaxial tensile loading whereas "UC" denotes uniaxial compressive loading. By manipulating Equations 2.3-19a and 2.3-20a, expressions for A_{UT} and A_{UC} in terms of the tensile and compressive plastic Poisson's ratios are obtained:

$$A_{UT} = \frac{-(s_{11}^{UT}\nu^{p,T} + s_{22}^{UT})}{2\sqrt{J_2}(1 + \nu^{p,T})} = \frac{\sqrt{3} - 2\sqrt{3}\nu^{p,T}}{6(1 + \nu^{p,T})} \tag{2.3-21}$$

$$A_{UC} = \frac{-(s_{11}^{UC}\nu^{p,C} + s_{22}^{UC})}{2\sqrt{J_2}(1+\nu^{p,C})} = \frac{-(\sqrt{3} - 2\sqrt{3}\nu^{p,C})}{6(1+\nu^{p,C})} \tag{2.3-22}$$

To determine the bounds on the tensile and compressive plastic Poisson's ratios, consider Equations 2.3-17, 2.3-19b, and 2.3-20b. Equations 2.3-19b and 2.3-20b can be solved for ξ and $\sqrt{\gamma}$ to yield $\sqrt{\gamma} = \frac{1}{2}(-A_{UC} + A_{UT})$ and $\xi = \frac{1}{2}(A_{UC} + A_{UT})$, respectively. Combining Equations 2.3-19b and 2.3-20b with Equation 2.3-17 implies $A_{UC} \leq 0$ and $A_{UT} \geq 0$, which imply, based on Equations 2.3-19a and 2.3-20a, $\nu^{p,C} \leq 0.5$ and $\nu^{p,T} \leq 0.5$. By evaluating the limit of $\nu^{p,T}$ (Equation 2.3-19a) as A_{UT} tends to infinity and the limit of $\nu^{p,C}$ (Equation 2.3-20a) as A_{UC} tends to negative infinity, the lower bounds of the tensile and compressive plastic Poisson's ratios are obtained to be negative one (-1). Nonnegative plastic power density therefore implies $-1 < \nu^{p,C} \leq 0.5$ and $-1 < \nu^{p,T} \leq 0.5$. It is interesting to note that these are the same bounds as on the elastic Poisson's ratio for an isotropic material, except the tensile and compressive plastic Poisson's ratios can be equal to 0.5 (as is the case in deviatoric plasticity models) whereas the elastic Poisson's ratio cannot since it would result in an infinite bulk modulus. Note that for $0 \leq \nu^{p,C} \leq 0.5$ and $0 \leq \nu^{p,T} \leq 0.5$, $-\frac{\sqrt{3}}{6} \leq \mathrm{A} \leq \frac{\sqrt{3}}{6}$.

There are a several special cases of the model that merit a brief discussion. A pressure independent model is obtained by setting both hydrostatic constants equal to zero ($\gamma = \xi = 0$). In this case, the effective stress reduces to the von Mises effective stress ($\sqrt{3\mathrm{J}_2}$), which implies the plastic deformation is deviatoric (tensile and compressive plastic Poisson's ratios are equal to 0.5) and the tensile and compressive saturation stresses are equal. A

temperature dependent version of the Goldberg model (Goldberg et al., 2005) is obtained by setting γ equal to zero ($\xi \neq 0$); this should not be done, as the model will inherent the same deficiencies as the original model (Goldberg et al., 2005). A pressure-dependent model that does not exhibit tension-compression asymmetry is obtained by setting ξ equal to zero ($\gamma \neq 0$). In this case, the tensile and compressive yield stresses and plastic Poisson's ratios are equal; $\gamma \geq 0$ ensures $-1 < \nu^{p,C} \leq 0.5$ and $-1 < \nu^{p,T} \leq 0.5$ whereas $0 \leq \gamma \leq \frac{1}{12}$ ensures $0 < \nu^{p,C} \leq 0.5$ and $0 < \nu^{p,T} \leq 0.5$.

2.3.5 Tension-Compression Asymmetry

Plasticity formulations that employ plastic potential functions that are even functions of hydrostatic pressure are capable of simulating nonisochoric deformation, but incapable of simulating tension-compression asymmetry. For tension-compression asymmetry, the value of the effective stress in uniaxial tension should be greater than the value of the effective stress in uniaxial compression for the same absolute value of applied uniaxial stress. In other words, a greater uniaxial stress would need to be applied in tension, σ^{UT}, than in compression, σ^{UC}, to achieve equivalent values of the effective stress. Using Equation 2.3-5, this can be expressed as:

$$\sigma_e = \sigma^{UT}\left(1 + \sqrt{3}A_{UT}\right) = \sigma^{UC}\left(1 - \sqrt{3}A_{UC}\right) \tag{2.3-23}$$

Therefore, for tension-compression asymmetry ($\sigma^{UC} > \sigma^{UT}$), $A_{UC} > -A_{UT}$, which implies the hydrostatic constant $0 < \xi < \sqrt{\gamma}$.

2.3.6 Summary of Constraints on Model Parameters and Special Cases

The conditions for nonnegative plastic dissipation, tension-compression asymmetry, and model special cases are summarized in Table 2.3.1.

Table 2.3.1: Conditions for Nonnegative Plastic Dissipation, Tension-Compression Asymmetry, and Model Special Cases	
Condition	**Remark**
$-\sqrt{\gamma} \leq \xi \leq \sqrt{\gamma}$	Nonnegative plastic power density
$0 < \xi < \sqrt{\gamma}$	Nonnegative plastic power density and tension-compression asymmetry
$\xi = \sqrt{\gamma}$	Plastically incompressible in compression
$\xi = \gamma = 0$	Pressure independent model; deviatoric plastic strain tensor; equal uniaxial tensile and compressive saturation stresses
$\gamma \neq 0, \xi = 0$	Pressure dependent model with no tension-compression asymmetry
$\gamma = 0, \xi \neq 0$	Deficient model; possibility of negative plastic power density and plastic Poisson's ratios that are out of bounds

2.4 Adiabatic Heating

The heat energy equation, which expresses the relationship between mechanical deformation and spatial-temporal temperature change, is as follows

$$k\nabla^2 T - \alpha_M(3\lambda + 2\mu)T\dot{\varepsilon}^e_{kk} + \beta\boldsymbol{\sigma}:\dot{\boldsymbol{\varepsilon}}^{\boldsymbol{I}} = \rho C\dot{T} \qquad (2.4\text{-}1)$$

where k is the thermal conductivity, T is the absolute temperature, α_M is the coefficient of thermal expansion, λ and μ are Lame's constants, $\dot{\varepsilon}^e_{kk}$ is the elastic volumetric strain rate, $\boldsymbol{\sigma}$ is the Cauchy stress tensor, $\dot{\boldsymbol{\varepsilon}}^I$ is the inelastic strain rate tensor, ρ is the density, C is the specific heat, and β is the inelastic heat fraction, which represents the fraction of inelastic work converted to heat. As aforementioned, the intended application of the unified viscoplastic constitutive formulation is in multiscale analyses of PMCs subjected to impact loading, where the assumption of adiabatic conditions is generally reasonable (Li and Lambros 2001, Kendall and Siviour 2013, Trojanowski 1997, Garg et al. 2008, Chou et al. 1973). It is useful to derive a characteristic thermal diffusion time to justify the assumption

of adiabatic conditions for high rate loading. To this end, consider the one-dimensional heat (diffusion) equation:

$$k\frac{\partial^2 T}{\partial \mathrm{x}^2} = \rho C\frac{\partial T}{\partial t}. \tag{2.4-2}$$

By replacing the partial derivatives in Equation 2.4-2 with finite differences, the following expression is obtained for the characteristic thermal diffusion time, Δt_d,

$$\Delta t_d = \frac{(\Delta x)^2}{D}, \tag{2.4-3}$$

where D is the thermal diffusivity ($D = \frac{k}{\rho C}$) and Δx is a characteristic length, which can be taken as the distance between the center of the deforming region of a test specimen and the nearest heat sink (Arruda et al., 1995). If the time over which a given experiment takes place is small compared to the characteristic thermal diffusion time, adiabatic conditions can be assumed to prevail (Li and Lambros, 2001; Kendall and Siviour, 2013; Trojanowski, 1997; Garg et al., 2008; Chou et al., 1973) and the conduction term in Equation 2.4-1 can be neglected. The characteristic thermal diffusion time can also be used to compute an approximate strain rate at which the system would be expected to behave adiabatically, Δt_d^{-1}. More details regarding the characteristic thermal diffusion time for E862 resin are given in later in this chapter. The thermoelastic term in Equation 2.4-1 is often negligible compared to the thermoplastic term (Li and Lambros, 2001; Varghese and Batra, 2009; Pan et al., 2016; Siviour and Jordan, 2016), reducing the heat energy equation to:

$$\beta\boldsymbol{\sigma}\colon\dot{\boldsymbol{\varepsilon}}^{\boldsymbol{I}} = \rho C\dot{T}. \tag{2.4-4}$$

Assuming the inelastic heat fraction, β, is known, either measured experimentally or assumed, Equation 2.4-4 can be integrated in time to compute the temperature change due

to the conversion of plastic work to heat at each timestep in an incremental solution procedure.

2.5 Temperature and Strain Rate Dependence of Elastic Properties

It is well known that polymers exhibit an increased stiffness and reduced strain to failure when the applied rate of loading is increased. Since the mechanical properties of carbon fiber are much less sensitive to rate and temperature compared to the epoxy, the rate and temperature dependence of carbon fiber reinforced PMCs is primarily a manifestation of the rate and temperature dependence of the matrix constituent. For this reason, material properties backed out based on quasi-static test data will not suffice to describe the material response under dynamic loading. Thus, a methodology to rapidly determine the elastic properties of the polymer matrix over a broad range of strain rates and temperatures is necessary.

A time-temperature shifting methodology, similar to the Decompose-Shift-Reconstruct (DSR) method originally developed by Mulliken and Boyce (2006), is utilized to compute temperature and strain rate dependent shifts in elastic moduli based on dynamic mechanical analysis (DMA) tests conducted on neat resin at various frequencies. Since the frequency at which a DMA test is conducted corresponds to a particular strain rate (depending on the specimen geometry), rate-dependent shifts in the shear modulus can therefore be obtained by conducting DMA tests at various frequencies and performing a temperature sweep. A schematic of the shifting of the shear storage modulus versus temperature curve with strain rate is shown in Figure 2.5-1 for E862 epoxy DMA data available in the literature (Gilat et al., 2007).

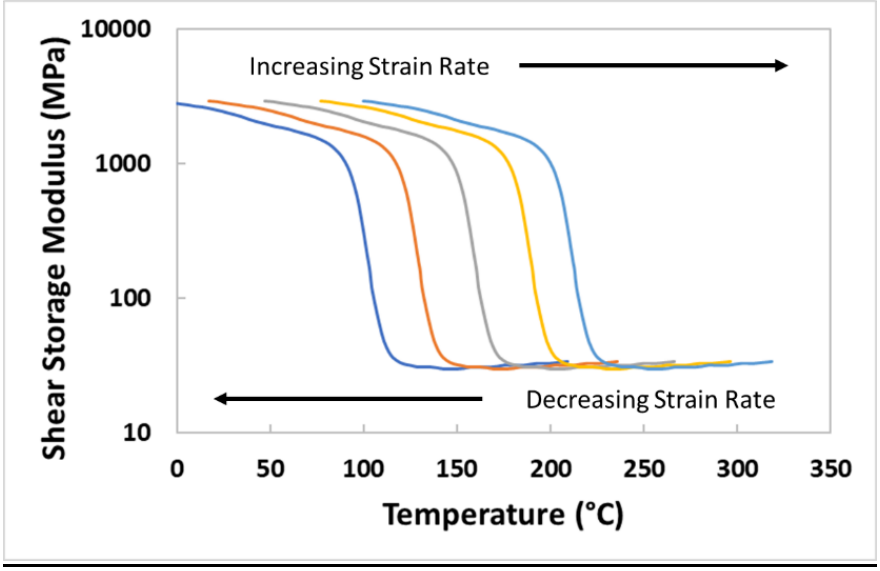

Figure 2.5-1: Illustration of Shifting of Epon 862 Epoxy DMA Data (Gilat et al., 2007) with Strain Rate

It is interesting to note that the glass transition temperature is indeed rate dependent, increasing with increasing strain rate (Mulliken and Boyce, 2006). In this research, it is assumed that the shear modulus is equal to the shear storage modulus. While the shear modulus is technically defined as the square root of the sum of the squares of the shear storage modulus, G', and shear loss modulus, G'' (Menard and Menard, 2008), i.e., $G = \sqrt{(\mathrm{G}')^2 + (G'')^2}$, the justification of the aforementioned assumption, $G = G'$, is supported by the fact that the shear loss modulus, at least for the E862 epoxy considered herein, has a relatively low value in comparison with the shear storage modulus over a wide range of temperatures. Figure 2.5-2 shows the shear storage modulus, the shear loss modulus, the corresponding loss tangent (i.e., the ratio of the shear loss modulus and shear storage modulus) for E862 DMA data presented in Gilat et al. (2007). Also shown in Figure 2.5-2 is the total shear modulus and the ratio of the total shear modulus to the loss tangent. The total shear modulus was computed using the data presented in Gilat et al. (2007) using the

aforementioned relation: $G = \sqrt{(\mathrm{G'})^2 + (G'')^2}$. The plot in Figure 2.5-2 has two y-axes; the moduli are referred to the left y-axis whereas the loss tangent and the ratio of the total shear modulus to the shear storage modulus are referred to the right y-axis.

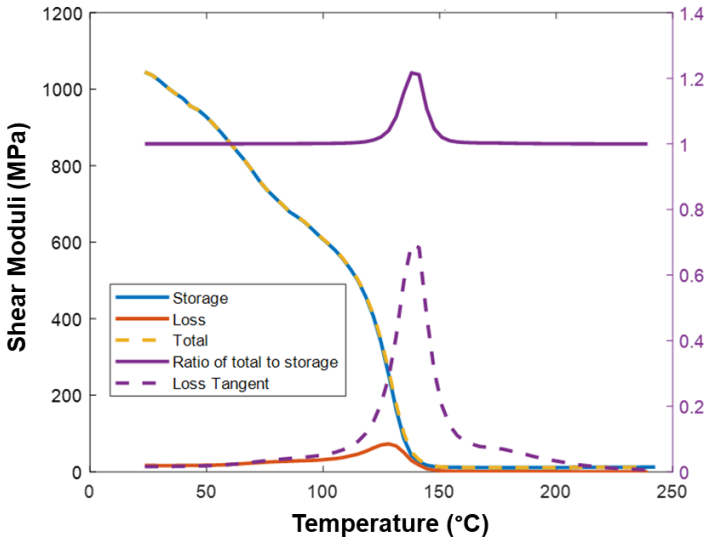

Figure 2.5-2: Comparison between shear modulus (denoted "total"), shear storage, shear loss moduli, and the loss tangent

It is evident from Figure 2.5-2 that, except for a range of temperatures corresponding to the glass transition, the shear loss modulus is nominal compared to the shear storage modulus. The maximum value of the ratio of the total shear modulus to the storage modulus is approximately 1.2 and occurs at a temperature of approximately 138 °C. This implies the assumption of $G = G'$ would be a maximum of 20% underpredicted near the glass transition. Since the goal of this chapter is to extend the Goldberg model (Goldberg et al., 2005) to enable thermodynamically consistent adiabatic temperature rise predictions and the resulting thermal softening, and not to develop a polymer constitutive model describing the glass transition process, this was deemed acceptable.

Assuming the elastic Poisson's ratio is independent of temperature and strain rate (Mulliken and Boyce, 2006; Jordan et al., 2008; Varghese and Batra, 2009), the shifting of the DMA data allows the elastic properties to be determined at various strain rates (can also be extrapolated to higher/lower strain rate values than those at which the DMA tests were conducted) and temperatures. To perform the horizontal (temperature direction) shifting of the shear storage modulus versus temperature curve with strain rate, it is necessary to determine a reference strain rate, $\dot{\varepsilon}_{ref}$, with respect to which the shifting occurs. Since the DMA shear storage modulus versus temperature curve for E862 presented in Gilat et al. (2007) corresponds to a strain rate of 0.02 s^{-1}, this value has been taken as the reference strain rate. To perform the shifting numerically, the logarithm (base ten) of the ratio of the actual strain rate to the reference strain rate, the "log strain rate ratio", must be computed and multiplied by what is referred to herein as the "DMA shift factor". The log strain rate ratio quantifies the number of decades the actual strain rate is above or below the reference strain rate. For example, an actual strain rate of 0.2 s^{-1} and reference strain rate of 0.02 s^{-1} would result in a log strain rate ratio of one (since the actual strain rate in this case would be ten times greater than the reference strain rate and the logarithm of ten is one).

The DMA shift factor quantifies how much the shear storage modulus versus temperature shifts horizontally per decade change in strain rate with respect to the reference strain rate. Since a tabular approach has been taken, the value of the DMA shift factor must be determined via trial and error during the calibration procedure. In this work, a DMA shift factor of 5 Kelvin per decade strain rate was found to provide a reasonably accurate description of the rate and temperature dependence of E862 elastic properties. If DMA data

is unavailable, it is recommended to at least approximate the rate and temperature dependence of the elastic modulus of the material of interest. This can be done by measuring the elastic properties over a range of temperatures and strain rates and determining an approximate functional dependence of the moduli on rate and temperature. The reader is referred to Richeton et al. (2007) for an example of an analytical description of the rate and temperature and dependence of the elastic moduli. Note that if the temperature dependence of the elastic moduli is not accounted for, adiabatic temperature rises predicted using the viscoplasticity model will not be able to predict thermal softening of the elastic properties, which is caused because the elastic moduli decrease with increasing temperature. It should also be noted that, if the unified viscoplasticity formulation is implemented into a FE code as a UMAT subroutine, a strain rate below which no shifting of the shear storage modulus versus temperature curve occurs should be defined. This is because, at least in explicit FE simulations, integration point effective strain rates will be zero until deformation occurs. Since the limit of the logarithm function as its argument approaches zero is negative infinity, a strain rate of zero would result in a shift factor of negative infinity, which would cause numerical problems.

2.6 Model Calibration – Determination of Nonisothermal Viscoplastic Model Parameters

The nonisothermal polymer viscoplastic constitutive model requires determining five constants (D_0, n, q, γ, *and* ξ) and two functions of temperature, $\bar{Z}_0(T)$ and $\bar{Z}_1(T)$. The characterization procedure is based on neat resin isothermal test data at different temperatures. Once the temperature-dependent state variables, $\bar{Z}_0$ and $\bar{Z}_1$, are known at multiple temperatures, they can be expressed as functions of temperature using regression

techniques. The value of D_0 is currently assumed to be equal to 10^6 s^{-1} (Goldberg et al., 2005). The procedure for the determination of the remaining model parameters is described below.

Since the hydrostatic stress is zero a pure shear stress state, the initial calibration is based on pure shear stress-strain data. The values of *n* and $\bar{Z}_1$ at a given temperature are determined as follows using Equation 2.3-13, simplified for the case of pure shear loading ($J_2 = \tau^2$; $\sigma_e = \sqrt{3}|\tau|$):

$$\dot{\varepsilon}^I = \frac{\dot{\gamma}^I}{2} = D_0 \, exp\left(-\frac{1}{2}\left(\frac{\bar{Z}(T)}{\sqrt{3}|\tau|T}\right)^{2n}\right)\left(\frac{\tau}{|\tau|}\right). \tag{2.6-1}$$

where $\dot{\gamma}^I$ is the inelastic engineering shear strain rate. Equation 2.6-1 is then manipulated to yield:

$$ln\left(-2ln\left(\frac{\dot{\gamma}^I}{2D_0}\right)\right) = 2n * ln\left(\bar{Z}(T)\right) - 2n * ln\left(\sqrt{3}|\tau|T\right). \tag{2.6-2}$$

To obtain the value of the constant n and $\bar{Z}_1$ at a particular temperature, constant strain rate pure shear tests at various strain rates (ideally at least three) at the temperature of interest are used. The value of the saturation shear stress, τ_s, (the stress level where the stress-strain curve flattens out and the inelastic strain rate becomes equal to the total strain rate) is then substituted in for τ in Equation 2.6-2. Since at saturation, the inelastic strain rate is equal to the total strain rate, the value of the inelastic engineering shear strain rate, $\dot{\gamma}^I$, is set equal to the total applied engineering strain rate, $\dot{\gamma}_0$. For each available shear stress-strain curve, data pairs of the total applied engineering shear strain rate and the corresponding saturation shear stress (one pair for each curve) are used. The values of the absolute test temperature and the constant D_o are also substituted into Equation 2.6-2. Least squares regression is

then performed on the data pairs of shear strain rates and corresponding saturation shear stresses for each test. The value of $\bar{Z}$ is taken to be the value at saturation, $\bar{Z}_1$. As evident from Equation 2.6-2, the slope of the line of best fit is equal to -2n and the intercept is equal to $2n * ln(\bar{Z}_1(T))$. The values $\bar{Z}_1$ for a given temperature and n are now known. This procedure is repeated for pure shear tests at various rates at other temperatures to determine the temperature-dependence of $\bar{Z}_1$. In this research, n is assumed to be constant, however a possible inverse relationship between n and temperature (i.e., higher rate sensitivity for higher temperatures) has been suggested (Bodner, 2001).

To obtain the value of $\bar{Z}_0$ at a particular temperature, Equation 2.6-1 is rearranged as follows:

$$\bar{Z}(T) = \left[-2ln\left(\frac{\dot{\gamma}^I}{2D_0}\right)\right]^{\frac{1}{2n}} \sqrt{3}|\tau|T. \tag{2.6-3}$$

The values of shear stress and corresponding inelastic engineering shear strain rate where the shear stress-strain curves deviate appreciably from linearity are used in Equation 2.6-3 for the values of τ and $\dot{\gamma}^I$, respectively. One hundredth of the constant strain rate used in the test has been found by trial and error to be a good approximation the value of $\dot{\gamma}^I$ (Goldberg et al., 2005). Equation 2.6-3 is then evaluated for $\bar{Z}$, which is set equal to $\bar{Z}_0$. This procedure is repeated for multiple temperatures to determine the temperature-dependence of $\bar{Z}_0$.

To determine the value of q for Equations 2.3-14a and 2.3-14b, Equation 2.3-14a is integrated for the case of pure shear loading, resulting in

$$\bar{Z}(T) = \bar{Z}_1(T) - \left(\bar{Z}_1(T) - \bar{Z}_0(T)\right)exp\left[\frac{-q}{\sqrt{3}}\gamma^I\right] \tag{2.6-4}$$

where γ^I is the engineering shear strain. At saturation, $\bar{Z}(T)$ approaches $\bar{Z}_1(T)$ and the exponential term approaches zero. It is assumed saturation occurs when the following condition is satisfied (Goldberg et al., 2005)

$$exp\left[\frac{-q}{\sqrt{3}}\gamma_s^I\right] = 0.01 \tag{2.6-5}$$

where γ_s^I is the inelastic shear strain at saturation. Equation 2.6-5 is then solved for the hardening rate, q.

To determine the values of the hydrostatic constants, γ & ξ, uniaxial tensile and uniaxial compressive test data are used. Ideally, one would measure the tensile and compressive plastic Poisson's ratios in the uniaxial tests using digital image correlation (DIC) and use Equations 2.3-21 and 2.3-22 to determine the values of A_{UT} and A_{UC}. The values of A_{UC} and A_{UT} would then be used in Equations 2.3-19b and 2.3-20b to determine the values of the hydrostatic constants:

$$\begin{bmatrix}-1 & 1\\ 1 & 1\end{bmatrix}\begin{bmatrix}\sqrt{\gamma}\\ \xi\end{bmatrix} = \begin{bmatrix}A_{UC}\\ A_{UT}\end{bmatrix} \rightarrow \begin{bmatrix}\sqrt{\gamma}\\ \xi\end{bmatrix} = \frac{1}{2}\begin{bmatrix}-1 & 1\\ 1 & 1\end{bmatrix}\begin{bmatrix}A_{UC}\\ A_{UT}\end{bmatrix} \tag{2.6-6}$$

However, it is well known that, after the peak load, plastic instabilities (necking in tension and barreling in compression) cause nonuniform stress and strain states in the gage section (Poulain et al., 2013; Poulain et al., 2014) and, thus, the plastic Poisson's ratios are likely not material constants (Kolling et al., 2005). The plastic Poisson's ratios may change with temperature, strain rate, and the level of deformation. However, to keep the constitutive model tractable, the tensile and compressive plastic Poisson's ratios are assumed to be constant. If it is found that the characterization is precluded by the assumption of constant plastic Poisson's ratios, evolution equations for the hydrostatic parameters, similar to those in Goldberg et al. (2005) (Equation 2.2-5), could be used, though care should be taken to

ensure the constraints summarized in Section 2.3.6 (Table 2.3.1) are satisfied. If information regarding the permanent volume change in uniaxial tensile and compressive tests is available, this information can be used to facilitate the determination of the hydrostatic constants as well. For example, if there is no permanent volume change in a uniaxial compression test, it suggests a compressive plastic Poisson's ratio of 0.5 (plastically incompressible in compression). If values of the tensile and compressive plastic Poisson's ratios are unavailable, it can be assumed that the effective stresses (Equation 2.3-5) at saturation in pure shear, uniaxial tension, and uniaxial compression are equal for a given strain rate and temperature (i.e., the shear, tension, and compression tests should be conducted at approximately the same temperature and strain rate). This results in the following two equations

$$\sqrt{3}\tau_s = \sigma_{st}\left(1 + \sqrt{3\gamma} + \sqrt{3}\xi\right) \tag{2.6-7}$$

$$\sqrt{3}\tau_s = \sigma_{sc}\left(1 + \sqrt{3\gamma} - \sqrt{3}\xi\right) \tag{2.6-8}$$

where τ_s, σ_{st}, and σ_{sc} are the shear, tensile, and compressive stresses at saturation, respectively. It is evident that, for a pressure independent material ($\gamma = \xi = 0$), the well-known relation between the shear, tensile, and compressive stresses at saturation is obtained: $\sqrt{3}\tau_s = \sigma_{st} = \sigma_{sc}$. By inserting the saturation values of the experimental shear, tensile, and compressive stresses, Equations 2.6-7 and 2.6-8 can be solved for the two unknown hydrostatic constants, γ and ξ. The values of these constants are assumed to be independent of rate and temperature, so the results from tests at one strain rate and temperature are sufficient to find the necessary values. Note that in this model, for a given strain rate and temperature, the larger the tensile and/or compressive plastic Poisson's ratio,

the larger the tensile and/or compressive saturation stresses. Thus, the maximum tensile and compressive saturation stresses for a given strain rate and temperature are therefore obtained for plastic Poisson's ratios of 0.5.

2.7 Results and Discussion

2.7.1 Monolithic Polymer Response

To demonstrate the capability of the modified constitutive model, it is calibrated for E862 epoxy using available data (Gilat et al., 2007; Littell, 2008; Littell et al., 2008) from uniaxial tension, uniaxial compression and pure shear tests conducted over a range of strain rates and temperatures. In this section, the 620 s^{-1} tensile curves are from Gilat et al. (2007) whereas the rest of the data is from Littell (2008) and Littell et al. (2008). Note that all tests used for characterization were conducted below the E862 glass transition temperature reported by Gilat et al. (2007), 133°C, which was determined from a DMA test conducted in oscillatory shear at 10 rad/s, which corresponds to a shear strain rate of 0.02 s^{-1} (Gilat et al., 2007). The experimental E862 stress-strain data presented in Littell (2008) and Littell et al. (2008) is in terms of engineering stress and a local strain determined by averaging digital image correlation (DIC) measurements at several points in the middle of the specimen gage sections (Littell, 2008; Poulain et al., 2013). The DIC strains presented in Littell (2008) and Littell et al. (2008) are therefore assumed to be the true strains whereas the true stresses were computed using the following equation (Poulain et al., 2013):

$$\sigma^{true} = \frac{\sigma^{eng}}{exp(2\varepsilon_T^{true})} \tag{2.7-1}$$

where ε_T^{true} is the transverse true strain measured by the DIC in the uniaxial tension and uniaxial compression tests. Since the relationship between longitudinal and transverse true

strain for uniaxial loading is $\varepsilon_T^{true} = -v\varepsilon_L^{true}$ and the relation between engineering normal strain and true normal strain is $\varepsilon^{true} = \ln(\varepsilon^{eng} + 1)$, the relationship between the longitudinal and transverse engineering strain for uniaxial loading is $\left(1 + \varepsilon_T^{eng}\right) = \left(1 + \varepsilon_L^{eng}\right)^{-v}$ (Arnold et al., 2019). It is therefore evident that, for a Poisson's ratio of 0.5, Equation 2.7-1 reduces to the well-known conversion between true stress and engineering stress, $\sigma^{true} = \sigma^{eng}\left(1 + \varepsilon_L^{eng}\right) = \sigma^{eng}\exp(\varepsilon_L^{true})$, which assumes incompressibility. The shear test data presented in Littell (2008) and Littell et al. (2008) was unmodified.

The E862 resin material properties and model parameters obtained from the calibration and used in the simulation results presented in this section are shown in Table 2.7.1. To illustrate how the values of the hydrostatic constants were obtained, consider the room temperature shear, tension, and compression data presented in Figures 2.7-1a, 2.7-2a, and 2.7-3a. The saturation stresses for the shear, tension, and compression tests conducted at strain rates of $1.6\text{x}10^{-1}$ s^{-1}, $1\text{x}10^{-1}$ s^{-1}, and $1\text{x}10^{-1}$ s^{-1} are 64.99 MPa, 103.83 MPa, and 112.23 MPa, respectively. Using these values in Equations 2.6-7 and 2.6-8 yields tensile and compressive plastic Poisson's ratios of 0.3836 and 0.4955. These values were slightly adjusted manually to obtain an optimal fit with the pure shear, uniaxial tension, and uniaxial compression test data at the various other test temperatures and strain rates; the values of γ and ξ in Table 2.7.1 correspond to tensile and compressive plastic Poisson's ratios of 0.3827 and 0.5, respectively.

In the simulation results presented in this section, the inelastic heat fraction has been set to zero (isothermal conditions; no adiabatic heating) since i) many of the experiments were conducted at low strain rates, where adiabatic heating due to the conversion of plastic work to heat can be assumed to be negligible and ii) the available high strain rate test data

exhibited fairly low failure strains, where the material response displayed minimal nonlinearity, and thus likely limited adiabatic heating due to viscoplastic deformation. Using Equation 2.4-3, E862 material properties ($\rho = 1{,}200\ \frac{kg}{m^3}$ (Littell, 2008), $k = 0.18\ \frac{W}{m-K}$ (Spurgeon, 2018), $C = 1{,}260\ \frac{J}{kg-K}$ (Rowghanian and Hoa, 2011), and assuming the characteristic length in Equation 2.4-3, Δx, is equal to half of the initial test coupon gage diameter used in the E862 neat resin tension and compression tests presented in Littell (2008) and Littell et al. (2008) ($\Delta x = 1.5875\ mm$, which is equal to the test coupon initial gage radius), the characteristic thermal diffusion time is found to be 21.17 seconds. The corresponding approximate strain rate at which the system would be expected to behave adiabatically, Δt_d^{-1}, is 0.047 s^{-1}. Note that this approximation does not account for the potential temperature dependence of the thermal properties of the material or the fact that the characteristic length, Δx, changes throughout the test as the specimen deforms. Additionally, in reality, the transition from roughly isothermal to roughly adiabatic conditions spans a range of strain rates. Garg et al. (2008) conducted uniaxial compression tests on E862 and found experimentally that, for cubic specimens of 5 mm and 10 mm side lengths, a strain rate of 0.5 s^{-1} provided approximately adiabatic conditions. However, using the thermal properties mentioned above, Equation 2.4-3, and considering the characteristic length to be half the side length of the cubic specimens (Garg et al., 2008), the approximate transition strain rates for the 5 mm and 10 mm side length cubic specimens are 0.019 and 0.0048, respectively, which are roughly 26 and 104 times less than reported value of 0.5 s^{-1} (Garg et al., 2007). This implies that the strain rate at which the E862 tests presented in Littell (2008) and Littell et al. (2008) exhibit approximately adiabatic conditions could potentially be between 1.2 s^{-1} and 4.9 s^{-1} (26 and 104 times greater than

the value computed using Equation 2.4-3). It is therefore reasonable to assume isothermal conditions for the simulations in this section. The fact that Garg et al. (2007) observed approximately adiabatic conditions at a strain rate of 0.5 s^{-1} helps to further justify the adiabatic assumption for dynamic loading, such as impact events, where much larger strain rates are expected. Also note that Poulain (2010) has suggested that the post-peak softening observed in the E862 compression response (Littell, 2008; Littell et al., 2008) is intrinsic material behavior, not thermal softening.

Figures 2.7-1, 2.7-2, and 2.7-3 show the simulated and experimental pure shear, uniaxial tensile, and uniaxial compressive stress-strain response of E862 epoxy resin at room temperature (25°C), 50°C, and 80°C for various strain rates. Reasonably good correlations with experimental data are obtained for all the strain rates and temperatures for shear, tensile and compressive loading. Based on the characterization, it was found that $\bar{Z}_0$ and $\bar{Z}_1$ decrease approximately linearly with temperature, as shown in Table 2.7.1, which is why the model slightly underestimates the shear saturation stresses at 50°C (Figure 2.7-1b). Due to the significant change in elastic properties above the glass transition temperature, it is likely that $\bar{Z}_0$ and $\bar{Z}_1$ would exhibit a different (nonlinear) functional dependence than shown in Table 2.7.1 near and above the glass transition. Therefore, modeling $\bar{Z}_0$ and $\bar{Z}_1$ as piecewise functions of temperature or using a tabular approach may be more appropriate. Regardless of the method used to model the temperature dependence of $\bar{Z}_0$ and $\bar{Z}_1$, these functions must decrease with increasing temperature (resistance to internal stress decreases as temperature increases). Care should also be taken to ensure $\bar{Z}_0$ and $\bar{Z}_1$ are always positive and that $\bar{Z}_1$ is always greater than $\bar{Z}_0$ for temperature ranges of interest; this may require setting these parameters to be constant for very high temperatures.

It is evident that in Figure 2.7-3a that the room temperature saturation stresses in the 10^{-3} s^{-1} and 10^{-5} s^{-1} strain rate uniaxial compression simulations are slightly lower than the experimental values. This is interesting because the compressive plastic Poisson's ratio in the model is 0.5 and therefore the compressive saturation stresses are the highest they can possibly be (since the saturation stress increases with plastic Poisson's ratio and 0.5 is the upper bound). Figure 2.7-3c shows that the 80°C saturation stress in the 10^{-3} s^{-1} strain rate compression simulation is slightly higher than the experimental value. This could suggest a nonconstant compressive plastic Poisson's ratio. As evident in Figures 2.7-1, 2.7-2, and 2.7-3, the model does not simulate the intrinsic strain softening observed in the compressive material response or the second hardening observed in the tensile and compressive response at large strains. This is assumed to be acceptable since the matrix in PMCs will likely fail at small strains before these effects become significant.

Table 2.7.1: Epon 862 Material Properties and Model Parameters

<table>
<tr><td>Young’s Modulus (GPa)</td><td colspan="5">*Taken from DMA curve (Figure 2.5-1)*
<table>
<tr><td colspan="2" rowspan="2"></td><td colspan="3">Temperature (°C)</td></tr>
<tr><td>30</td><td>50</td><td>80</td></tr>
<tr><td rowspan="3">Strain Rate (s^{-1})</td><td>10^{-3}</td><td>2.90</td><td>2.58</td><td>2.00</td></tr>
<tr><td>1</td><td>3.27</td><td>2.81</td><td>2.29</td></tr>
<tr><td>1,000</td><td>3.65</td><td>3.14</td><td>2.58</td></tr>
</table></td></tr>
<tr><td>Poisson’s Ratio</td><td colspan="5">0.4</td></tr>
<tr><td>Density (kg/m^3)</td><td colspan="5">1,200</td></tr>
<tr><td>Specific Heat (J/kg-K)</td><td colspan="5">1,260</td></tr>
<tr><td>CTE (1/K)</td><td colspan="5">5.4e-5</td></tr>
<tr><td>D_0 (s^{-1})</td><td colspan="5">10^6</td></tr>
<tr><td>n</td><td colspan="5">0.6351</td></tr>
<tr><td>q</td><td colspan="5">74.4073</td></tr>
<tr><td>γ</td><td colspan="5">0.0006</td></tr>
<tr><td>ξ</td><td colspan="5">0.02449</td></tr>
<tr><td>$\bar{Z}_0(T)$ (Pa-K)</td><td colspan="5">$-(1.462e9)T + 7.421e11$</td></tr>
<tr><td>$\bar{Z}_1(T)$ (Pa-K)</td><td colspan="5">$-(2.365e9)T + 1.232e12$</td></tr>
</table>

a)

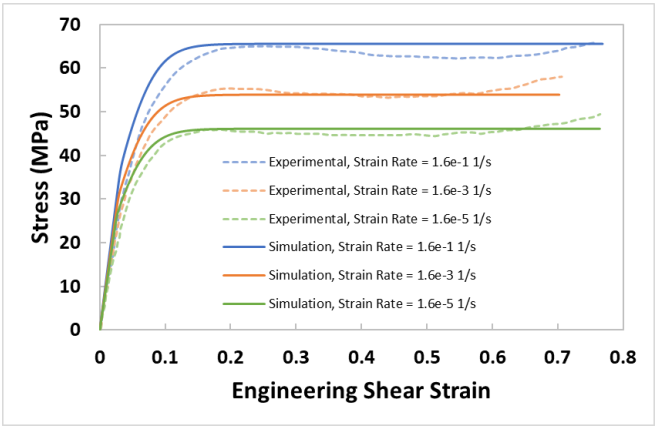

b)

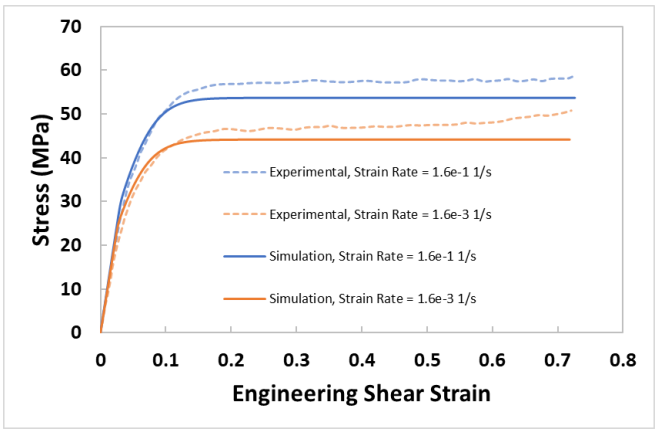

c)

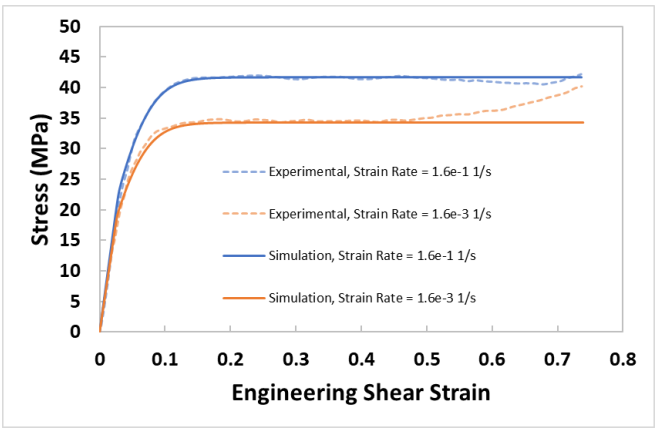

Figure 2.7-1: Simulated and Experimental Shear Stress-Strain Response of Epon 862 Epoxy at a) Room Temperature (25°C); b) 50°C; c) 80°C

a)

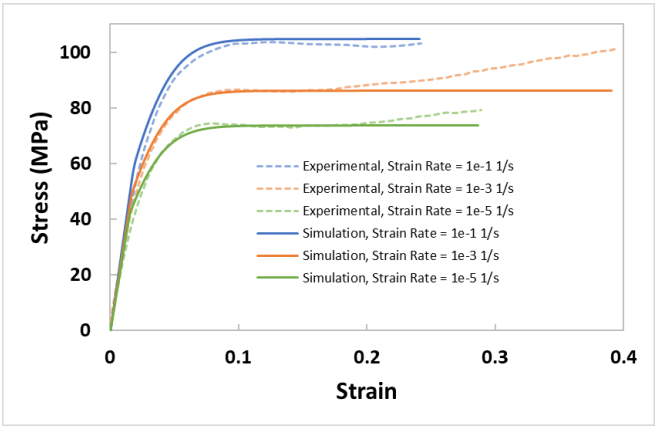

b)

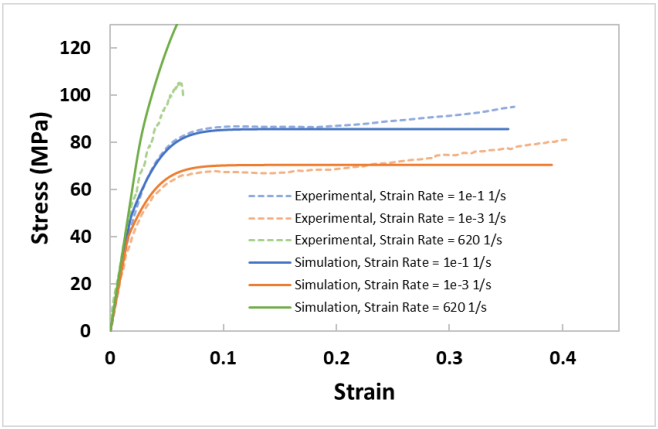

c)

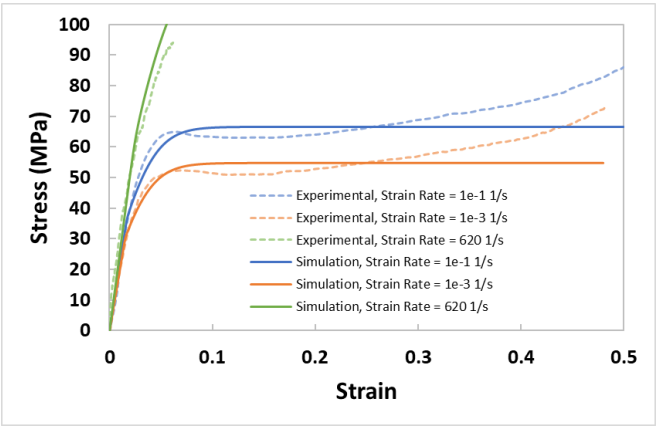

Figure 2.7-2: Simulated and Experimental Tensile Stress-Strain Response of Epon 862 Epoxy at a) Room Temperature (25°C); b) 50°C; c) 80°C

a)

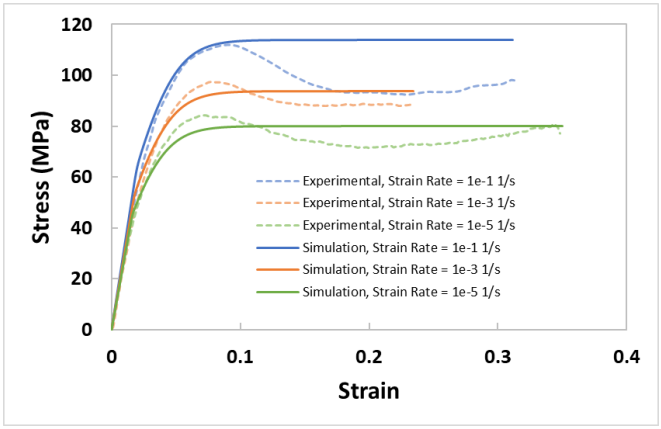

b)

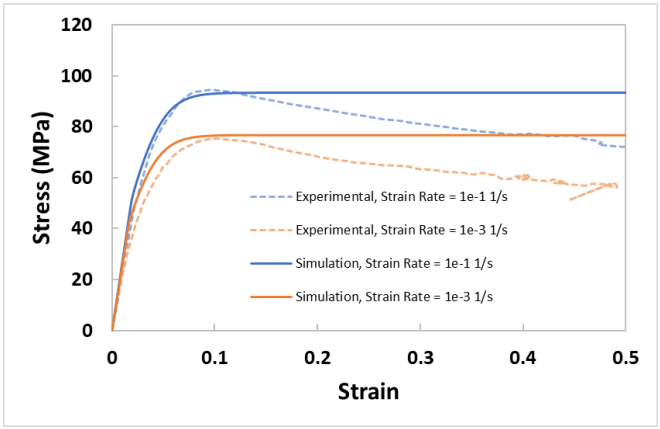

c)

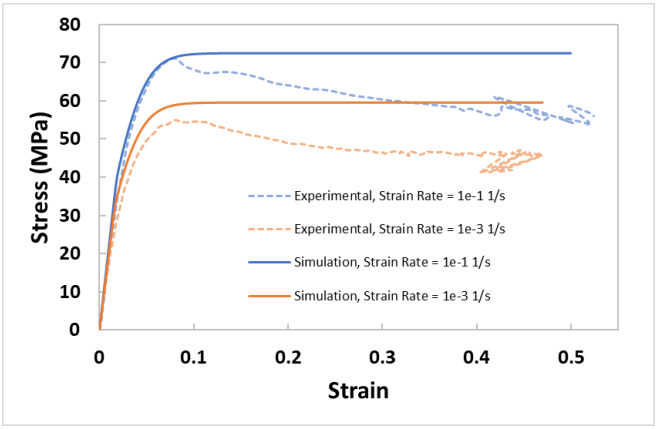

Figure 2.7-3: Simulated and Experimental Compressive Stress-Strain Response of Epon 862 Epoxy at a) Room Temperature (25°C); b) 50°C; c) 80°C

2.7.2 Effect of Inelastic Heat Fraction

Figures 2.7-4a) through 2.7-4c) show the effect of varying the inelastic heat fraction between zero and unity for pure shear, uniaxial tensile, and uniaxial compressive loading for an applied total strain rate of 1000 s^{-1} and an initial temperature of 25°. Higher temperature rises, resulting in more thermal softening, are observed for higher inelastic heat fractions for all loading cases, as expected.

a)

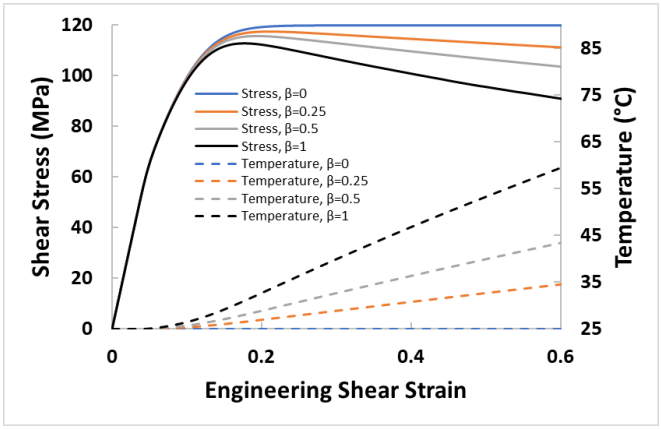

b)

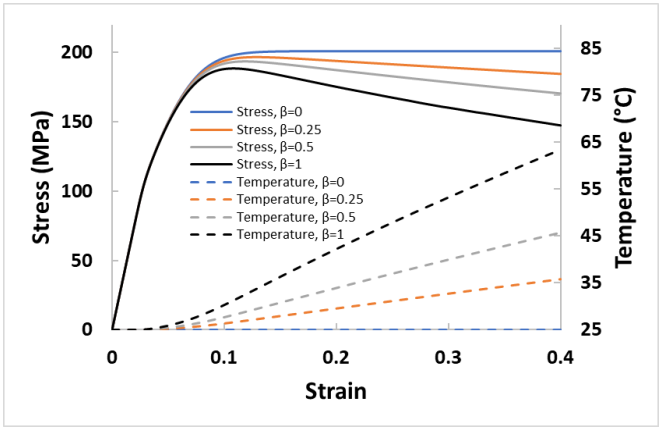

c)

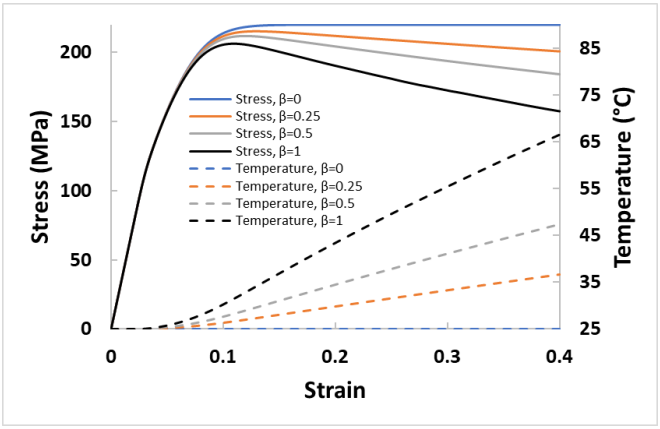

Figure 2.7-4: Effect of Varying Inelastic Heat Fraction on a) Pure Shear; b) Uniaxial Tensile; c) Uniaxial Compressive Stress-Strain and Temperature-Strain Response

2.7.3 Comparison Between Goldberg Model and Improved Model

To demonstrate the improvements made to the Goldberg (Goldberg et al., 2005) model, the response of the improved model is compared to the Goldberg model at 25°C. All the Goldberg model parameters are identical to those in the improved model, except Z_0, Z_1, and the hydrostatic constants. In the Goldberg model, the components of the inelastic strain rate tensor components are not temperature dependent. Therefore, the values of $Z_0(T)$ and $Z_1(T)$ in the Goldberg model are equal to those in the improved model divided by the absolute temperature to facilitate the comparison. Additionally, since the Goldberg model employs a single hydrostatic state variable, α, its initial and final values (α_0 and a_1) have been set equal to the value of A_{UT} (0.049), which results in constant plastic Poisson's ratios.

Figure 2.7-5 shows the stress and total Poisson's ratio predicted by the improved model and the Goldberg model as a function of strain in the load direction for simulated uniaxial tensile and uniaxial compressive loading under an applied total strain rate of 1000 s^{-1}. In Figure 2.7-5a, the tensile saturation stresses are the same, but the compressive saturation stresses are different. This implies that the Goldberg model is capable of simulating the same response as the improved model in tension and shear, but not in compression. Figure 2.7-5b shows the *total* Poisson's ratios in tension and compression for both models, where the total Poisson's ratios were computed as the negative ratio of the transverse total strain rate to the longitudinal total strain rate. The total Poisson's ratios start at their elastic values of 0.4 (Table 2.7.1) and, in the case of the improved model, approach their plastic values as the deformation progresses. However, in the Goldberg

model predictions the compressive Poisson's ratios exceed the upper bound of 0.5 derived in Section 2.3.4.

a)

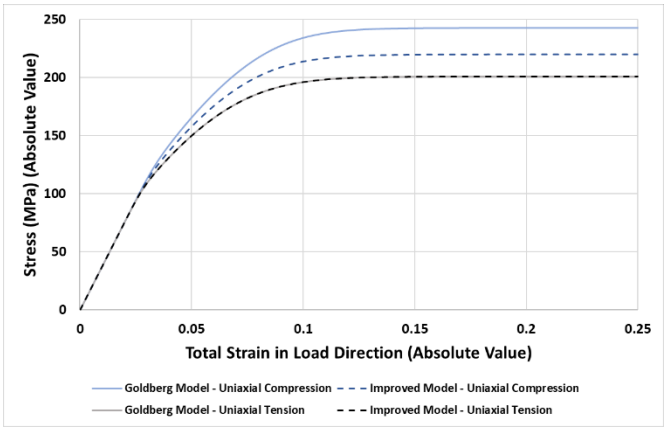

b)

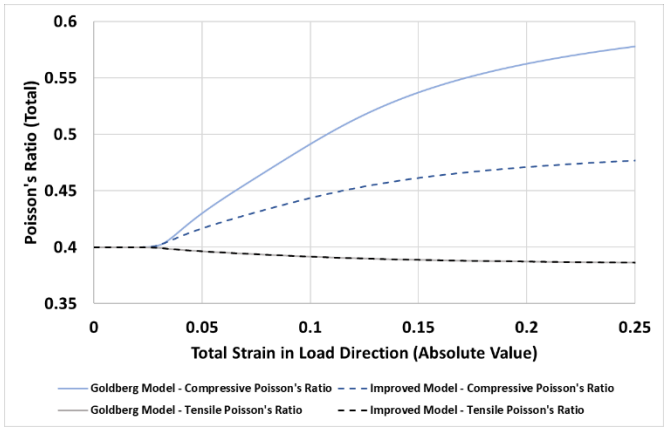

Figure 2.7-5: a) Stress and b) Poisson's Ratio as a Function of Strain in the Load Direction for Simulated Uniaxial Tensile and Uniaxial Compressive Loading

The following illustrates the importance of the fact that the expression for the parameter, A, given by Equation 2.3-1b, ($A = \sqrt{\gamma} sign(\sigma_{kk}) + \xi$), changes with the sign of the hydrostatic stress, σ_{kk}. Figure 2.7-6 shows the response of the improved model and the Goldberg model to a hydrostatic stress state, which was achieved by applying uniform strain-controlled compression at a strain rate of 1000 s^{-1} in each of the three normal directions simultaneously at 25°C. Recall that the compressive plastic Poisson's ratio for E862, determined via calibration against experimental data (Littell, 2008; Littell et al., 2008), is 0.5, which implies the material is plastically incompressible in compression. For

solely the simulation results presented in Figure 2.7-6, the tensile and compressive plastic Poisson's ratios have been set to 0.3 and 0.4, respectively ($\gamma = 0.00423$; $\xi = 0.0238$) so that the model can simulate nonisochoric plastic deformation under hydrostatic compression. Additionally, since the inelastic strain rate in the Goldberg model (Equation 2.2-1) is technically not defined for hydrostatic loading (due to division by $J_2 = 0$), the third line of Equation 2.3-9 was used to compute the inelastic strain rate tensor components, where A is set equal to A_{UT}, which in this case is 0.089. All other model parameters in the Goldberg model (Goldberg et al., 2005) and the improved model are unchanged. In Figure 2.7-6a, the Goldberg model (Goldberg et al., 2005) pressure versus volumetric strain curve becomes nearly vertical at a volumetric strain of approximately -0.1. In Figure 2.7-6b, the plastic volumetric strain has the wrong sign because the deviatoric stresses are zero and the hydrostatic state variable in the Goldberg model does not change signs with hydrostatic stress. In the improved model, the elastic and plastic volumetric strains are both negative, as they should be under hydrostatic compression. Figure 2.7-6c shows the effective stress and the accumulated plastic work density as a function of the accumulated effective inelastic strain. The Goldberg model results in a negative effective stress because the hydrostatic state variable does not change signs with pressure. Since the effective inelastic strain in the Goldberg model is always nonnegative due to the nonnegativity of the effective inelastic strain rate (Equation 2.2-6), the plastic work density is negative, which is thermodynamically incorrect. The improved model predicts positive plastic work density because the effective stress is guaranteed to be nonnegative as long as the constraints derived in Section 2.3.6 and shown in Table 2.3.1 are satisfied.

a)

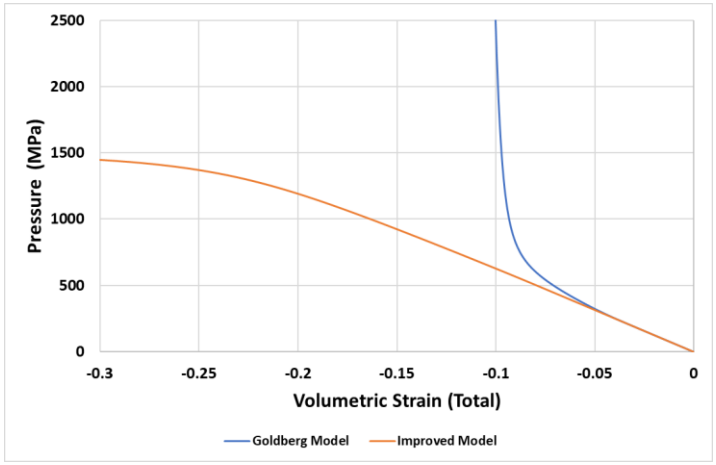

b)

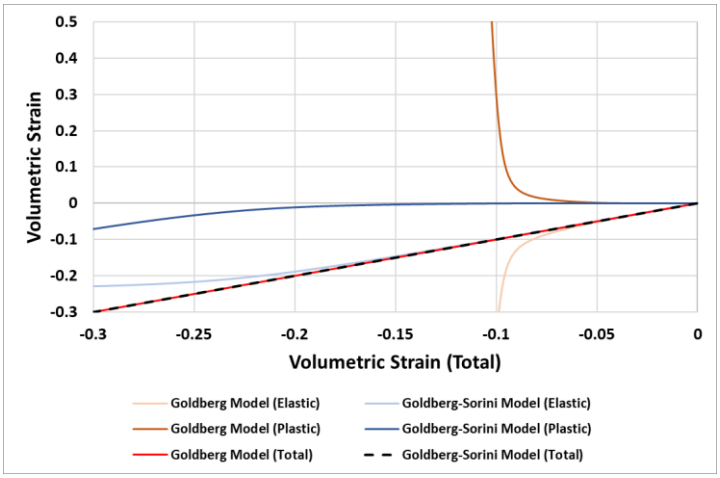

c)

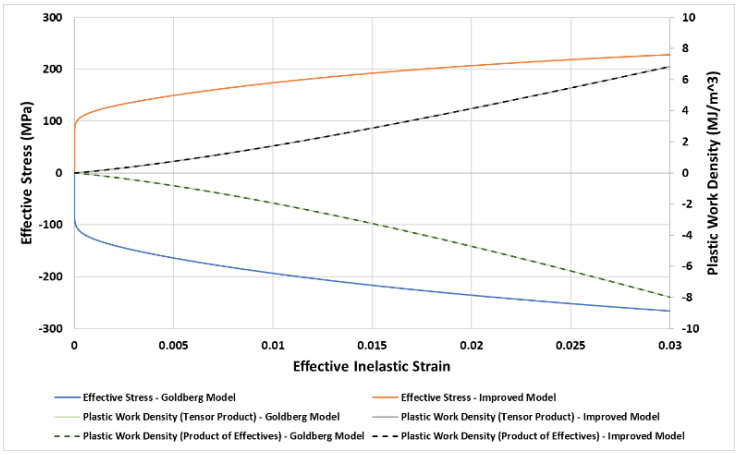

Figure 2.7-6: Response of Goldberg et al. (2005) Model and Improved Model to Hydrostatic Stress State: a) Pressure vs. Volumetric Strain; b) Elastic, Plastic and Total Volumetric Strain Components vs. Total Volumetric Strain

2.8 Conclusions

A nonisothermal and thermodynamically consistent extension of the rate- and pressure-dependent Goldberg (Goldberg et al., 2005) unified viscoplastic constitutive formulation, resulting in a rate-, temperature-, and pressure-dependent viscoplasticity formulation suitable for use in multiscale PMC impact problems has been presented. A new plastic potential function was proposed, where two hydrostatic constants control the level of influence of hydrostatic stress on plastic deformation. Elementary loading conditions were used to derive relations between model constants to ensure physically realistic plastic flow (i.e., tensile and compressive plastic Poisson's ratios between -1 and 0.5) and a nonnegative effective stress, which subsequently guarantees nonnegative plastic dissipation, a necessary thermodynamic requirement. Relations between the tensile and compressive plastic Poisson's ratios and the two hydrostatic constants were derived and a procedure to determine their values, as well as the other model constants, was presented. The model is strain rate, temperature, and pressure dependent and was shown to be capable of representing test data of a representative epoxy over a range of strain rates, temperatures, and loading conditions (pure shear, uniaxial tension, and uniaxial compression). The two hydrostatic constants used in the model permit the user to independently vary the tensile and compressive yield stresses and plastic Poisson’s ratios, which would not be possible using a single hydrostatic constant. The intended application of the improved unified viscoplastic constitutive formulation is the multiscale analysis of PMCs subjected to impact loading, where it is suitable to predict the rate, temperature, and pressure dependent inelastic deformation, as well as adiabatic heating and subsequent thermal softening, of the polymer matrix. The next chapter discusses the implementation of the viscoplasticity

model developed in this chapter into a micromechanics-based multiscale framework as well as its use in a subcell-based approach to model the impact response of braided PMCs.

3 MULTISCALE MODELING OF TRIAXIALLY BRAIDED POLYMER MATRIX COMPOSITES UNDER IMPACT LOADING

3.1 Introduction

In the first part of this two-part chapter, the extended version of the Goldberg model (Goldberg et al., 2005) described in the previous chapter is implemented into the semi-analytical GMC (Aboudi et al., 2012) micromechanics framework to investigate the effects of adiabatic heating on the high strain rate deformation of a T700/E862 UD composite. A micromechanics-based multiscale approach is used to allow adiabatic heating to be modeled at the matrix constituent level, where it has been experimentally observed to be predominant in flat panel impact tests conducted on triaxially braided PMCs (Johnston et al., 2018). Results indicate significant thermal softening due to adiabatic heating for matrix dominated deformation modes (transverse tension, transverse compression, and in-plane shear).

In the second part of this chapter, a synergistic multiscale approach is taken to investigate the quasi-static and impact response of a T700/E862 [0°/60°/–60°] triaxially braided composite. The GMC micromechanics model described in the first part of this chapter, including the nonisothermal viscoplasticity formulation presented in the last chapter, is implemented into the commercial transient dynamic FE code LS-DYNA (Hallquist, 2006) as a UMAT. A previously developed subcell-based modeling approach (Littell, 2008; Blinzler, 2012; Cheng and Binienda, 2008; Li et al., 2009; Goldberg et al., 2012; Xiao et al., 2011; Cater et al., 2014; Cater et al., 2015) is extended and used to approximate the mesoscale composite braid architecture as an assemblage of laminated composite subcells to approximate the heterogeneity at the highest analysis length scale.

Fiber failure is incorporated into the analyses using both the maximum stress criterion and the Curtin (1991) progressive fiber damage model. A top-down approach is used to determine/calibrate the failure properties to correlate with straight-sided quasi-static coupon tests.

Impact simulation results indicate significant heat generation in an impact event due to adiabatic heating in the polymer matrix. The synergistic multiscale approach undertaken herein is beneficial in that it allows the rate- and temperature-dependent matrix constituent properties to be determined based on the effective strain rate experienced locally, which, due to the complexity of an impact event, cannot be determined a-priori and vary both spatially within a structure and temporally in an impact event. Simulation results are compared with test data provided by NASA Glenn Research Center and discrepancies between simulation and test results are discussed.

3.2 Micromechanical Modeling of the Effects of Adiabatic Heating on the High Strain Rate Deformation of Polymer Matrix Composites

3.2.1 Micromechanical Modeling Using the Generalized Method of Cells Micromechanics Theory

To investigate the effects of adiabatic heating on the effective constitutive behavior of a UD composite, the rate-, temperature-, and pressure-dependent viscoplasticity model developed in the previous chapter is implemented into the existing GMC micromechanics framework (Aboudi et al., 2012). In the micromechanics model used herein, a doubly periodic RUC consisting of one fiber subcell and three matrix subcells, shown in Figure 3.2-1, is employed for the micromechanical analyses. The subcells in Figure 3.2-1 are denoted with indices (β, γ). As indicated in the figure, the 1-direction corresponds to the

fiber direction and the RUC is doubly periodic in the 23-plane. Though the RUC is doubly periodic, the effective (global/average) and local (constituent/subcell) constitutive relations are indeed fully three-dimensional.

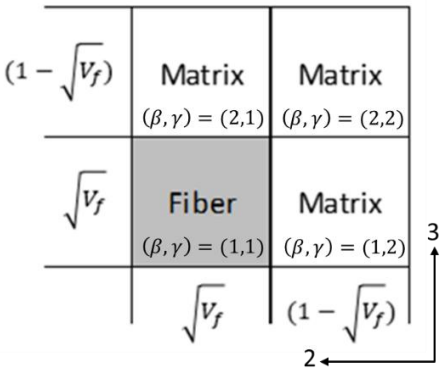

Figure 3.2-1: Schematic of Four-Subcell Microscale Repeating Unit Cell for GMC Micromechanics Analysis

The GMC (Aboudi et al., 2012) assumes a first order subcell displacement field and, via the enforcement of displacement and traction continuity conditions between adjacent subcells and adjacent RUCs in an average (integral) sense, elastic and inelastic strain concentration matrices, **A** and **D**, are determined. These concentration matrices relate local subcell strains, $\boldsymbol{\varepsilon_s}$, to the global (i.e., homogenized) strain tensor applied to the RUC, $\bar{\boldsymbol{\varepsilon}}$, and local inelastic and thermal strains, $\boldsymbol{\varepsilon_S^I}$ and $\boldsymbol{\varepsilon_S^{th}}$, according to

$$\boldsymbol{\varepsilon_s} = \boldsymbol{A}\bar{\boldsymbol{\varepsilon}} + \boldsymbol{D}(\boldsymbol{\varepsilon_S^I} + \boldsymbol{\varepsilon_S^{th}}) \tag{3.2-1}$$

where $\boldsymbol{\varepsilon_s}$, $\boldsymbol{\varepsilon_S^I}$, and $\boldsymbol{\varepsilon_S^{th}}$ are vectors that contain the respective total, inelastic, and thermal strain components of all subcells in the RUC. The global strains applied to the RUC, $\bar{\boldsymbol{\varepsilon}}$, are considered known quantities. The strain tensor for a particular subcell (β,γ) is expressed in terms of the average total strain applied to the RVE, $\bar{\boldsymbol{\varepsilon}}$, and the concentration submatrices corresponding to the subcell (β,γ), $\boldsymbol{A}^{(\beta,\gamma)}$ and $\boldsymbol{D}^{(\beta,\gamma)}$, as follows:

$$\boldsymbol{\varepsilon}^{(\beta,\gamma)} = \boldsymbol{A}^{(\beta,\gamma)}\bar{\boldsymbol{\varepsilon}} + \boldsymbol{D}^{(\beta,\gamma)}(\boldsymbol{\varepsilon}_{\boldsymbol{S}}^{\boldsymbol{I}} + \boldsymbol{\varepsilon}_{\boldsymbol{S}}^{\boldsymbol{th}}) \tag{3.2-2}$$

The local Cauchy stress tensor in each subcell (β, γ), $\boldsymbol{\sigma}^{(\beta,\gamma)}$, is then calculated using the generalized Hooke's law:

$$\boldsymbol{\sigma}^{(\beta,\gamma)} = \boldsymbol{C}^{(\beta,\gamma)}(\boldsymbol{\varepsilon}^{(\beta,\gamma)} - \boldsymbol{\varepsilon}^{\boldsymbol{I}(\beta,\gamma)} - \boldsymbol{\varepsilon}^{\boldsymbol{th}(\beta,\gamma)}) \tag{3.2-3}$$

Once the subcell stress tensor, $\boldsymbol{\sigma}^{(\beta,\gamma)}$, is known, the global RUC stress tensor, $\bar{\boldsymbol{\sigma}}$, is then determined via homogenization

$$\bar{\boldsymbol{\sigma}} = \frac{1}{h_{tot} l_{tot}} \sum_{\beta=1}^{\boldsymbol{N_\beta}} \sum_{\gamma=1}^{\boldsymbol{N_\gamma}} \boldsymbol{\sigma}^{(\beta,\gamma)} h_\beta \, l_\gamma \tag{3.2-4}$$

where h_{tot} and l_{tot} denote the total lengths of the RUC in the 2- and 3-directions, h_β and l_γ denote the subcell dimensions in the 2- and 3-directions, and N_β and N_γ denote the total number of subcells in the 2- and 3-directions.

Expressions for the effective RUC stiffness matrix, $\bar{\boldsymbol{C}}$, the effective RUC inelastic strain tensor, $\bar{\boldsymbol{\varepsilon}}^{\boldsymbol{I}}$, and the effective RUC thermal strain tensor, $\bar{\boldsymbol{\varepsilon}}^{\boldsymbol{th}}$, are determined by substituting Equation 3.2-2 into Equation 3.2-3 to obtain an expression for the local subcell stress tensor, $\boldsymbol{\sigma}^{(\beta,\gamma)}$, in terms of the average total strain applied to the RVE, $\bar{\boldsymbol{\varepsilon}}$, and the concentration submatrices corresponding to the subcell (β, γ)), $\boldsymbol{A}^{(\beta,\gamma)}$ and $\boldsymbol{D}^{(\beta,\gamma)}$. The resulting expression is then substituted into Equation (3.2-4), resulting in:

$$\bar{\boldsymbol{\sigma}} = \frac{1}{h_{tot} l_{tot}} \sum_{\beta=1}^{\boldsymbol{N_\beta}} \sum_{\gamma=1}^{\boldsymbol{N_\gamma}} \boldsymbol{C}^{(\beta,\gamma)}(\boldsymbol{A}^{(\beta,\gamma)}\bar{\boldsymbol{\varepsilon}} + \boldsymbol{D}^{(\beta,\gamma)}(\boldsymbol{\varepsilon}_{\boldsymbol{S}}^{\boldsymbol{I}} + \boldsymbol{\varepsilon}_{\boldsymbol{S}}^{\boldsymbol{th}}) - \boldsymbol{\varepsilon}^{\boldsymbol{I}(\beta,\gamma)} - \boldsymbol{\varepsilon}^{\boldsymbol{th}(\beta,\gamma)}) h_\beta \, l_\gamma \tag{3.2-5}$$

The effective RUC stiffness matrix, $\overline{\boldsymbol{C}}$, the effective RUC inelastic strain tensor, $\bar{\boldsymbol{\varepsilon}}^{I}$, and the effective RUC thermal strain tensor, $\bar{\boldsymbol{\varepsilon}}^{\boldsymbol{th}}$, are then identified comparing Equation 3.2-5 with the effective RUC constitutive law and collecting the respective terms associated with the total, inelastic, and thermal effects:

$$\bar{\boldsymbol{\sigma}} = \overline{\boldsymbol{C}}(\bar{\boldsymbol{\varepsilon}} - \bar{\boldsymbol{\varepsilon}}^{I} - \bar{\boldsymbol{\varepsilon}}^{\boldsymbol{th}}) \tag{3.2-6}$$

$$\overline{\boldsymbol{C}} = \frac{1}{h_{tot} l_{tot}} \sum_{\beta=1}^{\boldsymbol{N_\beta}} \sum_{\gamma=1}^{\boldsymbol{N_\gamma}} \boldsymbol{C}^{(\beta,\gamma)} \boldsymbol{A}^{(\beta,\gamma)} h_\beta \, l_\gamma \tag{3.2-7}$$

$$\bar{\boldsymbol{\varepsilon}}^{I} = \frac{-\overline{\boldsymbol{S}}}{h_{tot} l_{tot}} \sum_{\beta=1}^{\boldsymbol{N_\beta}} \sum_{\gamma=1}^{\boldsymbol{N_\gamma}} \boldsymbol{C}^{(\beta,\gamma)} (\boldsymbol{D}^{(\beta,\gamma)} \boldsymbol{\varepsilon}_{\boldsymbol{S}}^{\boldsymbol{I}} - \boldsymbol{\varepsilon}^{\boldsymbol{I}(\beta,\gamma)}) h_\beta \, l_\gamma \tag{3.2-8}$$

$$\bar{\boldsymbol{\varepsilon}}^{\boldsymbol{th}} = \frac{-\overline{\boldsymbol{S}}}{h_{tot} l_{tot}} \sum_{\beta=1}^{\boldsymbol{N_\beta}} \sum_{\gamma=1}^{\boldsymbol{N_\gamma}} \boldsymbol{C}^{(\beta,\gamma)} (\boldsymbol{D}^{(\beta,\gamma)} \boldsymbol{\varepsilon}_{\boldsymbol{S}}^{\boldsymbol{th}} - \boldsymbol{\varepsilon}^{\boldsymbol{th}(\beta,\gamma)}) h_\beta \, l_\gamma \tag{3.2-9}$$

In Equations 3.2-8 and 3.2-9, $\overline{\boldsymbol{S}} = \overline{\boldsymbol{C}}^{\boldsymbol{-1}}$ is the effective compliance matrix of the RUC. For more information regarding GMC and its formulation, the reader is referred to Aboudi et al. (2012).

In the simulation results presented in the next section, the extended version of the Goldberg model (Goldberg et al., 2005) presented in the last section is used to compute the viscoplastic strain rates in the matrix subcells, $\dot{\boldsymbol{\varepsilon}}^{\boldsymbol{I}(\beta,\gamma)}$, which are integrated forward in time to determine the local viscoplastic strains. The rates of heat generation due to the adiabatic conversion of inelastic work to heat are also computed at the matrix constituent level according to the adiabatic heat energy equation:

$$\dot{T}^{(\beta,\gamma)} = \frac{\beta \boldsymbol{\sigma}^{(\beta,\gamma)} : \dot{\boldsymbol{\varepsilon}}^{\boldsymbol{I}(\beta,\gamma)}}{\rho^{(\beta,\gamma)} C^{(\beta,\gamma)}} \tag{3.2-10}$$

Equation 3.2-10 is the same as Equation 2.4-4 in Chapter 2, except in the context of the GMC (Aboudi et al., 2012) micromechanics model it is applied at the subcell level. The local rates of heat generation computed using Equation 3.2-10 are integrated forward in time to compute local adiabatic temperature rises in the matrix subcells. It is noted that, while the same local density and specific heat, $\rho^{(\beta,\gamma)}$ and $C^{(\beta,\gamma)}$, are used for each of the matrix subcells, the local stress tensor, $\boldsymbol{\sigma}^{(\beta,\gamma)}$, and inelastic strain rate tensor, $\dot{\boldsymbol{\varepsilon}}^{\boldsymbol{I}(\beta,\gamma)}$, and therefore the rate of heat generation given by Equation 3.2-10 will in general be different in each subcell. The RUC average temperature, $\bar{T}$, is computed by volume averaging the local temperatures of the subcells in the RUC according to the following equation:

$$\bar{T} = \frac{1}{h_{tot} l_{tot}} \sum_{\beta=1}^{\boldsymbol{N_\beta}} \sum_{\gamma=1}^{\boldsymbol{N_\gamma}} T^{(\beta,\gamma)} h_\beta \, l_\gamma \tag{3.2-11}$$

3.2.2 Results and Discussion – Unidirectional Composite Response

The effects of adiabatic heating on the axial tensile, axial compressive, transverse tensile, transverse compressive, and in-plane shear response of a unidirectional composite are investigated in this section. Simulation results are presented for a T700/E862 unidirectional composite with a 60% fiber volume fraction at strain rates of 100 s^{-1} and 1000 s^{-1}. The T700 fiber properties used in the simulations are presented in Table 3.2.1 (Cater et al., 2015). The fibers are modeled as transversely isotropic and linear elastic and their material properties are assumed to not vary with temperature. The properties used for the matrix subcells are given in Table 2.7.1 in the previous chapter. It is noted that,

currently, there is no unidirectional T700/E862 composite test data available; this material system was selected due to the availability of fiber and matrix material properties and experimental data (for E862). To examine qualitatively the effects of adiabatic heating, simulations were also conducted with a nonzero inelastic heat fraction. Both isothermal ($\beta = 0$) and adiabatic simulations are presented in this section. The inelastic heat fraction has been set to unity (i.e., all plastic work is assumed to be converted to heat) for all the nonisothermal results that follow. This implies that the simulated temperature rises in this section represent an upper bound, though Garg et al. (2008) found experimentally that nearly all the inelastic work was converted to heat in high strain rate uniaxial compression of polycarbonate, implying that assuming an inelastic heat fraction of unity may be fairly accurate for adiabatic conditions. It is noted that damage and failure are not included in the simulations in this section; all nonlinearity is due to inelasticity.

Table 3.2.1: T700 Carbon Fiber Elastic Properties

Axial Young's Modulus	230 GPa
Transverse Young's Modulus	15 GPa
Axial Poisson's Ratio	0.2
Transverse Poisson's Ratio	0.3
In-Plane Shear Modulus	27 GPa

The simulated room temperature (25°C) response of the unidirectional composite subjected to axial tensile and axial compressive loading is presented in Figures 3.2-2 and 3.2-3 respectively. Linear elastic response is observed for both strain rates in both loading cases. Since the axial tensile/compressive response of a unidirectional composite is fiber dominated, no significant thermal softening is observed due to adiabatic heating in the matrix.

a)

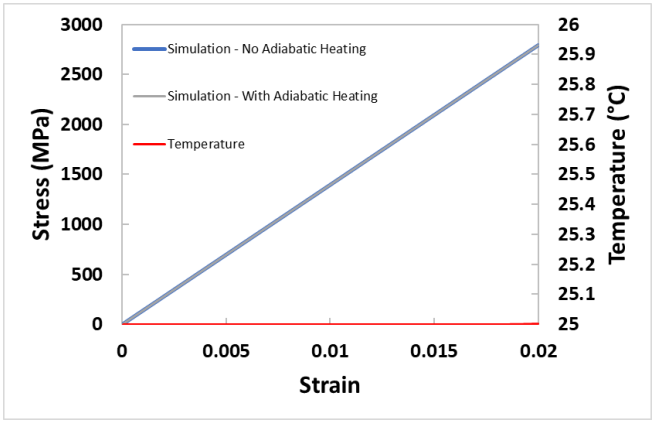

b)

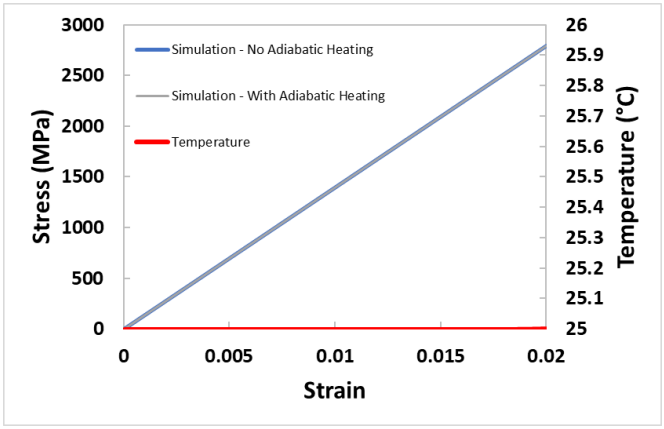

Figure 3.2-2: Simulated Response of Unidirectional Composite Subjected to Axial Tensile Loading at Strain Rates of a) 100 s^{-1} and b) 1000 s^{-1}

a)

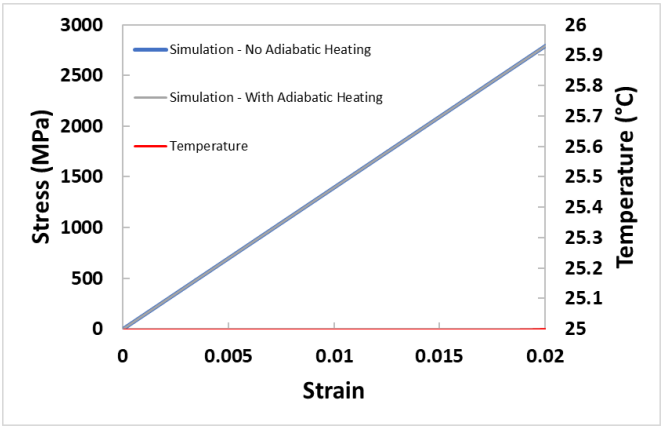

b)

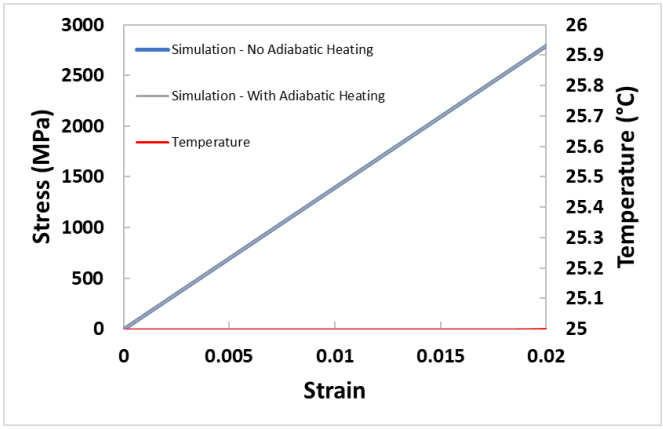

Figure 3.2-3: Simulated Response of Unidirectional Composite Subjected to Axial Compressive Loading at Strain Rates of a) 100 s^{-1} and b) 1000 s^{-1}

The simulated response of the unidirectional composite subjected to transverse tensile loading at strain rates of 100 s^{-1} and 1000 s^{-1} at room temperature is shown in Figures 3.2-4a) and 3.2-4b), respectively. The response of the unidirectional composite subjected to transverse compressive loading at the same strain rates is shown in Figures 3.2-5a and 3.2-5b. Since the transverse tensile and compressive response of a unidirectional composite is matrix dominated, significant adiabatic heating and thermal softening are observed for both transverse tensile (Figure 3.2-4) and compressive (Figure 3.2-5) loading. The RUC average temperature rises for the 100 s^{-1} and 1000 s^{-1} strain rate transverse tension simulations were 21.60°C and 25.12°C, respectively, whereas the maximum local (subcell level) temperature rises were 94.92°C and 110.33°C. The RUC average temperature rises for the 100 s^{-1} and

1000 s^{-1} strain rate transverse compression simulations were 27.12°C and 31.20°C, respectively, whereas the maximum local (subcell level) temperature rises were 117.36°C and 132.48°C. It is evident that, for the same strain rate and level of total deformation, the transverse compression simulations exhibited larger temperature rises than the transverse tension simulations. It is evident from Figures 3.2-4 and 3.2-5 that the tension-compression asymmetry in the composite response is captured in the simulations; the magnitude of the transverse compressive saturation stress is larger than the transverse tensile saturation stress.

a)

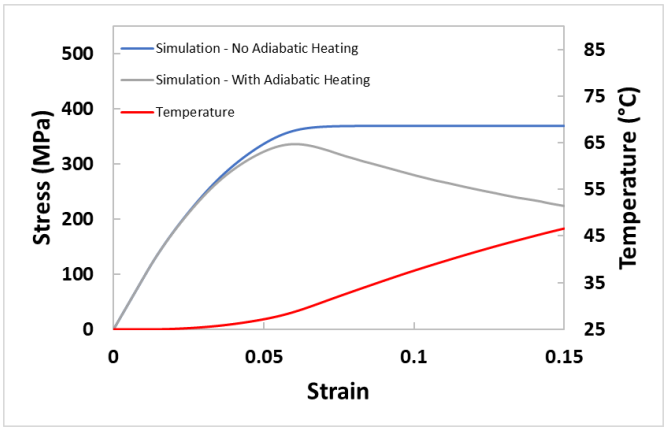

b)

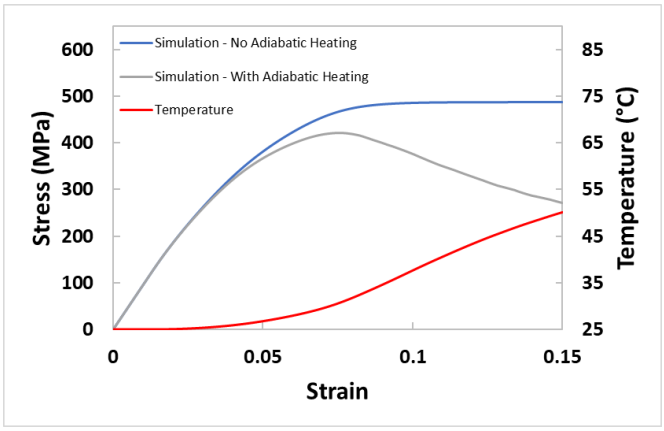

Figure 3.2-4: Simulated Response of Unidirectional Composite Subjected to Transverse Tensile Loading at Strain Rates of a) 100 s^{-1} and b) 1000 s^{-1}

a)

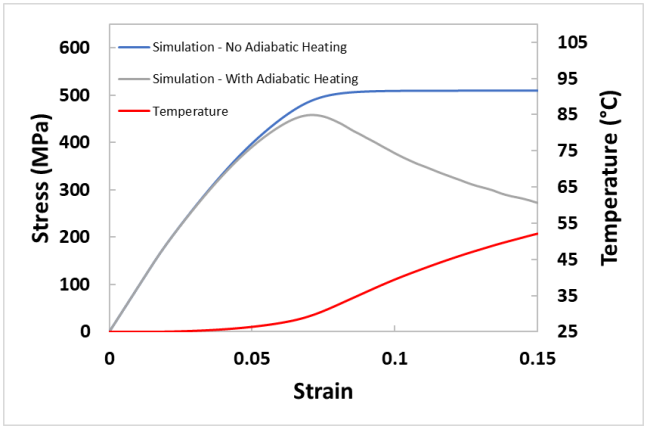

b)

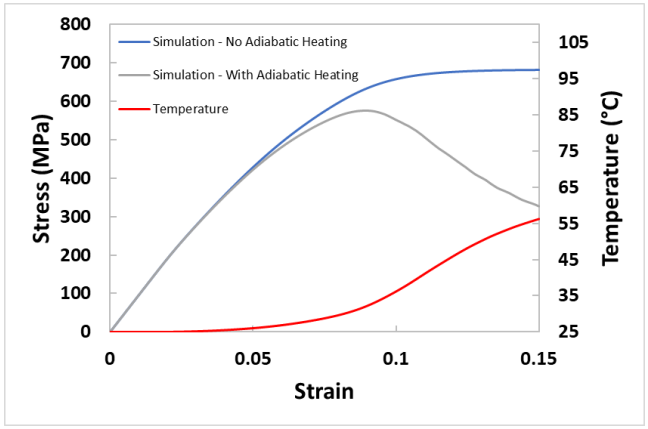

Figure 3.2-5: Simulated Response of Unidirectional Composite Subjected to Transverse Compression Loading at Strain Rates of a) 100 s^{-1} and b) 1000 s^{-1}

Figures 3.2-6a and 3.2-6b show the simulated response of the unidirectional composite subjected to in-plane shear loading at room temperature at engineering shear strain rates of 100 s^{-1} and 1000 s^{-1}, respectively. Significant thermal softening due to adiabatic heating in the matrix is observed. The RUC average temperature rises for the 100 s^{-1} and 1000 s^{-1} engineering shear strain rate simulations were 9.79°C and 11.51°C, respectively. The maximum local (subcell level) temperature rises were 48.37°C and 58.75°C.

a)

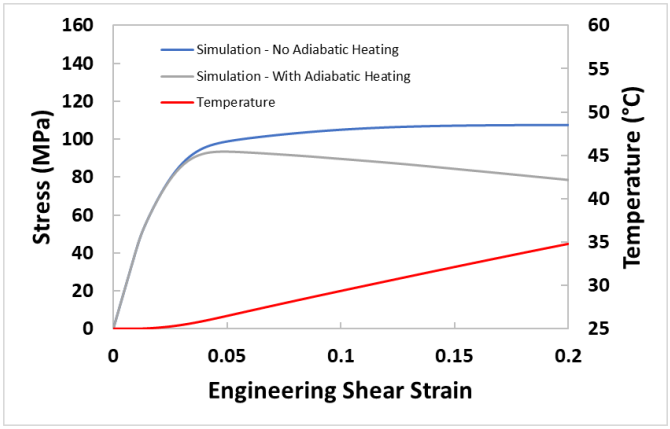

b)

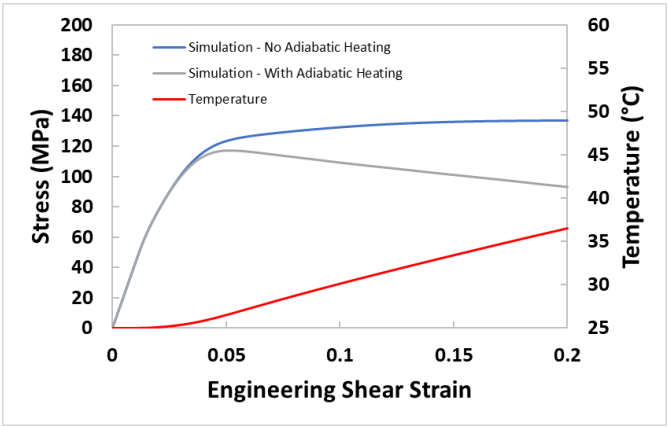

Figure 3.2-6: Simulated Response of Unidirectional Composite Subjected to In-Plane Shear Loading at Strain Rates of a) 100 s^{-1} and b) 1000 s^{-1}

3.2.3 Conclusions

The improved version of the Goldberg (Goldberg et al., 2005) model developed in the previous chapter was used as a constitutive model in the GMC micromechanics framework to computationally investigate the effects of adiabatic heating on the response of a T700/E862 unidirectional composite with a 60% fiber volume fraction under various loading conditions. The adiabatic heat energy equation (Equation 3.2-10) was used to compute temperature rises due to the conversion of inelastic work to heat at the subcell level based on the local plastic power density, local density, and local specific heat of each of the matrix subcells. Significant thermal softening due to adiabatic heating was observed

for simulated transverse tensile, transverse compressive, and in-plane shear loading whereas a nominal amount of thermal softening was observed in simulated longitudinal tensile and longitudinal compressive loading cases. These results are consistent with experimental observations in flat panel impact tests conducted on triaxially braided PMCs (Johnston et al., 2018), where local regions of impact induced adiabatic heating have been observed in resin-rich regions (Johnston et al., 2018). In the next part of this chapter, the GMC micromechanics model, including the viscoplasticity formulation presented in Chapter 2, is implemented into the commercial transient dynamic FE code LS-DYNA as a UMAT and used to simulate quasi-static tensile tests and a flat panel impact test conducted on T700/E862 [0°/60°/–60°] triaxially braided composite. The UMAT is used in the context of a subcell-based modeling approach to approximate the mesoscale composite braid architecture as an assemblage of laminated composite subcells.

3.3 Multiscale Modeling of Triaxially Braided Polymer Matrix Composites Using a Subcell-Based Approach

Though several constitutive models exist in LS-DYNA (Hallquist, 2006) for composite material analysis, many of them have shortcomings that deem them incapable of simultaneously modeling all the phenomena of interest in an impact event: complex interaction between the constituent materials (fiber and matrix); adiabatic heating and subsequent thermal softening in the rate, temperature, and pressure dependent polymer matrix; tension-compression asymmetry; material nonlinearity due to a combination of matrix progressive damage and inelasticity; ultimate failure. To account for the interaction between constituent materials at the microscale, a micromechanics-based constitutive model must be used. However, the only micromechanics-based composite model in LS-

DYNA is MAT_235 (Micromechanics Dry Fabric). This model was developed by Tabiei and Ivanov (2002) and Ivanov and Tabiei (2004) to model the elastic response of loose dry fabric, including yarn reorientation effects, not woven or braided composites (Cousigné et al., 2014). The MAT_058 and MAT_158 (Laminated Composite Fabric and Rate Sensitive Composite Fabric) material models are continuum-level models based on the work of Matzenmiller et al. (1995). They are suitable for modeling woven fabric laminates and are capable of simulating nonlinear behavior in all material directions. These models have been used in PMC impact analyses (Littell, 2008; Blinzler, 2012; Carney et al., 2013), though failure strains determined from quasi-static coupon tests often need to be adjusted to correlate to experimentally measured ballistic limits. In MAT_058 and MAT_158, all material nonlinearity is due to damage evolution rather than a combination of inelasticity and damage; since plastic strains are not computed, these models are incapable of simulating temperature rises due to the conversion of plastic work to heat. Though developed to model the rate dependent response of metals, an orthotropic material model that is capable of modeling temperature rises due to inelastic deformation is MAT_264 (Tabulated Johnson Cook Orthotropic Plasticity), which is based on the Johnson-Cook (Meyers, 1994) plasticity model. Since plastic deformation in metals is assumed to be deviatoric, this model is not applicable to the analysis of PMCs, for which the matrix response exhibits a significant dependence on hydrostatic pressure.

Since none of the composite material models currently available in LS-DYNA are capable of modeling all the phenomena of interest, the micromechanics model described in the first part of this chapter has been implemented into LS-DYNA as a UMAT, where it is used in the context of a subcell-based approach to approximate the heterogeneity of a

triaxially braided PMC at the highest analysis length scale. In the remainder of this chapter, the subcell methodology (Littell, 2008; Blinzler, 2012; Cheng and Binienda, 2008; Li et al., 2009; Goldberg et al., 2012; Xiao et al., 2011; Cater et al., 2014; Cater et al., 2015) is described and applied to a representative triaxially braided PMC. Straight-sided quasi static coupon tests as well as a flat panel impact test conducted at NASA Glenn Research Center are simulated with the developed UMAT and compared to available experimental data.

3.3.1 Subcell Methodology

The material system under investigation in this chapter is a T700/Epon 862 [0°/60°/–60°] triaxially braided composite. Epon 862 is a low viscosity, high flow thermoset epoxy resin (Littell, 2008; Littell et al., 2008) and T700 is a high strength carbon fiber manufactured by Toray. The triaxially braided carbon fiber preform (no resin), shown in Figure 3.3-1a, consists of 24K tows in the axial direction (red arrow) and 12K tows in the bias/braider (blue arrows) directions. Braided tow architectures are known to be resistant to failures driven by interlaminar stresses (Cater et al., 2015) and the particular [0°/60°/–60°] triaxial braid considered herein is known to approximately exhibit quasi-isotropic elastic properties (Littell, 2008; Kohlman, 2012). Due to the relatively large RUC compared to the size of structural components (dimensions shown in Figure 3.3-1b), the deformation and progressive damage behavior of the triaxial braid is a function of the material architecture. To account for the material heterogeneity at the highest analysis length scale, a subcell-based approach (Littell, 2008; Blinzler, 2012; Cheng and Binienda, 2008; Li et al., 2009; Goldberg et al., 2012; Xiao et al., 2011; Cater et al., 2014; Cater et al., 2015) is utilized, whereby the braided composite RUC is discretized into an assemblage of adjacent UD composites, with stacking sequences determined from the braid architecture. The subcell methodology, illustrated in

Figure 3.3-1, consists of identifying the braided composite RUC and discretizing it in-plane into a series of mesoscale subcells depending on the presence of axial and/or braider tows or lack thereof. The mesoscale subcells are then discretized through their thicknesses into an approximation of UD plies with layups determined by the braid architecture. It can be seen in Figure 3.3-1d that subcells A and C have antisymmetric stacking sequences whereas subcells B and D have symmetric stacking sequences. The RUC discretization shown in Figure 3.3-1d was developed by Cater et al. (2015) and is known as the absorbed matrix model (AMM) because pure matrix layers are not explicitly modeled; braider plies are assumed to be a homogenized representation of braider tows and surrounding pure matrix regions (Cater et al., 2014; Cater et al., 2015).

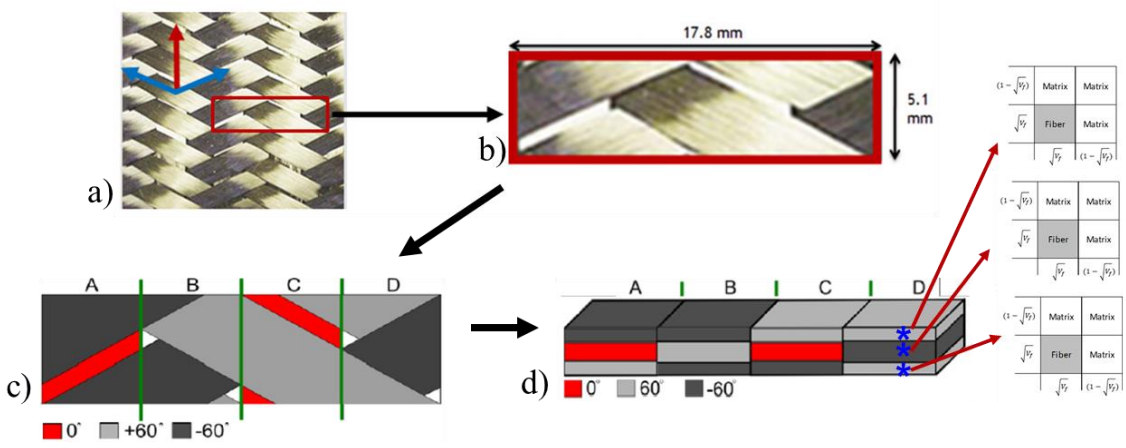

Figure 3.3-1: a) Triaxially Braided PMC Mesoscale RUC Identification; b) Enlarged Image of Identified RUC with Dimensions Shown; c) Identification of Four Adjacent Subcell Regions; d) Through-Thickness Discretization of Each Mesoscale Subcell into an Approximation of Unidirectional Plies

Figure 3.3-2 shows a coarse FE mesh of the triaxially braided RUC (Figure 3.3-1d), where each mesoscale subcell has been modeled in LS-DYNA (Hallquist, 2006) as a single thick shell element with three through thickness integration points, each corresponding to a UD ply. Thick shells have the advantage over 2D shell elements in that they are able to

admit a full 3D stress state, which is crucial in impact problems, where large transverse normal and transverse shear stresses are expected. It is noted that previous versions of the subcell model employed 2D shell elements (Littell, 2008; Blinzler, 2012; Cheng and Binienda, 2008; Li et al., 2009; Goldberg et al., 2012; Xiao et al., 2011; Cater et al., 2014; Cater et al., 2015). All material properties and model constants used in the analyses that follow have been presented in previous chapters.

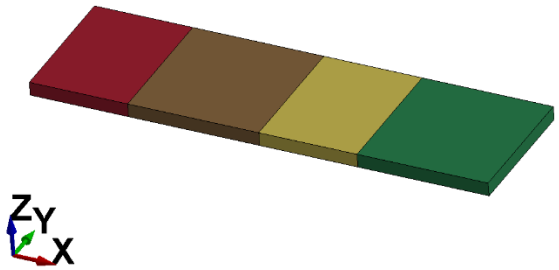

Figure 3.3-2: Coarse Finite Element Mesh of Triaxially Braided RUC; Each Thick Shell Element Represents One Subcell and Consists of Three Through-Thickness Integration Points

The synergistic multiscale approach taken in this chapter to model the triaxially braided PMC differs from previous subcell models (Littell, 2008; Blinzler, 2012; Cheng and Binienda, 2008; Li et al., 2009; Goldberg et al., 2012; Xiao et al., 2011; Cater et al., 2014; Cater et al., 2015) in that the nonlinear constitutive behavior of each UD ply in the laminated composite subcells (Figures 3.3-1c and 3.3-1d) is represented using the aforementioned UMAT. As such, in the current work, there is a two-way (i.e., combined top-down/bottom-up) information transfer between the microscale, mesoscale, and macroscales. In contrast, previous versions of the subcell methodology utilized a bottom-up hierarchical micromechanics approach to determine the elastic properties of the UD plies in the each subcell of the mesoscale RUC. While computationally efficient, a major

drawback of this bottom-up approach is that it does not allow the UD ply, laminated composite subcells, or the mesoscale RUC elastic properties to change with strain rate in an impact simulation. Due to the bottom-up nature, the elastic properties of the UD plies in previous subcell models are fixed (i.e., constant) once values that correlate well with the stiffnesses of quasi-static coupon tests are determined. As such, once these properties are determined, there is a two-way (top-down/bottom-up) information transfer between the mesoscale and macroscales, but the microscale is effectively disregarded once the bottom-up approach is used to determine the properties of the UD plies, which are modeled as smeared homogeneous continua in previous subcell models. This is likely inaccurate for high strain rate analyses considering the rate-, temperature-, and pressure-dependence, as well as the effects of adiabatic heating, are primarily due to the matrix. This also implies the UD ply elastic properties in previous subcell models correspond to their quasi-static values, which will undoubtedly be inaccurate for an impact problem given that the strain rate dependence of PMCs is primarily due to the rate dependence of the polymer matrix. Consider the E862 matrix properties presented in Table 2.7.1 in Chapter 2. For a temperature of 30°C, the DMA shifting methodology described in Section 2.5 results in E862 elastic modulus values of 2.9 GPa and 3.65 GPa for effective strain rates of 10^{-3} s^{-1} and 1000 s^{-1}, respectively; the elastic modulus increases by 22.9% from its value associated with the quasi-static strain rate of 10^{-3} s^{-1} to the dynamic strain rate of 1000 s^{-1}. In the synergistic approach taken herein, the fact that there is a two-way flow of information down to the microscale allows the properties of the matrix, and subsequently the properties of the UD plies in laminated composite subcells as well as the mesoscale RUC to be

determined automatically for any strain rate once the DMA shift factor described in Section 2.5 has been calibrated based on neat resin data.

3.3.2 Microstructure Quantification and RUC Development

To determine the mesoscale subcell UD layer dimensions and fiber volume fractions, serial sectioning and optical microscopy was performed on samples cut from a pristine triaxially braided composite panel obtained from NASA Glenn Research Center. The panel consisted of the same [0°/60°/–60°] triaxially braided preform as the T700/E862 material system, but a different matrix (Cycom PR520) material. It is assumed that microscopy measurements of the T700/PR520 material system are representative of the T700/E862 material system. The panel was 3.175 mm thick and consisted of six layers of triaxially braided preform through the thickness. Since the mesoscale RUC is representative of one layer of the triaxial braid, its total height is 0.53 mm (i.e., one sixth of the total panel thickness).

The widths of the UD mesoscale subcell layers were determined via optical microscopy. Three images of the mesostructure of the triaxial braid were taken and are shown in Figure 3.3-3. Measurements of the widths of the axial tows were taken from these mesostructural images. The average width of the axial tows was 5.626 mm, which was taken as the width of subcells A and C. Based on the total width of the RUC (17.78 mm), the width of subcells B and D were taken as 3.264 mm.

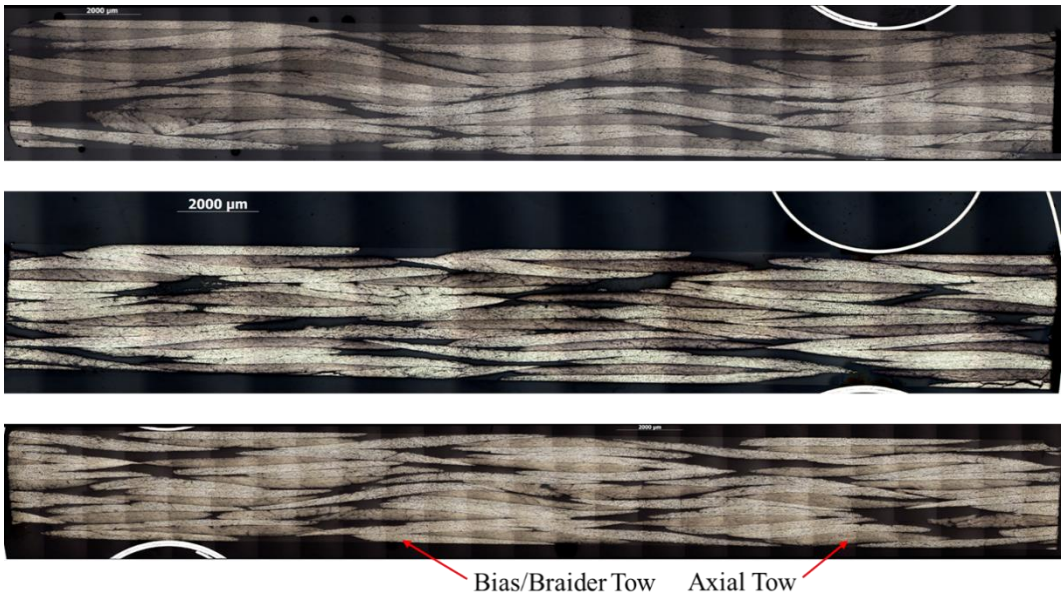

Figure 3.3-3: T700/PR520 Mesostructure Used for Determination of Subcell Widths

The fiber volume fractions of the UD mesoscale subcell layers were also determined via optical microscopy. Figure 3.3-4 shows three micrographs of various locations in the axial tows. A total of 261 micrographs were taken and an image processing code was developed in MATLAB to compute the fiber volume fraction of each micrograph using a simple approach based on threshold pixel intensity.

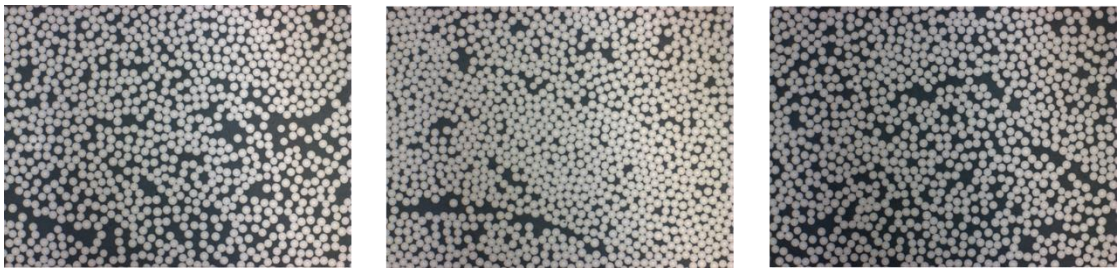

Figure 3.3-4: T700/PR520 Intratow Micrographs (Taken Within Axial Tows)

The axial volume fraction data was fit to a log normal distribution since the fiber volume fraction cannot be negative valued. The probability density and cumulative distribution functions for the axial tow fiber volume fraction are shown in Figures 3.3-5 and 3.3-6. The mean and standard deviation of the axial tow fiber volume fraction were 65.6% and 4.94%,

respectively. The mean value of 65.6% was used for the axial tows in the AMM (Cater et al., 2014; Cater et al., 2015) subcell discretization (Figure 3.3-1). It is noted that in the modeling results presented in this section, the fiber volume fraction of the axial tows is deterministic.

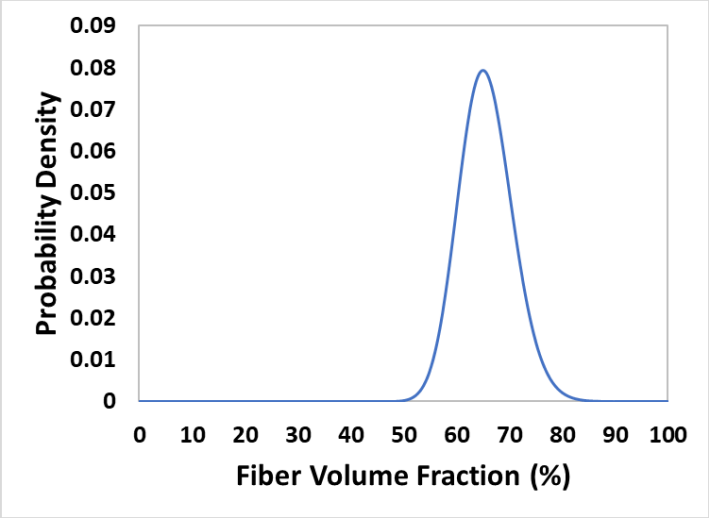

Figure 3.3-5: Probability Density Function for Axial Tow Fiber Volume Fraction

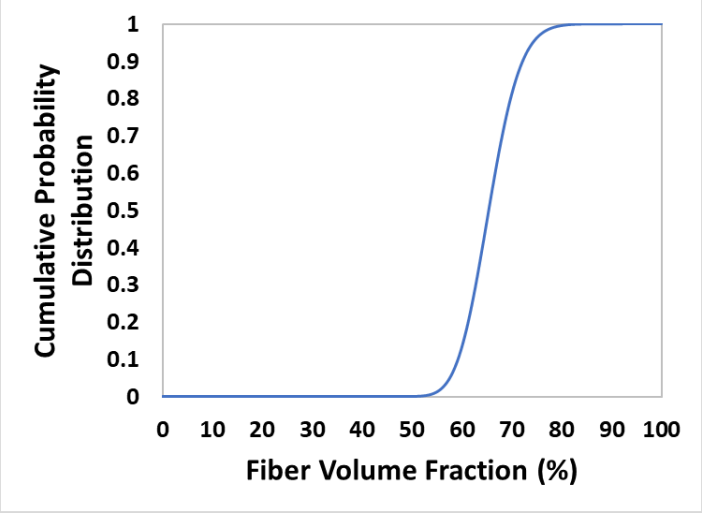

Figure 3.3-6: Cumulative Distribution Function for Axial Tow Fiber Volume Fraction

To determine the fiber volume fractions of the braider tows in mesoscale subcells A/C and B/D, knowledge of the subcell dimensions and total composite fiber volume

fraction of 56% were utilized. It is also assumed that the middle UD layers of the mesoscale subcells are twice the thickness as the outer layers. Based on the microscopy-informed assumption that mesoscale subcells A and C each have a fiber volume fraction of 60%, the fiber volume fraction of the braider tows in subcells A and C ($V_{f,bAC}$) is computed as follows:

$$V_{f,bAC} = \frac{V_{f,AC} - h_{aAC}V_{f,aAC}}{2h_{bAC}} \tag{3.3-1}$$

where $V_{f,aAC}$ & $V_{f,AC}$ are the fiber volume fractions of the axial tows in subcell A/C and h_{aAC} & h_{bAC} are the heights of the axial and braider tows in mesoscale subcell A/C divided by the total RUC height. The fiber volume fraction of subcell B/D, $V_{f,BD}$, is then computed to ensure a total RUC fiber volume fraction of 56% as follows:

$$V_{f,BD} = \frac{V_{f,RUC}(W_{AC} + W_{BD}) - W_{AC}V_{f,AC}}{W_{BD}} \tag{3.3-2}$$

where $V_{f,RUC}$ is the fiber volume fraction of the mesoscale RUC (56%) and W_{AC} & W_{BD} are the widths of subcells A/C and B/D, respectively. It is assumed that the fiber volume fraction of all the UD layers in mesoscale subcells B and D have the same fiber volume fraction ($V_{f,BD}$). The UD ply thicknesses and fiber volume fractions are summarized in Table 3.3.1.

Table 3.3.1: Summary of Unidirectional Ply Volume Fractions and Ply Thicknesses

Subcell A Layup	*Braid Angle*	*Fiber Vf (%)*	*Thickness (%)*
Braider Tow	-60°	54.4	25
Axial Tow	0°	65.6	50
Braider Tow	60°	54.4	25
Subcell B Layup	*Braid Angle*	*Fiber Vf (%)*	*Thickness (%)*
Braider Tow	-60°	49.1	25
Braider Tow	60°	49.1	50
Braider Tow	-60°	49.1	25
Subcell C Layup	*Braid Angle*	*Fiber Vf (%)*	*Thickness (%)*
Braider Tow	60°	54.4	25
Axial Tow	0°	65.6	50
Braider Tow	-60°	54.4	25
Subcell D Layup	*Braid Angle*	*Fiber Vf (%)*	*Thickness (%)*
Braider Tow	60°	49.1	25
Braider Tow	-60°	49.1	50
Braider Tow	60°	49.1	25

[a]Shown as percent of overall subcell thickness

3.3.3 Fiber Failure

Two different existing methods of modeling fiber failure are considered. The first method is a simple maximum stress criterion, which is applied to microscale fiber subcells. Once the longitudinal tensile stress in the fiber reaches the specified fiber tensile strength, all the stiffness components are reduced to nominal values ($1/10{,}000^{th}$ of their initial values). The fibers have only been permitted to fail due to longitudinal tensile stress.

In a longitudinal tensile test on a UD composite, the individual fibers will generally fail progressively due to the variation in their individual tensile strengths. However, employing a microscale RUC (Figure 3.2-1) with a statistically significant number of fiber subcells would be prohibitively computationally expensive for use in explicit FE simulations. It is therefore desirable to model the single fiber in the microscale RUC as an effective fiber, where the stiffness is progressively reduced to reflect the failure of individual fibers. The existing Curtin (1991) model is adopted in this research for this purpose. The model, which

is based on fiber Weibull strength statistics combined with a shear lag analysis, specifies the following relationship between the damaged, E_f^*, and undamaged, E_f, fiber longitudinal modulus:

$$E_{1f}^* = \frac{1}{2}\left\{1 + \exp\left[-\left(\frac{\sigma_L}{\sigma_C}\right)^{m+1}\right]\right\} E_{1f} \tag{3.3-3}$$

$$\sigma_C = \left(\frac{\sigma_0^m \tau L_o}{r}\right)^{\frac{1}{m+1}} \tag{3.3-4}$$

where σ_L is the fiber longitudinal stress. The Curtin (1991) model parameters are the gauge length, L_0, characteristic strength, σ_0, Weibull modulus, m, and the fiber-matrix interfacial frictional sliding resistance, τ. The corresponding failure strain and strength of the model are given by:

$$\varepsilon_1^u = \frac{\sigma_C}{E_{1f}} h^{\left(\frac{1}{m+1}\right)} \tag{3.3-5}$$

$$\sigma_{1f}^u = \frac{1}{2}\sigma_C h^{\left(\frac{1}{m+1}\right)}[1 + \exp(-h)] \tag{3.3-6}$$

where h is the lowest positive value that satisfies the following equation:

$$1 + [1 - (m+1)h]\exp(-h) = 0 \tag{3.3-7}$$

Once the longitudinal tensile fiber stress reaches the maximum stress, σ_{1f}^u, the fiber moduli are reduced to 1/10,000th of their initial values. The values of L_0, σ_0, m used in the simulations to follow are 8 mm, 4.41 GPa, and 12.06, respectively, and were obtained from the fiber strength data presented in Zhou et al. (2010). The value of the interfacial sliding resistance in the Curtin (1991) model, τ, and the fiber strength for the maximum stress

failure criterion are calibrated based on quasi-static coupon level test data, which is described in the next section.

3.3.4 Quasi-Static Straight-sided Coupon Simulation Results and Discussion

In this section, axial and transverse straight-sided coupon tests conducted by Littell (2008) and Littell et al. (2008) are simulated and compared to experimental data. In these tests (Littell, 2008; Littell et al., 2008), axial (0°) and transverse (90°) tension tests, the test specimens were cut such that the axial tows were oriented parallel and perpendicular to the loading direction. The coupons used in the experiments were 304.8 mm in length, 35.8 mm in width, 3.175 mm in thickness, and had a gage length of 203.2 mm. Each physical coupon had six through-thickness layers of triaxially braided preform. The axial and transverse coupon FE meshes, shown in Figure 3.3-7, were spatially discretized with 1920 and 1932 thick shell elements (ELFORM=5) (Guo, 2000; Chatiri et al., 2009), respectively, each with three through-thickness integration points and LS-DYNA type 6 hourglass control (Belytschko and Bindeman, 1993). As aforementioned, each of the three through-thickness integration points corresponds to a UD ply in subcells A, B, C and D of the mesoscale RUC (Figure 3.3-2). Six thick shell elements were used through the thickness to represent each of the six layers of preform in the physical coupons. No contact was used between layers (elements of adjacent layers share nodes) and only the coupon gage sections were modeled. In the simulations, all the nodes of one end of the model were prevented from translating and rotating in all directions whereas the nodes on the other end were only permitted move in the load direction. The nodes permitted to move in the load direction were displaced at a constant rate of 0.0106 mm/sec, the same rate used in the experiments (Littell, 2008; Littell et al., 2008). Due to the nominal nodal accelerations, mass scaling was used to

achieve a reasonable explicit timestep in the FE simulations. It should be noted that a mesh refinement study has not been performed in this work and that, due to the mesh density used in the current models, no through thickness nesting of axial tows could be modeled; in all models, the axial tows in each layer run parallel to and lie directly on top of each other through the thickness.

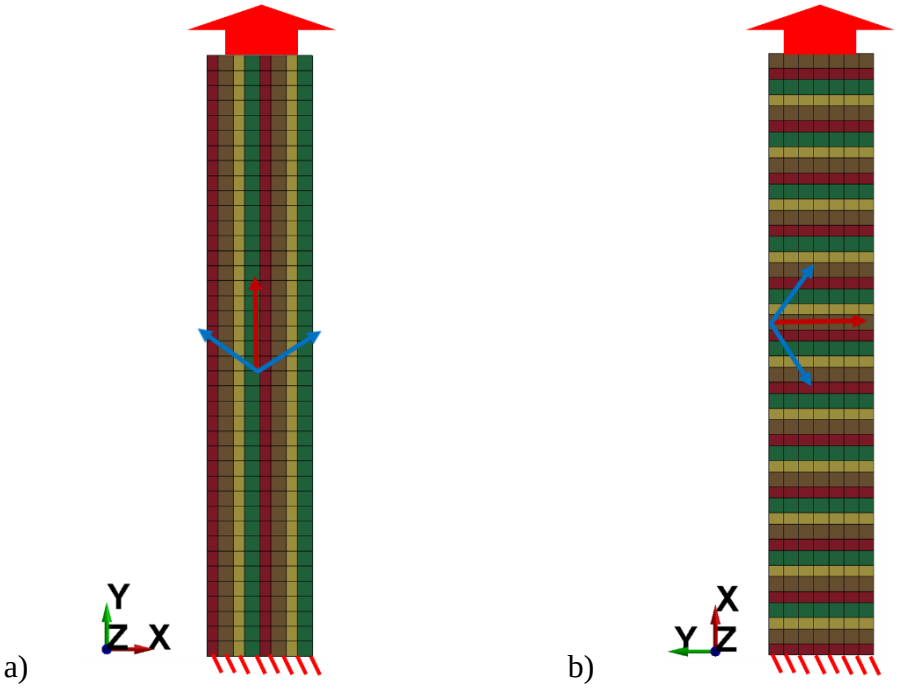

a) b)

Figure 3.3-7: Finite Element Meshes of Straight-Sided a) Axial and b) Transverse Tensile Coupon Gage Sections

The simulated stress-strain curves for the axial and transverse tensile coupon tests superimposed with the experimental data (Littell et al., 2008) are shown in Figures 3.3-8 and 3.3-9. Results are shown for simulations conducted with the maximum stress fiber failure criterion and the Curtin (1991) progressive fiber damage model. Since the quasi-static axial tension test failed due to a longitudinal tensile failure the axial tows, the fiber strength for the maximum stress model, 4.205 GPa, and fiber-matrix interfacial frictional sliding resistance for the Curtin model, 10 MPa, were calibrated such that the failure of the

quasi-static longitudinal tension simulation correlated to the experimental failure strain in the longitudinal tension test. The aforementioned values were used for the fibers in all UD layers (Figure 3.3-1d) of the mesoscale subcell regions (Figure 3.3-1c).

The simulated transverse tensile stress-strain response is initially in agreement with the experimental data, but overpredicts the experimental failure strain and fails to capture the nonlinearity observed in the test after about 0.25% strain, which has been attributed (Kohlman, 2012) to transverse splitting of the tows that terminate at the free edge. Since matrix damage is not considered in the multiscale model, this nonlinearity is not captured in the simulation. It is emphasized that, while the fiber failure properties used in the simulations are calibrated (backed out) based on the failure strain in the axial tensile coupon tests, the simulated elastic stiffness properties are a result of the UD ply fiber volume fractions and ply thicknesses in the triaxial braid subcell discretization in addition to the E862 matrix properties, which were calibrated based on neat resin test data in Chapter 2. The UD ply fiber volume fractions were determined through optical microscopy, as explained in Section 3.3.2, and were not altered to correlate with the experimental elastic stiffnesses. These quasi-static tests can therefore be viewed as: i) validation of the elastic properties resulting from the subcell discretization; ii) calibration of the fiber failure properties.

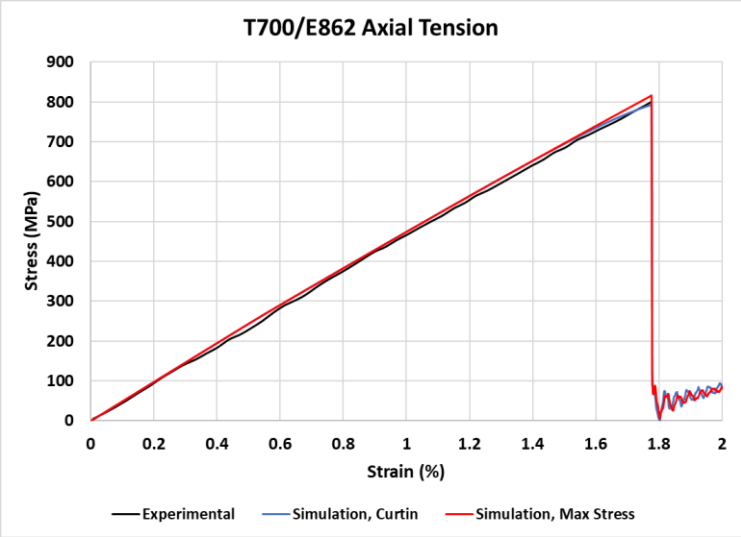

Figure 3.3-8: Simulated and Experimental Axial Tensile Stress-Strain Curves

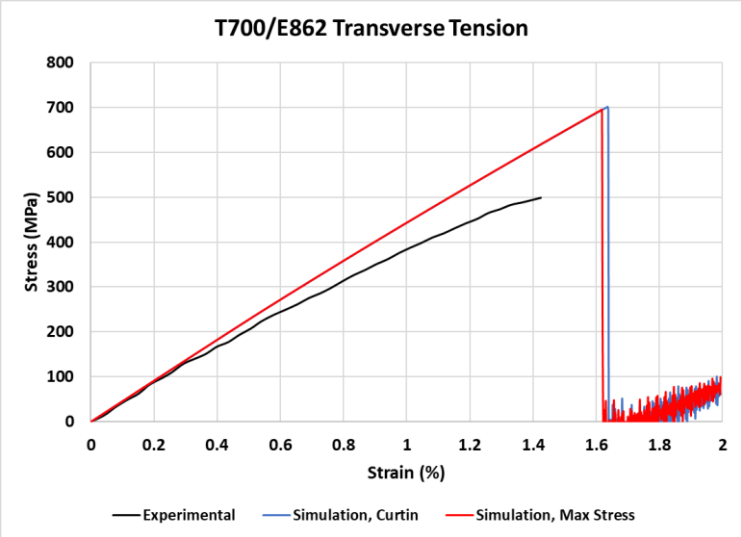

Figure 3.3-9: Simulated and Experimental Transverse Tensile Stress-Strain Curves

3.3.5 Impact Simulation Results and Discussion

As part of an ongoing investigation into the impact response of braided PMC structures, a series of flat panel impact experiments have been conducted by NASA personnel on a variety of triaxially braided composite material systems according to ASTM standard D8101 (ASTM, 2017). The experiments consist of impacting triaxially braided

PMC panels with a cylindrical, spherical nose aluminum projectile. The braided composite panels are square with side lengths of 30.48 cm and a thickness of approximately 3.175 mm. During the impact tests, the braided composite panels are held in place by a circular fixture with an aperture diameter of 25.4 cm by twenty-eight bolts (Pereira et al., 2010; Pereira et al., 2016). The cylindrical section of the semi-hollow aluminum projectile had a radius of 2.53 cm and a wall thickness of 0.76 mm; the front face of the spherical nose had a radius of 3.81 cm and a nose thickness of 0.635 cm; the projectile length was 4.95 cm (Carney et al., 2013). In the impact experiments, digital image correlation (DIC) was used to monitor the strains and displacements of a square section on the back side of the test panels with side lengths of roughly 70 mm (3 inches). More details regarding the impact test setup and projectile geometry can be found in Pereira et al. (2010) and Pereira et al. (2016).

The experimental impact data in this section has been provided by Revilock (2017, personal communication). The impact velocity and initial temperature in the experiment were 163.058 m/s and 21°C, respectfully. The same impact velocity and initial temperature were used in the simulations. Like the straight-sided test coupons, the flat panels consisted of six layers of the triaxially braided perform through the panel thickness. As such, the flat panel mesh was discretized with six through thickness layers of thick shell elements with LS-DYNA type 6 hourglass control (Belytschko and Bindeman, 1993). The panel mesh consisted of 19398 thick shell elements and is shown in Figure 3.3-9. A side view of the FE mesh of the panel and the aluminum projectile are shown in Figure 3.3-9a whereas Figure 3.3-9b shows the back of the plate mesh. To simulate the 25.4 cm diameter fixture used to hold the composite panels, a single point constraint (SPC) was applied to all

translational and rotational degrees of freedom of all nodes outside a 25.4 cm diameter circle; the bolts were not explicitly modeled. The aluminum projectile, which was discretized with 17760 reduced integration solid elements with standard LS-DYNA type 1 viscous hourglass control, was set up to impact the plate at the center of the 25.4 cm diameter circle of unconstrained nodes. The LS-DYNA automatic single surface contact card (*CONTACT_AUTOMATIC_SINGLE_SURFACE) was used to simulate contact between the projectile and panel meshes.

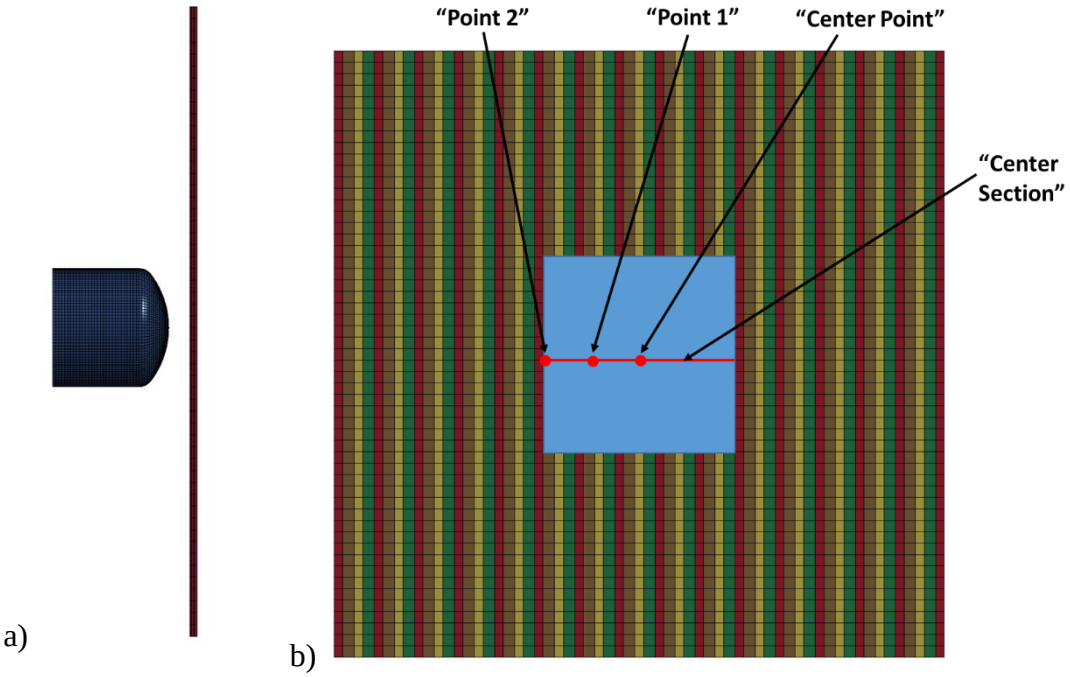

Figure 3.3-10: a) Side View of Plate Mesh with Projectile Mesh Shown; b) Back View of Plate Mesh with DIC Area, Section, and Points Labeled

In Figure 3.3-10b, the blue region on the panel mesh corresponds to the area on the back of the test panel monitored by DIC in the impact tests. Additionally, the out of plane displacement of the points labeled "Point 1", "Point 2", and "Center Point", as well as the "Center Section", are monitored during the experiments. The density, Young's modulus, and Poisson's ratio of the aluminum projectile used in the simulations are 2700 kg/m^3, 74

GPa, and 0.3, respectively. The elastic modulus of the polymer matrix in each microscale subcell is determined (automatically) based on the integration point effective strain rate and the subcell temperature using the DMA shifting methodology described in Chapter 2.

Figures 3.3-11a through 3.3-11c show the simulated and experimental out-of-plane displacement time histories for three points shown in Figure 3.3-10b (Point 1, Point 2, Center Point). Time t=0 ms corresponds to the time the tip of the projectile contacts the plate. Simulations have been conducted using both the maximum stress and Curtin (1991) failure models with inelastic heat fractions of zero (isothermal conditions) and unity (adiabatic conditions with 100% of plastic work converted to heat). Simulation results with no fiber failure are also shown to compare the effects of these various combinations of fiber failure models and thermal conditions (isothermal or adiabatic). In Figure 3.3-11a, the experimental out-of-plane displacement curve stops at approximately 0.15 ms due to a loss of paint required by the DIC. The isothermal and adiabatic simulations with no fiber failure predict nearly identical out-of-plane displacement time histories for the three points identified in Figure 3.3-10b. However, when fiber failure is included, the adiabatic simulations (for both maximum stress and Curtin model predictions) result in larger out of plane displacements than the simulations with no failure due to the thermal softening in the matrix. The isothermal maximum stress model predictions are very similar to the isothermal Curtin model predictions; the same is true for the adiabatic simulations.

It is evident from Figures 3.3-11a through 3.3-11c that the simulations with no fiber failure result in an overly stiff response, which is why the simulated and experimental time histories become out of phase after the first peak in the out of plane displacement versus time curves. Even in impact tests where projectile penetration does not occur, such as the

one simulated in this section, there is still significant matrix damage and fiber breakage, both visible and barely visible. It is hypothesized that this impact damage would reduce the effective wave speed of the material in damaged areas. This would imply the time it takes the initial stress wave (i.e., due to the projectile impact) to propagate from the center of the panel to the circular boundary in the experiment is less than the time it takes for the reflected stress wave to propagate from the circular boundary back to the center of the panel (since the reflected wave must traverse damaged areas with lower effective elastic properties and therefore lower effective wave speeds than undamaged areas). In the simulations with no fiber failure, the effective wave speeds of elements near the impact zone after the first impact are likely higher than they should be, which is likely why the simulated second peaks in out-of-plane displacement occur at earlier times than the experimental peaks. It is evident that the out-of-plane displacement time histories predicted by the models with fiber failure are more in-phase with the experimental results. However, in both the isothermal an adiabatic cases, the simulations with fiber failure overpredict the experimental out-of-plane displacements.

a)

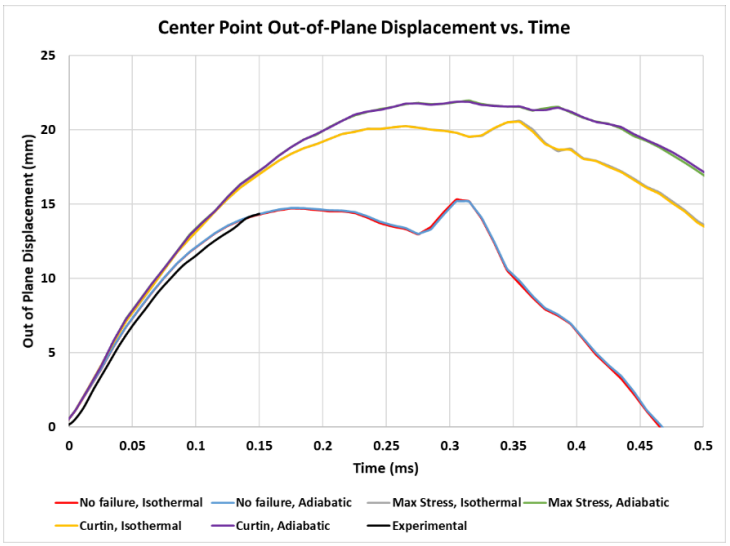

b)

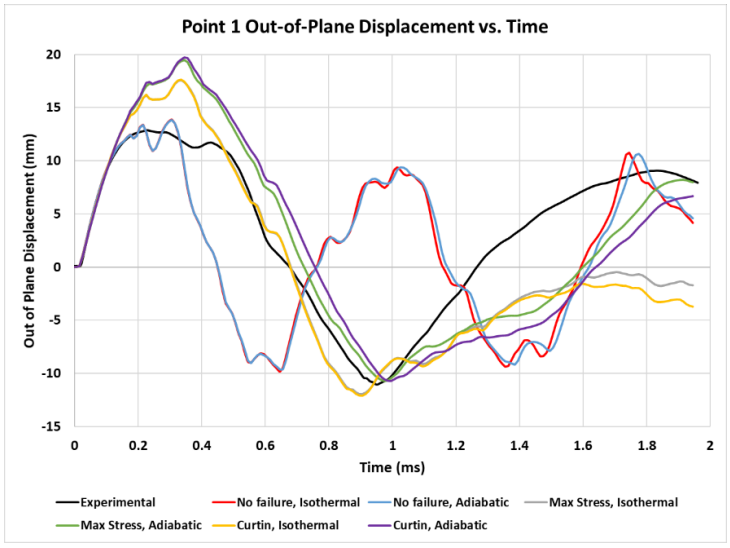

c)

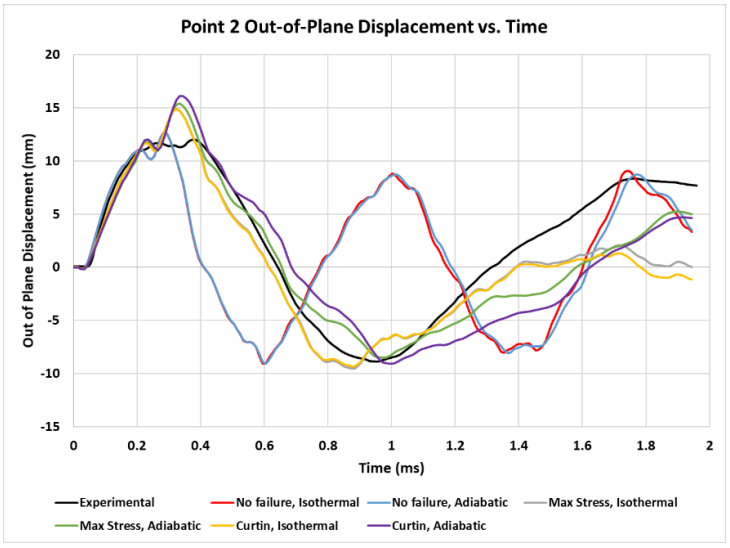

Figure 3.3-11: Simulated and Experimental Out-of-Plane Displacement Time Histories for a) Center Point; b) Point 1; c) Point 2

Figure 3.3-12 shows the experimental and simulated out-of-plane displacement contours on the back side of the panel (i.e., the side opposite of that impacted by projectile) 0.15 milliseconds after the aluminum projectile impacts the plate. The simulation results in Figure 3.3.12 correspond to the fully adiabatic simulation with no fiber failure. This case was chosen since it resulted in the closest correlation with the first peak in the out-of-plane displacement versus time curves shown in Figure 3.3-11. The white spaces on the experimental contour plots in Figure 3.3-11 are due to loss of the speckle pattern required by the DIC to compute the out-of-plane displacement.

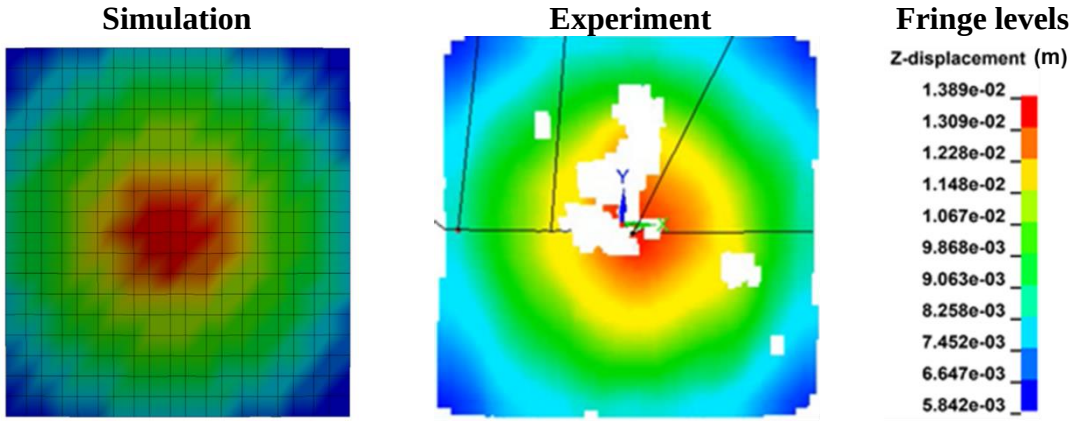

Figure 3.3-12: Simulated and Experimental Contours of Out-of-Plane Displacement at t=0.15 Milliseconds for Simulation 1; Z-Displacement is in Meters

Figures 3.3-13a through 3.3-13f show simulated contours of the maximum value of the microscale subcell absolute (Kelvin) temperature 0.15 milliseconds after impact for each of the six through thickness layers of thick shell elements for the fully adiabatic simulation with no fiber failure presented in Figure 3.3-11. Layer 1 designates the layer impacted by the projectile whereas layer 6 denotes the back of the plate. It is evident that the highest simulated temperature rises occur in the middle two layers, with the maximum temperature of 401.95 Kelvin (128.8°C) occurring in the 4th layer of thick shell elements.

It is also interesting to note that the simulation predicts higher temperature rises on the back layer than the layer the projectile comes into contact with. Note that no IR measurements of impact-induced temperature rises were available for T700/E862 impact tests.

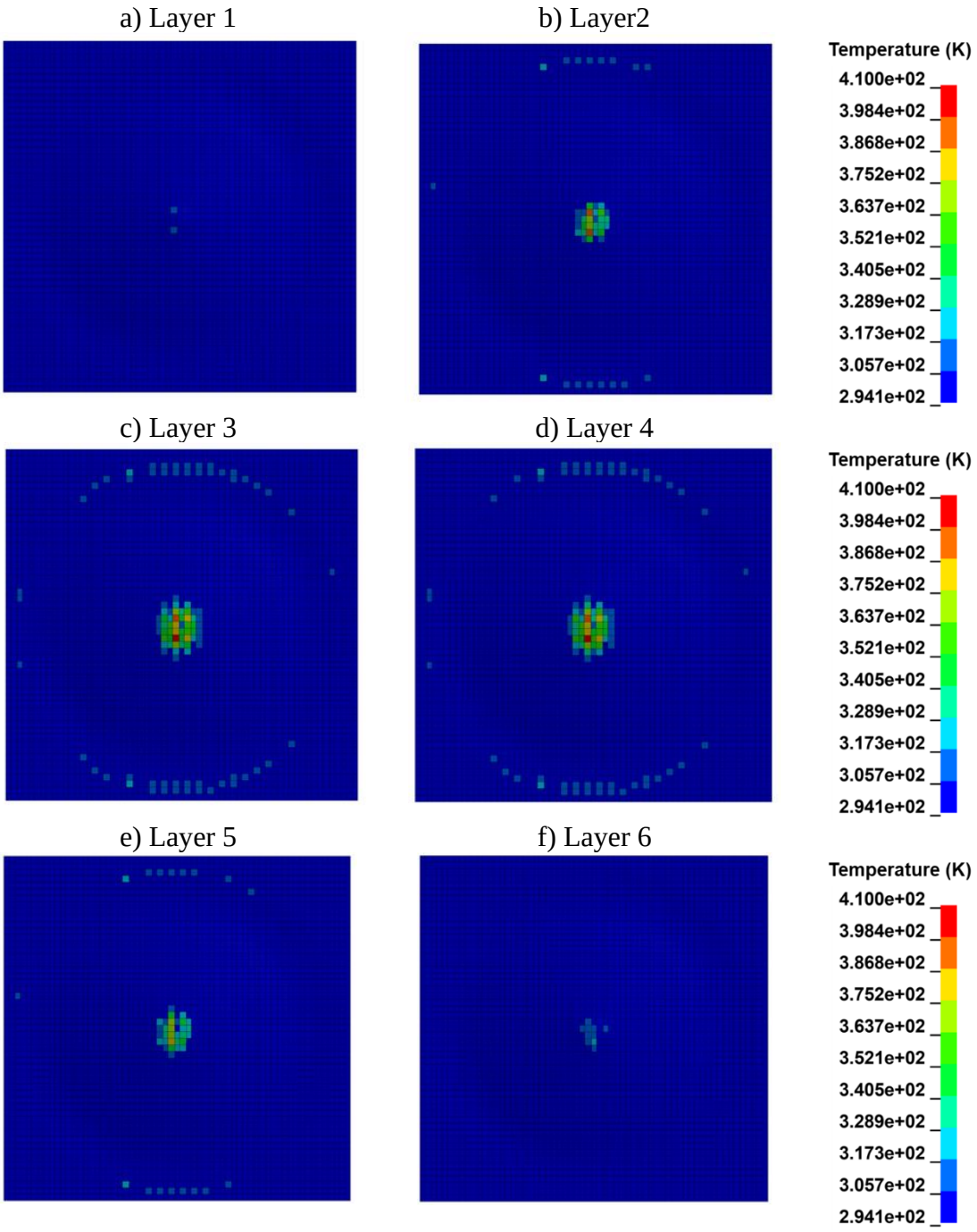

Figure 3.3-12: Contours of Maximum Subcell Temperature Rise on Each of the Six Through-Thickness Layers in the Fully Adiabatic Simulation with No Fiber Failure at t=0.15 Milliseconds; Layer One Designates the Layer Impacted by the Projectile Whereas Layer Six Denotes the Backside of the Plate

3.3.6 Conclusions

Details regarding the development of a UMAT designed to facilitate the analysis of PMCs with complex fiber architectures subjected to ballistic impact loading conditions, including effects of adiabatic heating due to high-rate inelastic deformation of the polymer matrix, have been presented. To preserve heterogeneity at the highest length scale in FE models, the UMAT was used in the context of a subcell-based approach (Littell, 2008; Blinzler, 2012; Cheng and Binienda, 2008; Li et al., 2009; Goldberg et al., 2012; Xiao et al., 2011; Cater et al., 2014; Cater et al., 2015), whereby the mesoscale RUC of the triaxial braid is discretized into unique subcell regions based on the braid architecture. Quasi-static straight-sided coupon tests conducted by Littell (2008) and Littell et al. (2008) and a flat panel impact test conducted by NASA personnel on a T700/E862 [0°/60°/–60°] triaxially braided composite material system were simulated using the synergistic multiscale framework. Simulations of straight-sided quasi-static axial tension tests were in excellent agreement with experimental data whereas simulations of straight-sided quasi-static transverse tensile coupon tests were unable to accurately capture the nonlinearity observed in the test. This is because the nonlinearity in the straight-sided transverse tensile coupon test was due to progressive matrix damage that initiated at the coupon free edges (Kohlman, 2012). However, matrix progressive damage has not been included in the current multiscale framework. To examine the effects of matrix adiabatic heating, an impact test conducted at NASA Glenn Research Center on a T700/E862 [0°/60°/–60°] triaxially braided composite panel was simulated. The impact simulation predicted local matrix temperature rises of over 105°C, though no measurements of impact-induced temperature rises were recorded in the experiment to compare this result with. Simulation results with no fiber failure indicate the

effects of adiabatic heating have no significant effect on the out of plane displacement versus time response of the panel. However, when fiber failure is considered, the impact simulation predicted additional out of plane displacement for adiabatic simulations compared to the isothermal case. While the results of the adiabatic simulations with fiber failure overpredict the first peak of the out of plane displacement versus time curves, the additional out of plane displacement predicted for the adiabatic case is consistent with the hypothesis that adiabatic heating does indeed play a role in the impact response of PMCs. It is expected that, once matrix progressive damage and failure are incorporated into the analysis, accounting for the effects of strain rate, temperature, pressure, and adiabatic heating will play a major role in accurately predicting the impact response of PMC structures.

MULTISCALE MODELING OF CREEP IN CERAMIC MATRIX COMPOSITES

4.1 Introduction

The ability of non-oxide CMCs with silicon carbide (SiC) matrices, and either Carbon (C) or silicon carbide (SiC) fibers (C/SiC and SiC/SiC CMCs), to perform exceptionally in extreme environments make them materials of choice in several high-temperature applications. This includes land- and air-based turbines (Spriet, 2014), advanced jet engine components, advanced rocket components, and other space applications (Staehler and Zawada, 2000; Naslain and Christin, 2003; Fohey et al., 1995; Spriet and Habarou, 1996; Brockmeyer, 1992). During service, CMCs are subjected to elevated temperatures (>1000℃), sustained loading, transients – either planned or accidental (Lara-Curzio, 1999), and gaseous oxidants for extended time periods. In such applications, CMC components are required to maintain structural integrity for thousands of hours or more (Naslain, 2004). Despite their intrinsic high strength, toughness, quasi-ductility, and ability to maintain structural integrity at elevated temperatures, SiC-fiber-based CMCs are known to creep at temperatures above about 1000-1100℃ (Gauthier and Lamon, 2009; Mital et al., 2018), which is the approximate maximum usage temperature for super alloys (Ohnabe et al., 1999). In composites, when one constituent creeps, it subsequently unloads to the other more creep-resistant constituents and can substantially alter the as-produced residual stresses in the composite (Santhosh et al., 2018).

Depending on the CMC, either the fibers (Begley et al., 1995; Santhosh and Ahmad, 2013) or the matrix (Rugg et al., 1999; Santhosh et al., 2018) may be more prone to creep. To categorize the creep behavior in CMCs, Holmes and Chermant (1993) defined the fiber-matrix creep mismatch ratio (CMR) as the ratio of the effective fiber creep strain rate to

the effective matrix creep strain rate: CMR=$\dot{\varepsilon}_f^I/\dot{\varepsilon}_m^I$. For CMR<1, $\dot{\varepsilon}_f^I < \dot{\varepsilon}_m^I$ and the matrix relaxes and unloads onto the more creep-resistant fibers, which can result in fiber failures (Rugg et al., 1999). For CMR>1, $\dot{\varepsilon}_m^I > \dot{\varepsilon}_f^I$ and the fibers relax and unload to the matrix. In this case (CMR>1), the time-dependent increase in matrix stress due to load transfer from the fibers can lead to progressive matrix cracking in high stiffness matrices, such as chemical vapor infiltrated (CVI) SiC. In an oxidizing environment, such as that experienced by turbine hot gas path components, matrix cracking creates pathways for gaseous oxidants to attack the CMC interior (Sullivan, 2016; Morscher et al., 2000; Xu et al., 2014; Lara-Curzio, 1999). It is therefore evident that creep in CMCs is a manifestation of simultaneous creep and relaxation in the constituents, even when the global mechanical loading on the composite is constant. Since high temperature CMCs typically consist of woven fabric architectures with tows woven in two perpendicular directions, this time-dependent constituent load transfer is inherently more complex. Further, the presence of multiple length scales in woven CMCs combined with the inability to produce neat ceramic samples representative of the highly porous in-situ CMC matrix presents significant modeling challenges. As a result, nonlinear constitutive laws describing creep and progressive damage in the constituents must be backed out based on coupon level test data. Moreover, it is generally unknown a-priori whether the fibers or matrix are more prone to creep. Thus, to facilitate the timely design and certification of next generation CMC material systems, physics based multiscale computational models able to admit three-dimensional stress states are necessary to investigate the time-dependent constituent load transfer responsible for their macroscopic creep deformation under sustained loading at elevated temperatures.

Macroscopic models, which treat the CMC as a smeared homogeneous continuum, have been proposed by several authors (Bessho et al., 2005; Gowayed et al., 2011). However, since macroscopic models do not explicitly model the constituents, they are incapable of simulating the complex constituent interaction and time-dependent load transfer responsible for macroscopic CMC creep. Since effective CMC constitutive behavior is a function of that of the constituents, their arrangement, and interactions, multiscale micromechanics-based approaches, which explicitly model the constituents, are more suitable for modeling CMC creep, particularly since creep may occur in both the fiber and matrix constituents. Holmes and Wu (1995), Rugg et al. (1999), and Almansour and Morscher (2019) developed one-dimensional uniaxial models to simulate the creep behavior of CMC single fiber microcomposites and single tow minicomposites; however, the one-dimensionality of the models precludes analyses of woven composites, where the tows experience multiaxial stress states. These one-dimensional models are also unsuitable for incorporation in micromechanics-based multiscale models, even for unidirectional fiber architectures, since these require fully three-dimensional material constitutive models. Santhosh and Ahmad (2013) and Santhosh et al. (2018) developed three-dimensional models for creep and damage in woven CMCs, where creep was solely modeled in one constituent. Pineda et al. (2015) used a three-dimensional temperature-dependent Norton-Bailey (Norton, 1929; Bailey, 1935) creep law as a constitutive model in the GMC (Aboudi et al., 2012) micromechancs framework to study the effect of stochastically varying creep model parameters on the creep behavior of a unidirectional SCS-6 SiC fiber-reinforced RBSN matrix composite lamina; creep was modeled in the fibers and matrix.

In this chapter, a three-dimensional temperature-dependent viscoplastic creep model is formulated based on the well-known Norton-Bailey/Nutting (Norton, 1929; Bailey, 1935; Nutting, 1921; Nutting, 1943) creep law with Arrhenius temperature dependence, Hill's (1948) orthotropic plastic potential, and an associative flow rule. Time hardening and strain hardening formulations of the model are considered to contrast these two widely used approaches. The three-dimensional time-hardening model is then used as a constitutive law in the GMC micromechanics framework (Aboudi et al., 2012) to simulate creep of SiC/SiC microcomposites for which data is available in the open literature (Rugg et al., 1999). The effects of time-dependent constituent load transfer, CMR, and fiber volume fraction are investigated and compared with the results presented in Rugg et al. (1999). Lastly, a computational study of the effects of creep-induced constituent stress redistribution on the room temperature proportional limit (first matrix cracking) stress level is presented, where an existing progressive damage law (Liu, 2011; Liu and Arnold, 2011; Liu, Chattopadhyay, and Arnold, 2011; Liu and Arnold, 2013) is utilized to simulate damage initiation and progression in the ceramic matrix.

4.2 Viscoplastic Creep Model Formulation

In this section, the formulation of a three-dimensional orthotropic viscoplastic creep constitutive model is presented. It is emphasized that this model is to be applied at the constituent level. While this study focuses on CMCs with SiC fiber reinforcement, which are generally considered mechanically pseudo-isotropic (Gowayed and Ojard, 2020), the model is formulated for the more general orthotropic case to facilitate modeling of carbon fibers, which are generally considered to be mechanically transversely isotropic (Daniel and Ishai, 2006) and are also a widely used CMC fiber reinforcement.

The general form of Hill's (1948) orthotropic quadratic plastic potential is expressed as:

$$f = \sqrt{\begin{matrix} F(\sigma_{22}-\sigma_{33})^2 + G(\sigma_{33}-\sigma_{11})^2 + H(\sigma_{11}-\sigma_{22})^2 \\ +2L\tau_{23}^2 + 2M\tau_{13}^2 + 2N\tau_{12}^2 \end{matrix}} \tag{4.2-1}$$

where, *F, G, H, L, M,* and *N* are coefficients that characterize the inelastic orthotropy of the material. It is noted that the Hill (1948) potential reduces to the isotropic von Mises potential when $F = G = H = \frac{1}{6}$ and $L = M = N = \frac{1}{2}$. An associative flow rule is utilized, where the components of the inelastic (creep) strain rate tensor, $\dot{\varepsilon}_{ij}^{cr}$, are assumed to be equal to the product of the rate of the plastic multiplier, $\dot{\lambda}$, and the partial derivative of the plastic potential with respect to the components of the Cauchy stress tensor, σ_{ij}, as follows:

$$\dot{\varepsilon}_{ij}^{cr} = \dot{\lambda}\frac{\partial f}{\partial \sigma_{ij}} \tag{4.2-2}$$

The effective stress, σ_e, is next defined as

$$\sigma_e = \sqrt{3}f \tag{4.2-3}$$

which, for an isotropic material, reduces to the applied stress for uniaxial tensile or uniaxial compressive loading. The rate of the plastic multiplier, $\dot{\lambda}$, is related to the effective inelastic strain rate, $\dot{\varepsilon}_e^{cr}$, by invoking the principle of equivalence of plastic power density:

$$\dot{W}^{cr} = \sigma_{ij}\dot{\varepsilon}_{ij}^{cr} = \sigma_e\dot{\varepsilon}_e^{cr} \geq 0 \tag{4.2-4}$$

which must be nonnegative due to thermodynamic requirements (Allen, 1991; Chow and Lu, 1989; Faria et al., 1998; Kawai et al., 2010; Laudau et al., 1960). By evaluating the partial derivative specified in Equation 4.2-2 and substituting Equations 4.2-2 and 4.2-3

into Equation 4.2-4, the relationship between the rate of the plastic multiplier and the effective inelastic strain rate is obtained as follows:

$$\dot{\lambda} = \sqrt{3}\dot{\varepsilon}_e^{cr} \tag{4.2-5}$$

The effective inelastic strain rate in this work is determined using the Norton-Bailey (Norton 1929, Bailey 1935), also known in the literature as the Nutting (1921, 1943), creep power law. The Norton-Bailey/Nutting creep power law was originally developed for constant uniaxial stress and constant temperature conditions and is given by:

$$\varepsilon_e^{cr} = A\sigma_e^n t^m exp\left(-\frac{Q}{kT}\right) = A\sigma_e^n t^m exp\left(-\frac{P}{T}\right) \tag{4.2-6}$$

where Q is the activation energy, k is Boltzmann's constant, T is the absolute (Kelvin) temperature, t is time, $P = \frac{Q}{k}$ and A, $n > 1$, and $m < 1$ are model parameters that may be taken as functions of temperature (Kraus, 1980; Penny and Marriott, 2012). As suggested by Dorn (1955), an Arrhenius term has been introduced in Equation 4.2-6 to explicitly capture the temperature dependence of the creep rate (Skrzypek and Hetnarski, 1993; Aboudi et al., 2012). Since the Norton-Bailey/Nutting creep law was originally developed for uniaxial stress states, the uniaxial stress and uniaxial creep strain have been replaced with the effective stress, σ_e, and effective creep strain, ε_e^{cr}, in Equation 4.2-6. The dimensions of the parameters A, n, and m in Equation 4.2-6 are such that the effective inelastic strain is dimensionless (units given in Table 4.3.1). For conditions of varying stress, such as experienced by the constituents in a composite under creep, it is desirable to work with the creep strain rate, which is determined by evaluating the partial derivative of Equation 4.2-6 with respect to time:

$$\dot{\varepsilon}_e^{cr} = A\sigma_e^n m t^{(m-1)} exp\left(-\frac{P}{T}\right) \tag{4.2-7}$$

Equation 4.2-7 is known as the time-hardening formulation. Note that, since the partial derivatives with respect to temperature and stress have been neglected in deriving Equation 4.2-7, it is technically limited to cases where the stress and temperature change slowly (Stouffer and Dame, 1996). However, this is likely not an issue for CMC creep modeling, where it can be reasonably assumed that components will experience slowly varying stresses and temperatures. It should be noted that, since m < 1, the creep strain rate given by Equation 4.2-7 is undefined when time is equal to zero; for this case, the integrated form of the time-hardening formulation (Equation 4.2-6) should be used to compute the initial creep strain increment (Stouffer and Dame, 1996; Kraus, 1980). To derive the strain-hardening formulation of Equation 4.2-7, where accumulated inelastic strain is used as a state variable instead of time, Equation 4.2-6 is solved for time and the resulting expression is substituted into Equation 4.2-7, yielding:

$$\dot{\varepsilon}_e^{cr} = A^{\left(\frac{1}{m}\right)} \sigma_e^{\left(\frac{n}{m}\right)} m (\varepsilon_e^{cr})^{\left(\frac{m-1}{m}\right)} exp\left(-\frac{P}{mT}\right) \tag{4.2-8}$$

In Equation 4.2-8, the effective inelastic strain rate depends on the accumulated effective creep strain, ε_e^{cr}, which is computed by integrating Equation 4.2-8. Note that, since the accumulated effective creep strain is initially zero, the integrated form of the time hardening formulation, Equation 4.2-6, should be used to compute the initial creep strain rate for the strain hardening formulation (Stouffer and Dame, 1996). By combining Equations 4.2-2, 4.2-5, 4.2-7, and 4.2-8, the inelastic strain rate tensor components for the

time and strain hardening formulations are determined (Kraus, 1980; Skrzypek and Hetnarski, 1993; Penny and Marriott, 2012) and are shown in Equations 4.2-9 and 4.2-10.

$$\dot{\varepsilon}_{ij}^{cr} = \sqrt{3}A\sigma_e^n m t^{(m-1)} exp\left(-\frac{P}{T}\right)\frac{\partial f}{\partial \sigma_{ij}} \tag{4.2-9}$$

$$\dot{\varepsilon}_{ij}^{cr} = \sqrt{3}A^{\left(\frac{1}{m}\right)}\sigma_e^{\left(\frac{n}{m}\right)} m(\varepsilon_e^{cr})^{\left(\frac{m-1}{m}\right)} exp\left(-\frac{P}{mT}\right)\frac{\partial f}{\partial \sigma_{ij}} \tag{4.2-10}$$

Since the Hill (1948) potential is independent of hydrostatic stress, $\dot{\varepsilon}_{kk}^{cr} = 0$ and the components of the inelastic strain rate tensor are equal to the components of the deviatoric inelastic strain rate tensor, $\dot{e}_{ij}^{cr} = \dot{\varepsilon}_{ij}^{cr} - \frac{1}{3}\dot{\varepsilon}_{kk}^{cr}\delta_{ij} = \dot{\varepsilon}_{ij}^{cr}$, implying the plastic deformation is isochoric. Since creep deformations are relatively small, infinitesimal deformation theory has been assumed to apply, which permits the additive decomposition of the total strain tensor into its respective elastic, inelastic (creep), and thermal components.

4.3 Micromechanical Creep Modeling Using the Generalized Method of Cells

To facilitate modeling of CMCs with arbitrary microstructures, the three-dimensional time hardening and strain hardening viscoplastic creep formulations (Equations 4.2-9 and 4.2-10) are used as inelastic constitutive models in the GMC micromechanics framework (Aboudi et al., 2012). The same microscale RUC used in Chapter 3 (Figure 3.2-1) is used and is therefore omitted from this section for brevity. The fiber volume fractions used in the simulations are mentioned as the results are presented and discussed in the next section.

4.4 Results and Discussion

In this section, simulation results of the previously described models are compared against experimental and numerical results from the literature (Rugg et al., 1999). Results are presented for CMC microcomposites consisting of single Hi-Nicalon fibers embedded

in a chemically vapor deposited (CVD) SiC matrix with various fiber volume fractions (Rugg et al., 1999). The constituent properties are shown in Table 4.3.1, where the creep properties have been adopted from Rugg et al. (1999). Since the model presented in Rugg et al. (1999) is one-dimensional and therefore does not include effects of Poisson's ratio, the creep model parameters have been slightly modified manually to obtain a reasonable fit with the experimental data (Rugg et al., 1999). In the results that follow, the matrix and fibers are modeled as elastically and inelastically isotropic (Pineda et al., 2015, Mital et al., 2018). Note that inelastic isotropy ($F = G = H = \frac{1}{6}$ and $L = M = N = \frac{1}{2}$) reduces the orthotropic Hill (1949) potential to the isotropic von Mises potential, $f = \sqrt{J_2}$, where $J_2 = \frac{1}{2} s_{ij} s_{ij}$. In the case of inelastic isotropy, $\frac{\partial f}{\partial \sigma_{ij}} = \frac{s_{ij}}{2\sqrt{J_2}}$. The fiber-matrix interphase is not explicitly modeled to facilitate comparison with the one-dimensional model presented in Rugg et al. (1999), which solely considered the fiber and matrix constituents.

Table 4.3.1. Fiber and Matrix Elastic and Creep (Rugg et. al., 1999) Properties

	A ($min^{-m} Pa^{-n}$)	m	n	P (K)	E (GPa)	ν
Matrix	2.33×10^{-17}	0.49	1.9	9607	420	0.20
Hi-Nicalon Fiber	1.29×10^{-7}	0.48	1.42	32042	200	0.35

4.4.1 Time Hardening and Strain Hardening Formulation Comparison

Before using the developed models to study the creep response of the Hi-Nicalon/CVD SiC microcomposites (Rugg et al., 1999), it is useful to compare the time hardening and strain hardening creep formulations (Equations 4.2-9 and 4.2-10). Figure 4.4-1 shows the simulated longitudinal creep strain versus time response of a) pure Hi-Nicalon fiber, b) pure SiC matrix, and c) Hi-Nicalon/CVD SiC microcomposite with a fiber volume fraction

of 0.5 subjected to three different global uniaxial loading cases using both the time hardening and strain hardening formulations. The temperature used in the simulations is 1300 ^{o}C. Two of the loading cases consist of constant uniaxial global stresses of 100 MPa and 200 MPa whereas the other load case consists of a constant global uniaxial stress of 100 MPa for $0 \leq t \leq 1000$ minutes, after which the global stress is abruptly increased from 100 MPa to 200 MPa over the time interval $1000 \leq t \leq 1001$ minutes, and is then held constant at 200 MPa for the remainder of the simulation. It is evident that the simulated creep strain versus time curves for the time and strain hardening formulations are identical for pure fiber (Figure 4.4-1a) and pure matrix (Figure 4.4-1b) under constant global uniaxial stresses. However, the results differ when a nonconstant global uniaxial stress is applied. In Figure 4.4-1a, for the nonconstant stress loading case on the pure Hi-Nicalon fiber, the time hardening and strain hardening model predictions are identical for $0 \leq t \leq 1000$ minutes. When the global stress is increased to 200 MPa, the responses differ. When the stress is changed to 200 MPa in the time hardening formulation, the strain versus time curve for the constant stress of 200 MPa is shifted vertically (normal to the time axis, see the solid gray arrow) to the end of the response. In contrast, when the stress is changed to 200 MPa in the strain hardening formulation, the curve for the constant stress of 200 MPa is shifted horizontally (normal to the strain axis, see the dashed black arrow) to the end of the response. The same trends are observed in Figures 4.4-1b for the pure SiC matrix.

It is evident from Figures 4.4-1a and 4.4-1b that, for a given constant stress level and temperature, the SiC matrix creeps more than the Hi-Nicalon fiber and is therefore less creep resistant (CMR<1). Therefore, when the composite is subjected to a constant global

longitudinal stress, the matrix unloads onto the fiber, leading to a decrease in matrix stress and an increase in the fiber stress in time, as will be shown later in the chapter. Because of the nonconstant stresses in the constituents when a composite begins to creep, the time and strain hardening formulations differ slightly under both constant and varying global stress conditions. Additionally, the shifting of the curves normal to the time and strain axes does not occur for the composite in the same way it does for a monolithic material when subjected to variable stress loading, as shown in Figure. 4.4-1c.

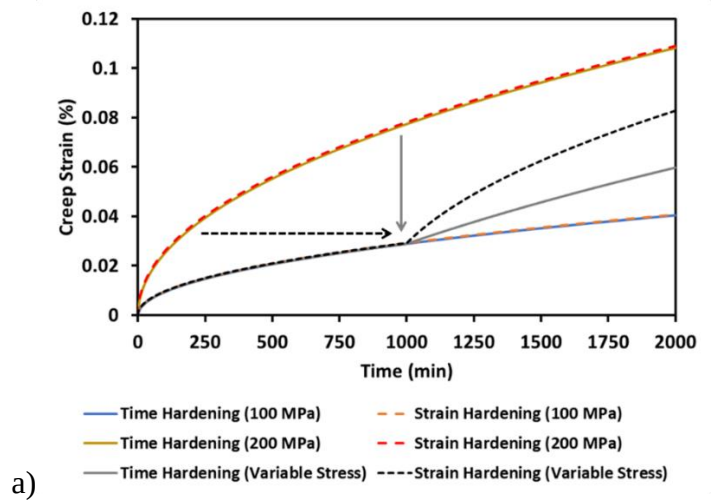

a)

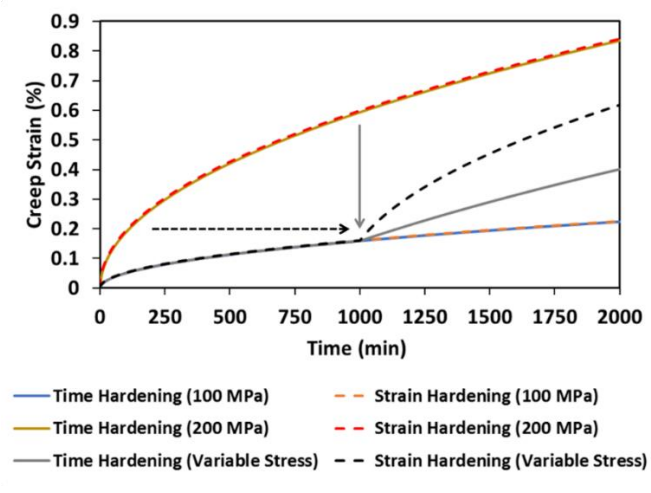

b)

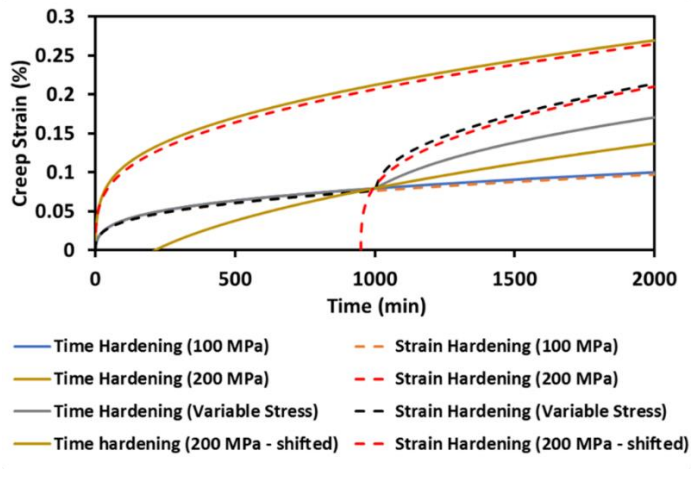

c)

Figure 4.4-1. Longitudinal Creep Strain Versus Time for a) Pure Hi-Nicalon Fiber; b) Pure SiC Matrix; c) Composite (V_f= 0.5) for Three Different Loading Cases

Though the time and strain hardening formulations provide identical results for a monolithic material under sustained loading, as shown in Figure 4.4-1, the time hardening formulation is more widely used in the literature due to its ease of implementation (Kraus, 1980). The main shortcoming of the time hardening formulation is that it is not objective with respect to time, as all physical laws should be (Stouffer and Dame, 1996). Despite this, it has been used successfully by many authors due to its simplicity and ease of implementation. Since both formulations produce very similar results for the composite, the time hardening formulation is used in the remainder of this chapter.

4.4.2 Time-Dependent CMC Deformation and Constituent Load Transfer

Figure 4.4-2 shows the simulated total strain versus time of a Hi-Nicalon/CVD SiC microcomposite with a 52% fiber volume fraction (Rugg et al., 1999) subjected to a constant RUC average longitudinal stress of 100 MPa at 1300 ^{o}C. The total composite strain is initially nonzero and purely elastic since there is no initial creep strain. The constituents subsequently start to creep under the applied stress, resulting in a strain versus time response that increases in time at a decreasing rate (i.e., primary creep) until reaching an approximate steady state around 500 minutes, after which the creep strain increases approximately linearly in time (i.e., secondary creep).

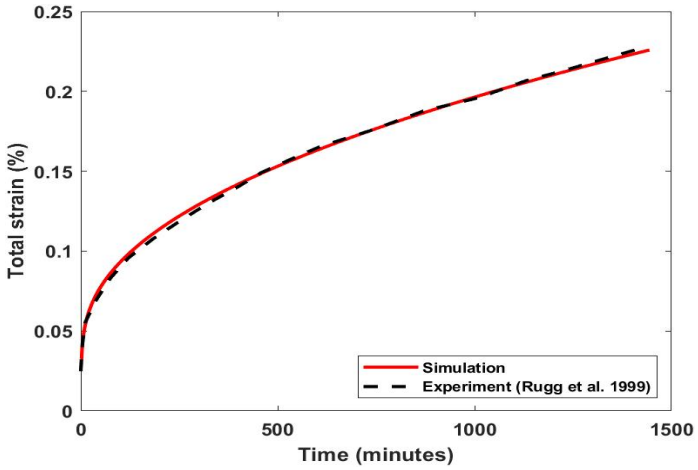

Figure. 4.4-2. Simulated and Experimental (Rugg et al. 1999) Total Strain Versus Time Response of 52% Fiber Volume Fraction Hi-Nicalon/CVD SiC Microcomposite Subjected to Sustained Loading of 100 MPa at 1300 ^{o}C

Figure 4.4-3 shows the simulated constituent longitudinal stress versus time results corresponding the total strain versus time results shown in Figure 4.4-2. The results agree favorably with the results of the one-dimensional model presented in Rugg et al. (1999), which are also shown in Figure 4.4-3. It is evident that the constituent longitudinal stresses are initially unequal due to the different elastic moduli of the Hi-Nicalon fibers (200 GPa) and the CVD SiC matrix (420 GPa). The larger matrix elastic modulus causes the initial matrix stress to be greater than that of the more compliant fiber. Due to the differing constituent creep rates, the matrix unloads onto the more creep resistant fiber, which implies a CMR<1 for the Hi-Nicalon/CVD SiC microcomposites (Rugg et al., 1999). As such, the fiber stress increases in time whereas the matrix stress decreases. The creep mismatch decreases until both constituents creep at approximately the same rate and an approximate steady state is reached. The fiber and matrix longitudinal stresses saturate at approximately 500 minutes, after which they remain at roughly constant values of 120 MPa and 78 MPa, respectively, for the remainder of the simulation. These values are in good agreement with one-dimensional model results from the literature (Rugg et al., 1999), for

which the fiber and matrix approximately saturate at longitudinal stress levels of 118 MPa and 80 MPa, respectively. The difference between the simulation results herein and the literature results (Rugg et al., 1999) can be attributed to the use of slightly different creep properties and the presence of Poisson's effects in the current work. The time at which approximate saturation of the constituent stresses occurs in Figure 4.4-3 corresponds to the time at which the total strain increases approximately linearly in time in Figure 4.4-2.

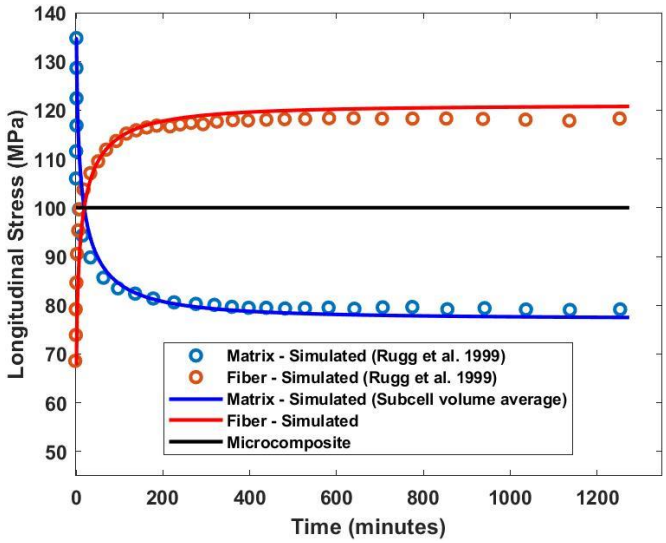

Figure 4.4-3. Simulated and Experimental (Rugg et al. 1999) Constituent Longitudinal Stress Time History of 52% Fiber Volume Fraction Hi-Nicalon/CVD SiC Microcomposite Subjected to Sustained Loading of 100 MPa at 1300 ^{o}C

4.4.3 Effects of Fiber-Matrix Creep Mismatch Ratio

Figure 4.4-4 shows the simulated CMR versus time for the Hi-Nicalon/CVD SiC microcomposite with 52% fiber volume fraction subjected to a constant global stress level of 100 MPa at 1300 ^{o}C. The results in Figure 4.4-4 correspond to the total strain versus time results in Figure 4.4-2 and the constituent longitudinal strain versus time results in Figure 4.4-3. Since there are three matrix subcells in the GMC RUC (see Figure 3.2-1), the matrix effective inelastic strain rate was volume averaged to compute the CMR shown in

Figure 4.4-4. It should be noted that the effective inelastic strain rates in the matrix subcells were almost equivalent for the duration of the simulation. It is evident that the time at which the CMR approximately reaches unity in Figure 4.4-4 (approximately 500 minutes) corresponds to the time in Figure 4.4-2 where the creep strain begins to increase approximately linearly in time (nearly constant inelastic strain rate; secondary creep) and the time in Figure 4.4-3 where the constituent stresses approximately saturate.

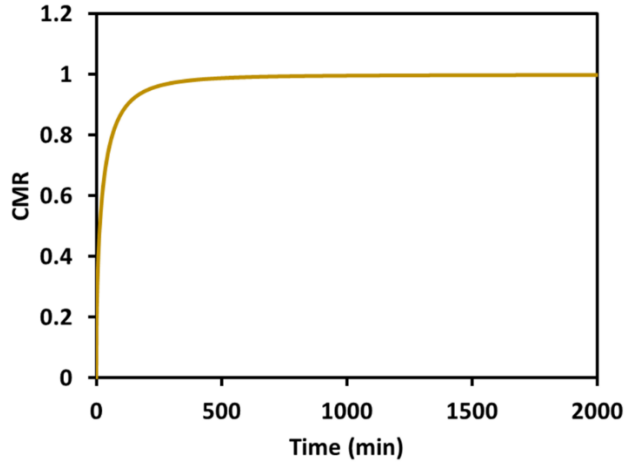

Figure 4.4-4: CMR Versus Time for a Hi-Nicalon/CVD Microcomposite with 52% Fiber Volume Fraction Subjected to a Constant Stress of 100 MPa at 1300 ^{o}C

4.4.4 Effects of Volume Fraction

Figure 4.4-5 illustrates the effects of the fiber volume fraction on the Hi-Nicalon microcomposite creep response. The total strain-time curves in Figure 4.4-5 with solid lines are the simulation results whereas the dashed lines are experimental results from Rugg et al. (1999). The constant global stress levels (130 MPa and 147 MPa), volume fractions (0.44 and 0.28), and temperature (1300 ^{o}C) used in the simulations are the same as those in the experiments (Rugg et al., 1999). A good agreement is observed between the simulation results and the experimental data (Rugg et al., 1999) in Figure 4.4-5a. Since the simulations presented in Figure 4.4-5a are conducted for different constant global

longitudinal stress levels, a general statement technically cannot be made regarding the effect of the fiber volume fraction on the microcomposite creep response. To allow a direct comparison, a simulation was conducted with a fiber volume fraction of 0.28 and a constant global stress level of 130 MPa and compared to results of the simulation with a volume fraction of 0.44 and a constant global stress level of 130 MPa (i.e., same stress level, different volume fraction); the results are shown in Figure 4.4-5b. It is evident from Figure 4.4-5b that, for a given global stress and temperature, the total strain increases as the fiber volume fraction decreases. It is emphasized that this is only the case for CMR<1, where the matrix creeps first and unloads onto the fiber. Moreover, comparing the results of the simulation with a fiber volume fraction of 0.28 and a constant global stress of 130 MPa in Figure 4.4-5b to the simulation with a fiber volume fraction of 0.28 and a constant global stress of 147 MPa in Figure 4.4-5a, it is evident that larger applied stress results in more longitudinal strain, as expected.

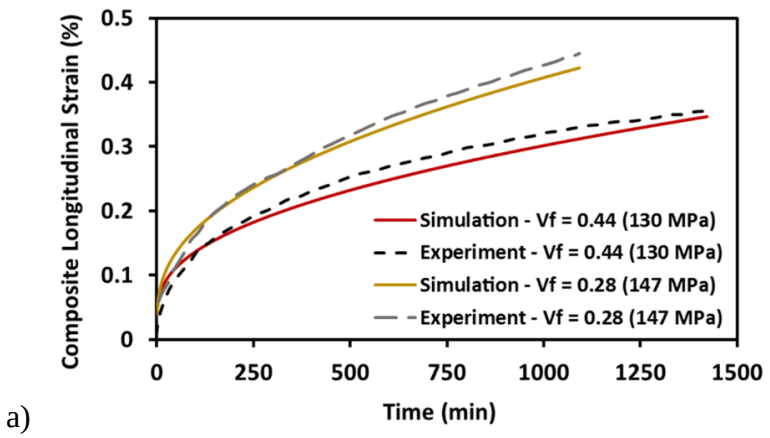

a)

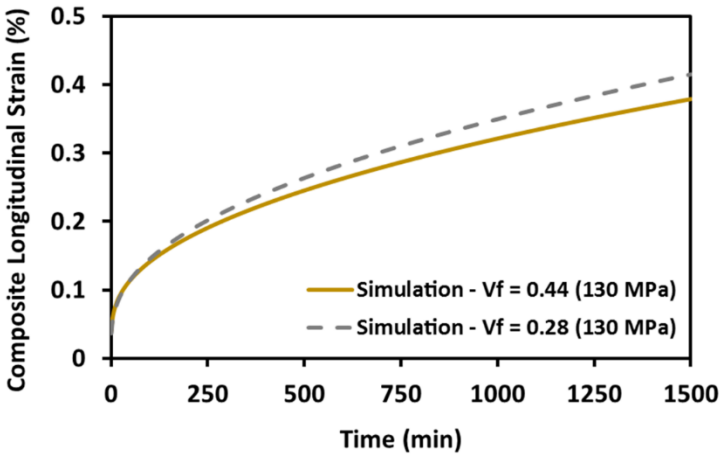

b)

Figure 4.4-5. Hi-Nicalon/CVD SiC Results: Effects of Different Fiber Volume Fractions Under (a) Different Constant Applied Longitudinal Stress; (b) Same Constant Applied Longitudinal Stress

In general, for a given constant stress level, temperature, and time, the creep strain increases when the volume fraction of the less creep resistant constituent increases. So, when CMR<1, as is the case for the Hi-Nicalon/CVD SiC microcomposites (Rugg et al., 1999), the creep strain increases with decreasing fiber volume fraction whereas the opposite is true for CMR>1. Figure 4.4-6 illustrates the effect of fiber volume fraction for the CMR>1 case and shows: a) simulated total strain-time history of a UD CMC with fiber and matrix properties (elastic and inelastic) equal to that of the Hi-Nicalon fiber, except for

the parameter A of the matrix, which is set equal one tenth of the value of that of the fiber to achieve CMR>1; b) the CMR versus time. The fiber volume fractions used for this comparison are 0.52 and 0.3. The temperature and constant global stress level used in the simulation are 1300 ^{o}C and 100 MPa. Figure 4.4-6a shows that, for a given constant global stress and temperature, the creep strain increases with increasing fiber volume fraction when CMR>1. Since $A_m = \frac{A_f}{10}$, where A_m and A_f refer to the A parameter (Table 4.3.1) of the matrix and fiber, respectively, the CMR (Figure 4.4-6b) is initially 10 and then gradually decreases to unity as an approximate steady state is reached (Figure 4.4-6a).

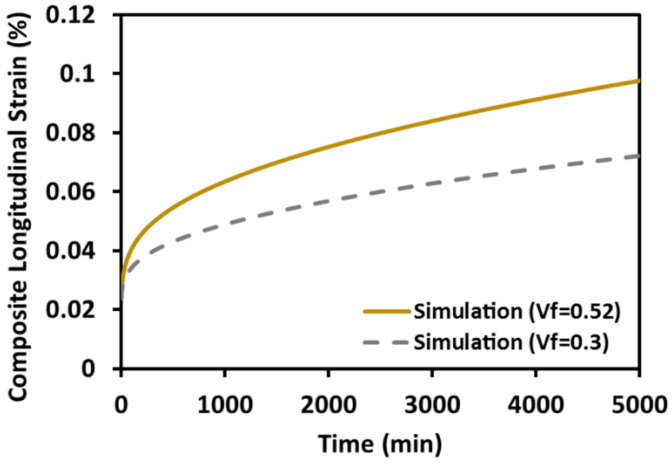

a)

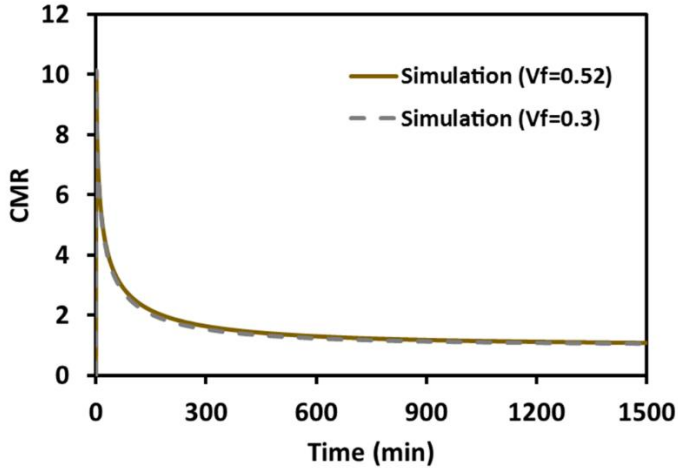

b)

Figure 4.4-6. a) Simulated Creep Versus Time Response of a Microcomposite with CMR>1; b) CMR Versus Time

4.4.5 Effects of Creep on Room Temperature Proportional Limit Stress Level

The purpose of this section is to computationally investigate the effects of elevated temperature creep on the post-creep room temperature proportional limit (first matrix cracking) stress level for the Hi-Nicalon/CVD SiC CMC microcomposites (Rugg et al., 1999) considered in the previous sections of this chapter. It is noted that, since post-creep room temperature quasi-static tensile tests were not considered by Rugg et al. (1999), solely computational results are presented in this section. While not considered in the results presented in previous sections of this chapter, it is necessary to employ a suitable progressive damage model. To this end, an existing bilinear isotropic progressive damage model (Liu and Arnold, 2011) is employed to simulate the initiation and propagation of matrix damage at the subcell level in the GMC micromechanics model (Aboudi et al., 2012) and is briefly described in the following paragraph prior to discussing the results.

The damage model (Liu and Arnold, 2011) consists of a scalar damage variable, ϕ, that reduces the initial elastic stiffness properties. The generalized Hooke's law with damage is as follows:

$$\sigma_{ij} = (1-\phi)C^0_{ijkl}\left(\varepsilon^{tot}_{kl} - \varepsilon^{th}_{kl} - \varepsilon^{cr}_{kl}\right) \tag{4.4-1}$$

where σ_{ij}, C^0_{ijkl}, ε^{tot}_{kl}, ε^{th}_{kl}, and ε^{cr}_{kl} are the respective components of the Cauchy stress, undamaged elastic stiffness, total strain, thermal strain, and inelastic (creep) strain tensors. The scalar damage variable, ϕ, ranges from an initial value of zero to unity, the former representing the initial undamaged material and the latter representing a complete loss of stiffness. The isotropic nature of the damage model implies the damaged ceramic matrix retains the elastic isotropy of the initial undamaged matrix. However, since the damage model is applied to the matrix constituent in the GMC micromechanics model (Aboudi et

al., 2012), the effective RUC elastic properties due to local matrix damage are not necessarily isotropic. The local undamaged and damaged elastic stiffness tensor components, C^0_{ijkl} and C_{ijkl}, are related according to: $C_{ijkl} = (1-\phi)C^0_{ijkl}$. Damage initiation and progression are controlled by the first invariants of the Cauchy stress and elastic strain tensors (Liu and Arnold, 2011), i.e., the hydrostatic stress, σ_{kk}, and hydrostatic elastic strain, $\varepsilon^{el}_{kk} = \varepsilon^{tot}_{kk} - \varepsilon^{th}_{kk} - \varepsilon^{cr}_{kk}$. Damage initiates when the hydrostatic stress exceeds a critical nonnegative value, σ_{crit}. The nonnegativity of σ_{crit} implies that damage can only initiate and accumulate for stress states with a tensile hydrostatic component. When the hydrostatic stress in any of the matrix subcells exceeds the critical value, $\sigma_{kk} > \sigma_{crit}$, the satisfaction of the following incremental damage law governs the subsequent propagation of damage:

$$f = 3nK^0\Delta\varepsilon^{el}_{kk} - \Delta\sigma_{kk} = 0 \tag{4.4-2}$$

where K^0 is the initial (undamaged) bulk modulus and n is the damage normalized secant bulk modulus (Liu and Arnold, 2011; Borkowski and Chattopadhyay, 2015). In Equation 4.4-2, $\Delta\sigma_{kk}$ and $\Delta\varepsilon^{el}_{kk}$ denote hydrostatic stress and hydrostatic elastic strain increments, which relate values at the next (i+1) and current (i) increments as: $\sigma^{i+1}_{kk} = \sigma^{i}_{kk} + \Delta\sigma_{kk}$ and $\varepsilon^{el,i+1}_{kk} = \varepsilon^{el,i}_{kk} + \Delta\varepsilon^{el}_{kk}$. An expression for the damage variable at the next increment, ϕ^{i+1}, is obtained by considering the hydrostatic component of the constitutive law, $\sigma_{kk} = 3K\varepsilon^{el}_{kk}$, where $K = (1-\phi)K^0$ is the damaged bulk modulus, in incremental form:

$$\Delta\sigma_{kk} = 3K\Delta\varepsilon^{el}_{kk} + 3\Delta K\varepsilon^{el}_{kk} = 3(1-\phi)K^0\Delta\varepsilon^{el}_{kk} + 3(1-\phi)K^0\varepsilon^{el}_{kk} \tag{4.4-3}$$

Substituting the expression for $\Delta\sigma_{kk}$ given by Equation 4.4-3 into Equation 4.4-2 and simplifying results in the following expression for the damage variable at the next increment:

$$\phi^{i+1} = \left(1 - \frac{n\Delta\varepsilon_{kk}^{el(i+1)} + (1-\phi^i)\varepsilon_H^{el(i+1)}}{(\Delta\varepsilon_H^{el(i+1)} + \varepsilon_H^{el(i+1)})}\right) \tag{4.4-4}$$

where the relations $K^{i+1} = \left(1-\phi^{i+1}\right)K^0$ and $K^i = \left(1-\phi^i\right)K^0$ have been used to obtain Equation 4.4-4. It is noted that, when implementing the damage update given by Equation 4.4-4, it is necessary to prevent negative values of ϕ^{i+1}, damage accumulation during unloading, and the values of damage from decreasing, the latter of which requires $\phi^{i+1} \geq \phi^i$. This can be accomplished in a numerical implementation by: i) setting ϕ^{i+1} to zero if Equation 4.4-4 results in a negative value; ii) setting $\phi^{i+1} = \phi^i$ if $\phi^{i+1} < \phi^i$.

To investigate the effects of time-dependent constituent load transfer on the RT proportional limit, simulations of CMC creep at various constant stress levels (50 MPa, 150 MPa, 220 MPa) followed by quasi-static monotonic tensile loading are presented and discussed in the remainder of this section. Specifically, the simulated thermomechanical loading consists of: i) two-hour stress-free thermal cooldown from an assumed processing temperature of 1450 °C to RT (25 °C) followed by a one-hour stress-free reheating to 1300 °C; ii) subsequent application of monotonic longitudinal tensile loading over 15 minutes to a given creep stress level; iii) roughly 19 hours (1120 minutes) of sustained creep loading; iv) monotonic unloading from the creep stress level to zero stress over 15 minutes; v) stress-free cooldown from 1300 °C to RT (25 °C); vi) monotonic quasi-static tensile loading. The simulation results to follow are for a Hi-Nicalon/CVD SiC microcomposite

with a 52% fiber volume fraction. The constituent coefficients of thermal expansion and matrix damage parameters used in the simulations are given in Table 4.4.2.

Table 4.4.2: CMC Thermal Properties (Rugg, 1997) and Damage Parameters (Liu and Arnold, 2011)

	CTE ($°C^{-1}$)	n	σ_{crit} (MPa)
SiC Matrix	$4.7x10^{-6}$	0.04	180
Hi-Nicalon Fiber	$4.8x10^{-6}$	N/A	N/A

The damage parameters in Table 4.4.2 were obtained from Liu and Arnold (2011) whereas the CTEs were obtained from Rugg (1997). Note that Rugg (1997) states that the CTE for Hi-Nicalon for temperatures between 20 °C and 900 °C is $4.6x10^{-6}$ $°C^{-1}$, though also mentions that values up to $5.3x10^{-6}$ $°C^{-1}$ have been measured. Rugg (1997) also states that little to no thermal residual stress would be expected in the matrix of Hi-Nicalon based microcomposites. Given that the majority of the Hi-Nicalon CTE values between $4.6x10^{-6}$ $°C^{-1}$ and $5.3x10^{-6}$ $°C^{-1}$ are above the SiC matrix CTE of $4.7x10^{-6}$ $°C^{-1}$ (Rugg, 1997), a CTE of $4.8x10^{-6}$ $°C^{-1}$ was utilized for Hi-Nicalon.

Figures 4.4-7 and 4.4-8 show the constituent longitudinal (Figure 4.4-7) and hydrostatic (Figure 4.4-8) stresses versus time for the aforementioned simulated thermomechanical loading. The prescribed RUC effective longitudinal stress and temperature history are also shown, the latter of which is plotted on the right y-axes. The subfigures (a, b, and c) in Figures 4.4-7 and 4.4-8 correspond to sustained (from 195 minutes to 1315 minutes) longitudinal creep stress levels of 50 MPa, 150 MPa, and 220 MPa, respectively. Other than the creep stress level, the prescribed loading in each case is identical. It is noted that the matrix progressive damage model and the viscoplastic creep model are employed for the entire duration of these simulations, i.e., the damage and creep models are not selectively turned on/off for various portions of the prescribed loading.

During the initial thermal cooldown from the stress-free processing temperature of 1450 °C to RT (0 to 120 minutes), the constituent CTE mismatch results in tensile stresses (longitudinal and hydrostatic) in the fiber and compressive stresses (longitudinal and hydrostatic) in the matrix. This is because the fiber CTE is greater than that of the matrix. For a given decrease in temperature, the fiber, if unconstrained by the surrounding matrix, would exhibit a larger magnitude thermal contraction than the matrix. However, in the composite, the matrix constrains the thermal contraction of the fiber, resulting in longitudinal and hydrostatic tension in the fiber and compression in the matrix. The magnitudes of the constituent hydrostatic thermal residual stresses (Figure 4.4-7) are larger than those in the longitudinal direction (Figure 4.4-8) because, though not shown, the transverse residual stresses are of the same sign as those in longitudinal direction for a given constituent (tensile for fiber and compressive for matrix). Since the simulated creep test temperature (1300 °C) is less than the stress-free processing temperature (1450 °C), the constituents retain a portion of the thermal residual stress due to the initial cooldown prior to the application of monotonic uniaxial tensile loading to the creep stress level, which occurs from 180 to 195 minutes.

Once the creep stress level is reached at 195 minutes, it is sustained until 1315 minutes. Similar to the results in the previous sections of this chapter, the matrix longitudinal stresses are larger than those of the fiber at the beginning of the creep loading (195 minutes) since the elastic modulus of the matrix (420 GPa) is greater than that of the fiber (200 GPa). This is true for the longitudinal stresses (Figure 4.4-7) for all creep stress levels considered (50 MPa, 150 MPa, and 220 MPa), though not as apparent for the 220 MPa case. In Figure 4.4-8, it is evident that the progressive application 220 MPa longitudinal stress on the

composite causes the local matrix hydrostatic stress to exceed the critical damage initiation stress (Table 4.4.2) of 180 MPa, which results in degradation of the effective matrix (matrix subcell volume average) elastic modulus from 420 GPa to approximately 204 GPa at the beginning of the creep loading (195 minutes). It is noted that matrix damage also occurs during loading to the creep stress level in the 150 MPa case, as is evident in Figure 4.4-8, though the resulting matrix damage is nominal in this case. No matrix damage occurred upon loading to the creep stress level in the 50 MPa case (Figures 4.4-7a and 4.4-8a). Since the CMR<1, the matrix unloads onto the more creep resistant fiber during the sustained creep loading (195 to 1315 minutes) for all creep stress levels considered. As such, no matrix damage occurs during creep in any of the simulations (i.e., since the matrix is unloading). Comparing the 50 MPa (Figures 4.4-7a and 4.4-8a) and 150 MPa (Figures 4.4-7b and 4.4-8b) load cases, it is evident that the larger applied creep stress level causes the local stresses to redistribute more quickly and results in a larger disparity in the approximate saturation stress levels of the constituents.

At the conclusion of the sustained creep loading (1315 minutes), the global longitudinal creep stress is reduced to zero over 15 minutes (from 1315 to 1330 minutes) while the creep temperature (1300 °C) is maintained. Comparing the constituent stresses at 180 minutes (after heating to the creep test temperature and before application of the creep stress) and 1330 minutes (before cooldown from creep test temperature and after removal of creep load), it is evident that creep alters the constituent residual stresses by the relative change in stress experienced by the constituent during creep. The time-dependent matrix stress relaxation during creep therefore results in (additional) compressive stresses in the matrix upon removal of the mechanical load (1330 minutes). As such, the matrix

residual compressive stresses at 1330 minutes are larger in magnitude than the compressive thermal residual stresses at 180 minutes. Since CMR<1, the time-dependent increase in fiber stress due to stress transfer from the matrix during creep results in (additional) tensile stresses in the fiber. The fiber tensile residual stresses at 1330 minutes are therefore larger in magnitude than the tensile thermal residual stresses. It is noted that the opposite behavior would be expected for CMR>1, where the fiber unloads onto the matrix. In this case (CMR>1), creep would result in the development of compressive stresses in the fiber and tensile stresses in the matrix. Once mechanical unloading is complete (at 1330 minutes), cooldown from the creep temperature to RT is applied from 1330 to 1440 minutes, which results in additional residual tension in the fiber and compression in the matrix since the CTE of the fiber is greater than that of the matrix. The opposite behavior would occur if the CTE of the matrix was greater than that of the fiber.

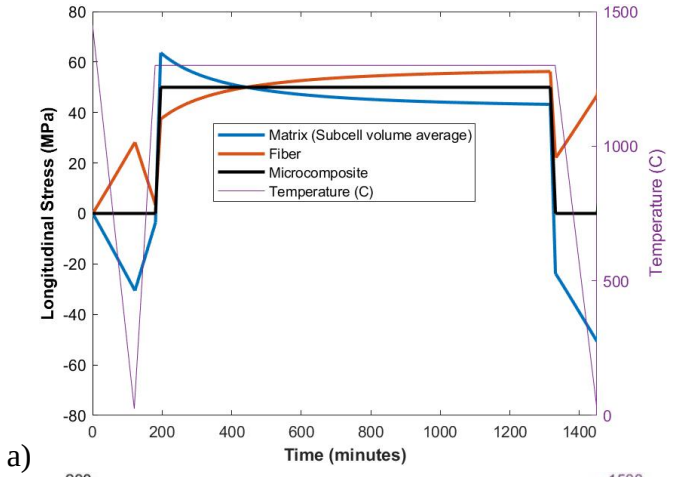

a)

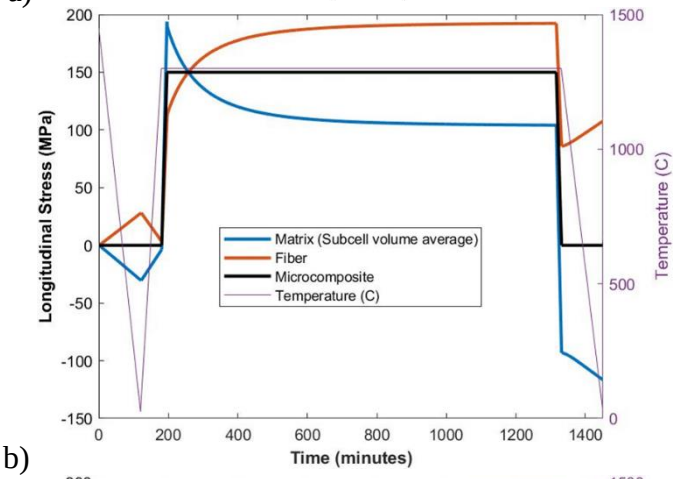

b)

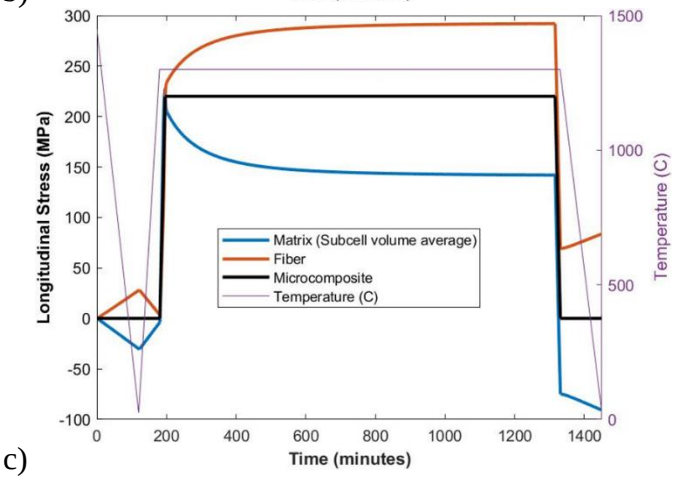

c)

Figure 4.4-7: Constituent Longitudinal Stresses for Hi-Nicalon/CVD SiC Microcomposite with 52% Fiber Volume Fraction Subjected to Simulated Thermomechanical Loading for Longitudinal Creep Stress Levels of a) 50 MPa; b) 150 MPa; c) 220 MPa

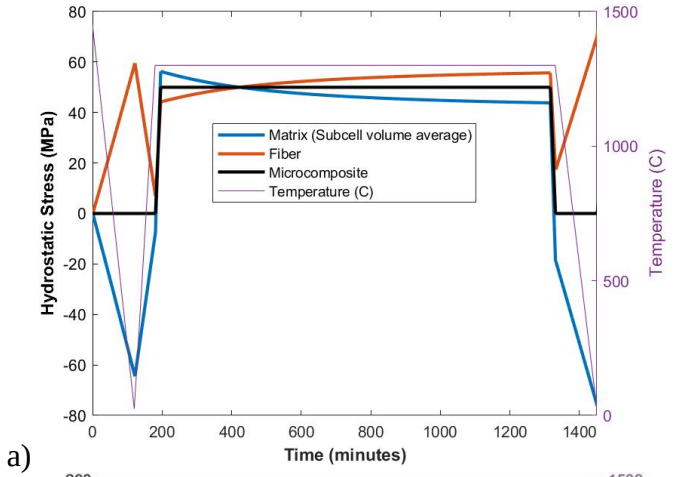

a)

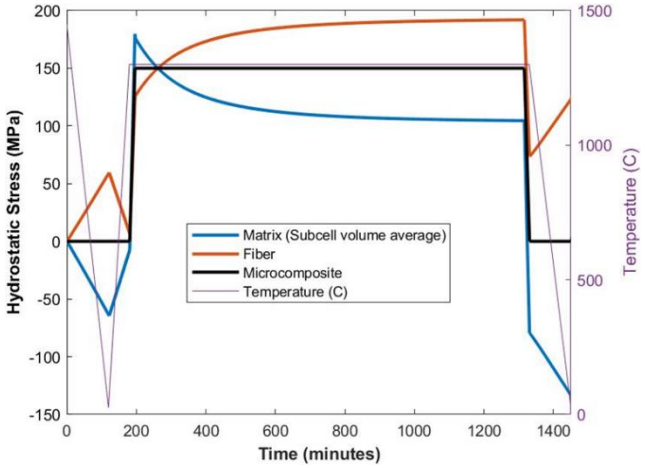

b)

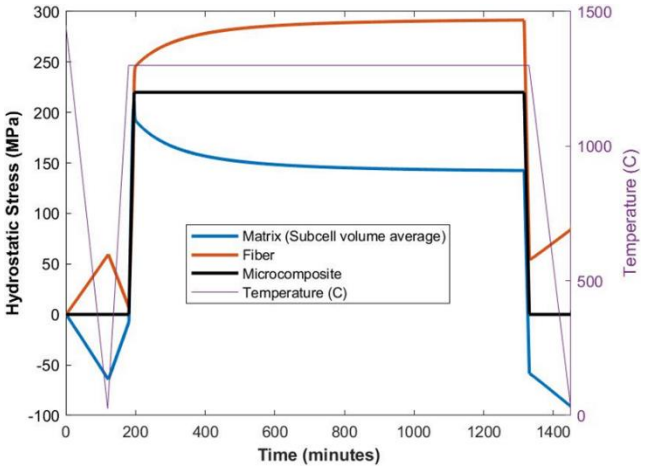

c)

Figure 4.4-8: Constituent Hydrostatic Stresses for Hi-Nicalon/CVD SiC Microcomposite with 52% Fiber Volume Fraction Subjected to Simulated Thermomechanical Loading for Longitudinal Creep Stress Levels of a) 50 MPa; b) 150 MPa; c) 220 MPa

Figure 4.4-9 shows simulated RT quasi-static monotonic tensile stress-strain curves for composites subjected to the previously-described simulated thermomechanical loading

conditions. The stress levels in the legend of Figure 4.4-9 refer to the sustained stress levels applied to the composite in the creep portion of the simulations prior to RT monotonic tensile loading. Also included in Figure 4.4-9 are stress-strain curves for composites that were: i) not subjected to the thermomechanical loading (denoted by "No residual" in the legend); ii) subjected solely to thermal cooldown from 1450 °C to RT prior to monotonic tensile loading (denoted by "As-produced" in the legend).

The proportional limit stress for each case shown in Figure 4.4-9 can be identified as the level of stress corresponding to the point at which the stress-strain curve deviates appreciably from linearity. For the composite with no residual stresses (blue curve), the RT proportional limit is approximately 140 MPa. It is evident that the simulated proportional limit for the composites that include the effects of residual stresses are all greater than that of the composite with no residual stresses. This is because the simulated thermomechanical loading results in compressive hydrostatic residual stresses in the matrix for the composites (CMR<1 and fiber CTE greater than matrix CTE) and loading cases considered in this section. Since matrix damage initiation and progression requires a local matrix hydrostatic tensile stress greater than the critical damage initiation stress (Table 4.4.2), any residual hydrostatic compression in the matrix must be overcome prior to damage initiation, thereby increasing the RT composite proportional limit. The amount by which the RT proportional limit increases is dependent on the magnitude of residual compression in the matrix; larger residual compressive stresses tend to increase the composite RT proportional limit stress by a greater amount. It is noted that the initial elastic modulus of the stress-strain curve (green curve) corresponding to the thermomechanical loading with the 220 MPa creep stress level (Figures 4.4-7c and 4.4-8c) is less than that of the other curves since significant

matrix damage occurred in the simulation while monotonically loading to the creep stress level, as was previously mentioned. It is also interesting to note that, while the proportional limit stresses of the composites subjected to simulated creep loading prior to monotonic tension increase with increasing creep stress level, the composite subjected to the 220 MPa creep load resulted in a compressive residual stress between that of the 50 MPa and the 150 MPa creep load cases. Despite this, the lower matrix modulus due to the progressive matrix damage that occurred during loading to the 220 MPa creep stress level still resulted in a larger proportional limit than the composite subjected to the 150 MPa creep stress level.

While fiber failure was not explicitly included in the simulations presented in this Chapter, the stress-strain curves in Figure 4.4-9 are shown up to the point at which the fiber stress reached an assumed strength of 900 MPa. While the actual strength of Hi-Nicalon fibers is 2.8 GPa (Gowayed and Ojard, 2020), the value of 900 MPa was selected, somewhat arbitrarily, to gain insight into the effect of creep-induced constituent residual stresses on the strain to failure as a post-processing step. It is evident in Figure 4.4-9 that the composite with no thermal residual stresses (blue curve), which has the lowest proportional limit stress of the cases considered, has the highest strain to failure. Other than the 220 MPa stress-strain curve in Figure 4.4-9, the simulated composite strain to failure decreases with increasing creep stress level. This is because the creep-induced stress transfer from the matrix to the fiber for the UD CMC considered herein (CMR<1) results in residual longitudinal tension in the fibers prior to the application of the monotonic tensile loading. As such, less composite longitudinal strain is required for the tensile prestressed fibers to reach the assumed fiber strength of 900 MPa. For all cases shown in Figure 4.4-9 other than the 220 MPa case, the increase in the proportional limit stress with increasing

creep stress level is accompanied by a reduction of the strain to failure (for CMR<1). In the 220 MPa case, the matrix damage that occurred during the simulated loading to the creep stress level prior to the simulated monotonic tensile loading results in the strain to failure being between that of the 50 MPa and 150 MPa cases. It is noted that, for CMCs with CMR>1, it is expected that, in the absence of matrix damage prior to simulated monotonic tensile loading, the RT proportional limit stress level would decrease and the strain to failure would increase after being subjected to elevated temperature creep with increasing constant stress levels.

The reduction of the strain to failure associated with the increase in the RT proportional limit stress for the CMCs with CMR<1 considered in this section are consistent with results reported by Pineda et al. (2015) for a UD CMC for which the fibers are more creep resistant than the matrix and therefore CMR<1. The increase in proportional limit in CMCs previously subjected to creep at increasing constant creep stress levels observed in the simulations presented in this section is also consistent with results reported by Santhosh et al. (2018) for a Sylramic-iBN/MI-SiC cross-ply CMC with CMR<1.

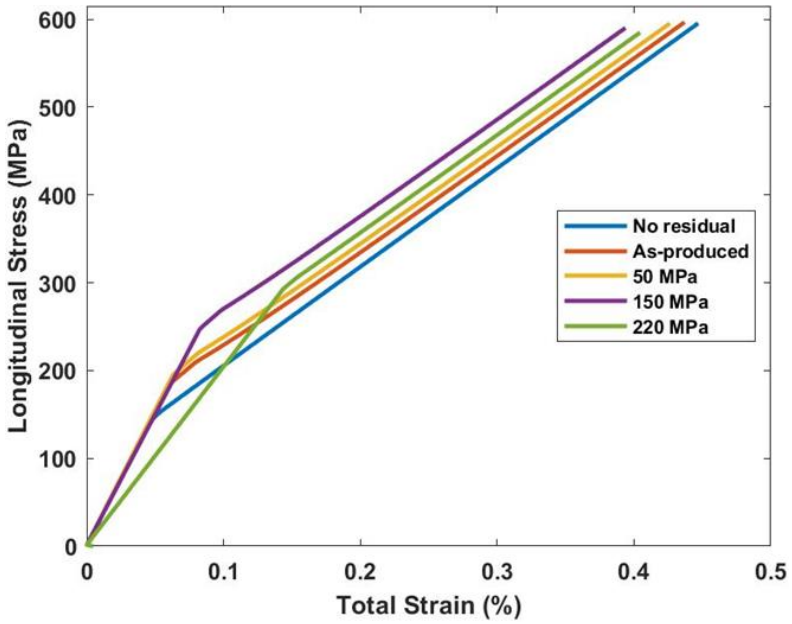

Figure 4.4-9: Simulated Room Temperature Quasi-Static Monotonic Tensile Stress-Strain Curves for UD CMCs Previously Subjected to Thermomechanical Loading

4.5 Conclusions

In this chapter, the formulation of a three-dimensional viscoplastic creep constitutive model based on the Hill (1948) orthotropic plastic potential, an associative flow rule, and the Norton-Bailey/Nutting creep law with Arrhenius temperature dependence was presented. Time hardening and strain hardening formulations were implemented and discussed. The three-dimensional viscoplasticity model was implemented into the GMC micromechanics theory, which was subsequently used to investigate the effects of time-dependent constituent load transfer, CMR, and fiber volume fraction on the creep response of Hi-Nicalon/CVD SiC CMC microcomposites for which experimental data was available in the open literature (Rugg et al., 1999). Though the constituent materials were both modeled as elastically and inelastically isotropic, the formulation is sufficiently general to describe orthotropic constitutive behavior. It is therefore applicable to CMC systems with orthotropic constituents, such as carbon-fiber reinforced CMCs. Results indicate that, when

a composite experiences creep, internal stress transfer is driven by the CMR, which is dependent on the mismatch in constituent elastic and creep properties. The rate of change of constituent stresses decreases in time as the CMR approaches unity an approximate steady state (secondary creep) is reached. When CMR>1, the fibers unload onto the matrix for whereas the matrix unloads onto the fibers for CMR<1. In general, for a given stress and temperature, more creep deformation is observed with increasing volume fraction of the less creep resistant constituent. So, when CMR<1, the creep strain increases with decreasing fiber volume fraction. For CMR>1, the creep strain increases with increasing fiber volume fraction. Both cases are possible in CMCs, though CMR<1 for the Hi-Nicalon/CVD SiC microcomposites (Rugg et al., 1999) considered in this chapter. Lastly, a computational study of the effects of creep-induced constituent stress redistribution on the room temperature proportional limit (first matrix cracking) stress level was also presented, where an existing bilinear progressive damage law (Liu and Arnold, 2011) was utilized to simulate the initiation and progression of damage in the ceramic matrix. Results of this computational study indicated an increase in the RT proportional limit due to creep-induced constituent stress redistribution when CMR<1, which is consistent with results reported by Santhosh et al. (2018) for a cross-ply CMC with CMR<1. Overall, simulation results are in good agreement with experimental and numerical results available in the literature and provide valuable insight into the mechanisms governing creep in CMCs.

5 CONTRIBUTIONS AND FUTURE WORK

5.1 Contributions

The primary objective of the research presented in this dissertation was to develop relevant multiscale computational tools and nonlinear constituent material constitutive models to better understand the complex multiscale behavior of fiber-reinforced composite materials. In particular, these models were used to gain insight into the nonintuitive mechanisms governing macroscopic PMC and CMC response in extreme service environments, including the high strain rate and impact behavior of PMCs (Chapters 2 and 3) and the elevated-temperature creep behavior of CMCs (Chapter 4).

In Chapter 2, a nonisothermal and thermodynamically consistent extension of the rate- and pressure-dependent Goldberg (Goldberg et al., 2005) unified viscoplastic polymer constitutive formulation was presented. In Chapter 3, the polymer viscoplasticity formulation developed in Chapter 2 was used as a constitutive model in the GMC micromechanics framework to computationally investigate the effects of adiabatic heating due to the conversion of plastic work to heat on the deformation of a T700/E862 UD composite. Significant adiabatic heating and thermal softening was observed for simulated matrix-dominated deformation modes. The GMC micromechanics model, including the nonisothermal polymer viscoplasticity model, was subsequently implemented as an LS-DYNA UMAT and used in the context of a subcell-based approach to approximate the heterogeneity of the braid architecture of a triaxially braided T700/E862 PMC to simulate quasi-static tensile tests (Littell, 2008) and a flat-panel impact test. Impact simulations predicted additional out of plane displacement for adiabatic simulations when fiber failure was considered. While the results of the adiabatic impact simulations with fiber failure

overpredicted experimentally observed out of plane displacements, it is consistent with experimental evidence (Johnston et al., 2018) that adiabatic heating does indeed play a role in the impact response of PMCs. While not considered in this work, it is expected that the consideration of matrix progressive damage and failure, in addition to local matrix adiabatic heating considered in this work, will play a major role in accurately predicting the impact response of PMC structures.

In Chapter 4, the formulation of a three-dimensional viscoplastic creep constitutive model based on Hill's orthotropic plastic potential, an associative flow rule, and the Norton-Bailey/Nutting creep law with Arrhenius temperature dependence was presented. Both time hardening and strain hardening formulations were implemented and discussed. The three-dimensional viscoplastic creep formulation was subsequently used as a constitutive model in the GMC micromechanics framework, where it was used to model creep in both the fiber and matrix constituents. The model was then used to simulate the creep behavior of two microcomposites for which test data was available in the literature (Rugg et al., 1999). The effects of fiber volume fraction, fiber-matrix creep mismatch ratio, and time-dependent constituent load transfer were investigated. The effects of time-dependent constituent load transfer on as-produced thermal residual stresses and the room temperature proportional limit stress was also investigated using a previously developed progressive damage model (Liu and Arnold, 2011) to simulate the initiation and propagation of matrix damage. Simulation results were in good agreement with experimental data available in the literature, when available, and provide valuable insight into the mechanisms governing creep in CMCs.

5.2 Future Work

While the research presented in this dissertation provides an improved understanding of some of the nonintuitive mechanisms governing the nonlinear constitutive behavior of PMCs under high strain rate loading and CMCs under sustained loading at elevated temperatures, further developments are necessary to maximize the fidelity, effectiveness, and predictive capability of the techniques and methods described herein. Additional study and future work is essential to provide a more thorough understanding of the complex interplay between deformation, progressive damage, and failure mechanisms such that these mechanisms can be better exploited to meet the multiple, and often conflicting, design and certification criteria of advanced PMC and CMC structures. The future research directions are summarized in the remainder of this section.

The predictions of adiabatic temperature rises in polymers and PMCs presented in Chapters 2 and 3 can be improved by approximating the inelastic heat fraction using neat resin mechanical test data for which thermal measurements are available. Since the inelastic heat fraction is likely nonconstant, its dependence upon on various quantities, such as strain, strain rate, temperature, and stress state, should also be investigated. At moderate rates of deformation, where neither isothermal or adiabatic assumptions hold, coupled thermodynamic conditions must be considered. The fully adiabatic ($\beta = 1$) simulations considered in in Chapters 2 and 3 should therefore be viewed as upper bounds on the possible deformation-induced temperature rises. For moderate deformation rates it is necessary to consider the conduction term in the heat energy equation. Lastly, further improvements can be made by considering the thermoelastic term in the heat energy equation, which will allow modeling thermoelastic cooling/heating.

The polymer and PMC related work in Chapters 2 and 3 can be further improved by developing a thermodynamically consistent progressive damage and failure model for the polymer matrix. Since polymers are pressure-dependent and generally more ductile at low deformation rates and high temperatures, the matrix progressive damage law will likely need to be strain rate, temperature, and pressure dependent. The damage model could be assumed to be isotropic and therefore employ one or multiple scalar damage variables, as well as a suitable set of internal state variables to control progressive stiffness reduction. In addition to the deformation-induced heating due to plastic dissipation considered in this dissertation, the dissipated energy associated with the progression of damage may also result in notable heating in the material at high strain rates. It is therefore necessary to account for dissipated energy due to progressive stiffness reduction resulting from damage. The damage model can be calibrated using data from cyclic load-unload tests conducted on neat resin to partition material nonlinearity due to inelasticity and damage. If it is desirable to account for the nonlinear unloading typically observed in polymers, it will likely be necessary to also consider viscoelasticity. The viscoelastic behavior can be characterized using data from DMA tests, creep tests, relaxation tests, as well as cyclic tests conducted on the neat polymer of interest.

The micromechanics simulations presented in Chapters 3 and 4 employed relatively simple idealized doubly-periodic microscale RUCs, which represent the effective constitutive behavior of tows in a woven or braided composite. The periodicity in these micromechanics simulations implies a perfectly ordered intratow fiber packing arrangement, which is not the case for the tows in actual composites (see Figure 3.3-4). The subcell-based approach used in Chapter 3 to approximate the heterogeneity of the

considered T700/E862 triaxially braided PMC also represents an idealized approximation of the true braid architecture (Figure 3.3-3). Particularly, the approximation lacks bias tow continuity since each mesoscale subcell region is approximated as a laminated composite. The fidelity of both the standalone micromechanics simulations (Chapters 3 and 4) and the triaxially braided PMC FE simulations (Chapter 3) could therefore be improved by considering more realistic high-fidelity RUCs, or representative volume elements (RVEs). These RVEs can be constructed using images of intratow regions (e.g., Figure 3.3-4) and braided or woven composite cross sections (e.g., Figure 3.3-3) obtained via optical microscopy. These images can then be used to construct periodic RVEs of varying levels of architectural variability (i.e., idealized and as-produced), which can subsequently be meshed and used for micromechanical analyses. Micromechanical analyses of the aforementioned RVEs should be conducted using either a higher-order micromechanics theory with normal-shear coupling, such as HFGMC, or using fully numerical FE-based micromechanics simulations with periodic boundary conditions.

In Chapter 3, the volume fractions of UD plies in the discretization of the triaxially braided PMC mesoscale RUC were determined via microscopy and microscopy-informed assumptions. Particularly, the volume fraction of UD plies corresponding to the axial tows were assumed equal to the mean axial tow fiber volume fraction determined through optical microscopy (Figure 3.3-4). Additionally, while constituent material properties used in the work presented in this dissertation were assumed to be deterministic, these properties will vary spatially in a real composite. Architectural parameters such as the local tow fiber volume fraction in woven/braided composites will also vary spatially (e.g., between individual tows in a composite and along a given tow). The effects of variability in

constituent material properties and geometric parameters on the effective composite constitutive behavior is a critical consideration that must be addressed in future research. This can be done by considering the fiber volume fraction and constituent material properties to be random variables, determining suitable probably distributions for these random variables (e.g., Figure 3.3-5), and sampling from the distributions using an appropriate technique, such as Monte Carlo or Latin Hypercube sampling. This would result in a family or envelope of stress-strain curves for a given applied loading rather than a single curve as in the deterministic case. Consideration of material property and architectural/geometric variability would also be beneficial for calibration against test data, where variability is expected for repeated tests of the same type.

While the UD creep simulations presented in Chapter 4 are a necessary first step to better understand the complex time-dependent constituent load transfer governing macroscopic CMC response, it is essential to consider woven architectures typically used in high-temperature CMC structural components. Additionally, due to the presence of moisture in the service environment of hot-gas-path CMC turbine components, oxidative degradation is a major life-limiting mechanism. Progressive matrix cracking creates pathways for gaseous oxidants to enter the CMC and attack the constituent materials. The effects of this oxidative degradation are known to be most critical at intermediate temperatures whereas, at elevated temperatures, oxidation products have been reported to seal matrix cracks and prevent further ingress of gaseous oxidants. A comprehensive model for the elevated temperature constitutive behavior of CMCs therefore must account for the coupling between oxidative degradation and damage, including mechanisms responsible for temperature-dependent mechanistic changes.

REFERENCES

Aboudi, J. (1989). Micromechanical analysis of composites by the method of cells.

Aboudi, J. (1995). Micromechanical analysis of thermo-inelastic multiphase short-fiber composites. Composites Engineering, 5(7), 839-850.

Aboudi, J., Arnold, S. M., & Bednarcyk, B. A. (2012). Micromechanics of composite materials: a generalized multiscale analysis approach. Butterworth-Heinemann.

Allen, D. H. (1991). Thermomechanical Coupling in Inelastic Solids. Applied Mechanics Reviews, 44(8), 361.

Almansour, A. S., & Morscher, G. N. (2019). Testing and Modeling of Creep Behavior of Different Fiber Content and Type Single-Tow CVI-SiC_f/SiC Minicomposites. SiC Minicomposites. https://ssrn.com/abstract=3310269.

Arnold, S. M., Bednarcyk, B. A., & Aboudi, J. (2004). Comparison of the computational efficiency of the original versus reformulated high-fidelity generalized method of cells. NASA/TM–213438, National Aeronautics and Space Administration, Washington, DC.

Arnold, S. M., Lerch, B., & Ricks, T. M. (2019). Interpretation of Experimental Tensile Test Results and Its Implication on Damage Modeling. In *AIAA Scitech 2019 Forum* (p. 1965).

Arruda, E. M., Boyce, M. C., & Jayachandran, R. (1995). Effects of strain rate, temperature and thermomechanical coupling on the finite strain deformation of glassy polymers. *Mechanics of Materials*, *19*(2-3), 193-212.

ASTM D8101 / D8101M-17, Standard Test Method for Measuring the Penetration Resistance of Composite Materials to Impact by a Blunt Projectile, ASTM International, West Conshohocken, PA, 2017, www.astm.org.

Bailey, R. W. (1935). The utilization of creep test data in engineering design. *Proceedings of the Institution of Mechanical Engineers*, *131*(1), 131-349.

Bansal, Y., & Pindera, M. J. (2004). Testing the predictive capability of the high-fidelity generalized method of cells using an efficient reformulation. NASA CR, 213043, 2004, National Aeronautics and Space Administration, Washington, DC.

Bednarcyk, B. A., & Arnold, S. M. (2002). MAC/GMC 4.0 User's Manual: Keywords Manual. National Aeronautics and Space Administration, Washington, DC.

Bednarcyk, B. A., Aboudi, J., Arnold, S. M., & Pineda, E. J. (2019). A multiscale two-way thermomechanically coupled micromechanics analysis of the impact response of thermo-elastic-viscoplastic composites. International Journal of Solids and Structures, 161, 228-242.

Begley, M. R., Evans, A. G., & McMeeking, R. M. (1995). Creep rupture in ceramic matrix composites with creeping fibers. Journal of the Mechanics and Physics of Solids, 43(5), 727-740. https://doi.org/10.1016/0022-5096(95)00006-5

Belytschko, T., & Bindeman, L. P. (1993). Assumed strain stabilization of the eight node hexahedral element. Computer Methods in Applied Mechanics and Engineering, 105(2), 225-260.

Bessho, T., Ogasawara, T., Aoki, T., Ishikawa, T., & Ochi, Y. (2005). Transient creep behavior of a plain woven SiC fiber/SiC matrix composite. JSME International Journal Series A Solid Mechanics and Material Engineering, 48(4), 210-214. https://doi.org/10.1299/jsmea.48.210

Bhattachar, V. S., & Stouffer, D. C. (1993). Constitutive Equations for the Thermomechanical Response of René 80: Part 1—Development From Isothermal Data. Journal of Engineering Materials and Technology, 115(4), 351-357.

Bhattachar, V.S. (1991). A unified constitutive model for the thermomechanical fatigue response of a nickel base superalloy Rene 80. Ph.D. Dissertation, University of Cincinnati.

Blinzler, B. J. (2012). Systematic approach to simulating impact for triaxially braided composites. Ph.D. Dissertation, University of Akron.

Bodner, S. R. (2001). Unified plasticity for engineering applications. (Vol. 47). Springer Science & Business Media.

Bodner, S., & Partom, Y. (1975). Constitutive equations for elastic-viscoplastic strain-hardening materials. Journal of Applied Mechanics, 42(2), 385-389.

Borkowski, L., & Chattopadhyay, A. (2015). Multiscale model of woven ceramic matrix composites considering manufacturing induced damage. Composite Structures, 126, 62-71.

Brockmeyer, J.W., 1992, June. Ceramic matrix composite applications in advanced liquid fuel rocket engine turbomachinery. In ASME 1992 International Gas Turbine and Aeroengine Congress and Exposition (pp. V005T13A002-V005T13A002). American Society of Mechanical Engineers. https://doi.org/10.1115/92-GT-316

Carney, K., Pereira, M., Kohlman, L., Goldberg, R., Envia, E., Lawrence, C., and Emmerling, W. (2013). Weight Assessment for Fuselage Shielding on Aircraft With Open-Rotor Engines and Composite Blade Loss.

Cater, C. R., Xiao, X., Goldberg, R. K., & Kohlman, L. W. (2014). Single ply and multi-ply braided composite response predictions using modified subcell approach. Journal of Aerospace Engineering, 28(5), 04014117.

Cater, C., Xiao, X., Goldberg, R. K., & Kohlman, L. W. (2015). Experimental and Numerical Analysis of Triaxially Braided Composites Utilizing a Modified Subcell

Modeling Approach. NASA/TM—2015-218814, National Aeronautics and Space Administration, Washington, DC.

Chamis, C. C. (1984). Simplified Composite Micromechanics Equations for Strength, Fracture Toughness, Impact Resistance and Environmental Effects. NASA/TM–83696, National Aeronautics and Space Administration, Washington, DC.

Chamis, C. C., & Hopkins, D. A. (1988). Thermoviscoplastic nonlinear constitutive relationships for structural analysis of high-temperature metal matrix composites. In Testing Technology of Metal Matrix Composites. ASTM International.

Chatiri, M., Güll, T., & Matzenmiller, A. (2009, May). An assessment of the new LS-DYNA layered solid element: basics, patch simulation and its potential for thick composite structure analysis. In 7th European LS-DYNA Conference, Salzburg (pp. 1-12).

Chen, J. K., Allahdadi, F. A., & Sun, C. T. (1997). A quadratic yield function for fiber-reinforced composites. *Journal of composite materials*, *31*(8), 788-811.

Chen, J. L., & Sun, C. T. (1993). A plastic potential function suitable for anisotropic fiber composites. Journal of Composite Materials, 27(14), 1379-1390.

Cheng, J., & Binienda, W. K. (2008). Simplified braiding through integration points model for triaxially braided composites. Journal of Aerospace Engineering, 21(3), 152-161.

Chiou, S. T., Tsai, H. L., & Lee, W. S. (2007). Effects of strain rate and temperature on the deformation and fracture behaviour of titanium alloy. Materials transactions, 48(9), 2525-2533.

Chou, S. C., Robertson, K. D., & Rainey, J. H. (1973). The effect of strain rate and heat developed during deformation on the stress-strain curve of plastics. *Experimental mechanics*, *13*(10), 422-432.

Chow, C. L., & Lu, T. J. (1989). On evolution laws of anisotropic damage. Engineering Fracture Mechanics, 34(3), 679-701.

Cousigné, O., Moncayo, D., Coutellier, D., Camanho, P., & Naceur, H. (2014). Numerical modeling of nonlinearity, plasticity and damage in CFRP-woven composites for crash simulations. Composite Structures, 115, 75-88.

Curtin, W. A. (1991). Theory of Mechanical Properties of Ceramic-Matrix Composites. J. Am. Ceram. Soc., 74(11), 2837e2845.

Daniel, I. M., Ishai, O., Daniel, I. M., & Daniel, I. (2006). *Engineering mechanics of composite materials* (Vol. 1994). New York: Oxford university press.

Davies E, Hunter S (1963) The dynamic compression testing of solids by the method of the split Hopkinson pressure bar. J Mech Phys Solids 11(3):155–179.

Dorn, J. E. (1955). Some fundamental experiments on high temperature creep. *Journal of the Mechanics and Physics of Solids*, *3*(2), 85-116. https://doi.org/10.1016/0022-5096(55)90054-5

Faria, R., Oliver, J., & Cervera, M. (1998). A strain-based plastic viscous-damage model for massive concrete structures. International journal of solids and structures, 35(14), 1533-1558.

Feyel, F. (1999). Multiscale FE2 elastoviscoplastic analysis of composite structures. Computational Materials Science, 16(1-4), 344-354.

Fohey, W.R., Battison, J.M. and Nielsen, T.A., 1995, January. Ceramic composite turbine engine component evaluation. In Proceedings of the 19th Annual Conference on Composites, Advanced Ceramics, Materials, and Structures—A: Ceramic Engineering and Science Proceedings (pp. 459-466). Hoboken, NJ, USA: John Wiley & Sons, Inc. https://doi.org/10.1002/9780470314715.ch50

Garg, M., Mulliken, A. D., & Boyce, M. C. (2008). Temperature rise in polymeric materials during high rate deformation. Journal of Applied Mechanics, 75(1), 011009.

Gauthier, W., & Lamon, J. (2009). Delayed failure of Hi-Nicalon and Hi-Nicalon S multifilament tows and single filaments at intermediate temperatures (500–800° C). Journal of the American Ceramic Society, 92(3), 702-709. https://doi.org/10.1111/j.1551-2916.2009.02924.x

Gilat, A., Goldberg, R. K., & Roberts, G. D. (2007). Strain rate sensitivity of epoxy resin in tensile and shear loading. Journal of Aerospace Engineering, 20(2), 75-89.

Goldberg, R. K., Blinzler, B. J., & Binienda, W. K. (2012). Modification of a Macromechanical Finite Element–Based Model for Impact Analysis of Triaxially Braided Composites. Journal of Aerospace Engineering, 25(3), 383-394.

Goldberg, R. K., Roberts, G. D., & Gilat, A. (2005). Implementation of an associative flow rule including hydrostatic stress effects into the high strain rate deformation analysis of polymer matrix composites. Journal of Aerospace Engineering, 18(1), 18-27.

Gowayed, Y., Ojard, G. (2020). Ceramic Matrix Composites: Characterization Analysis, and Applications. DEStech Publications, Inc.

Gowayed, Y., Ojard, G., Chen, J., Morscher, G., Miller, R., Santhosh, U., ... & John, R. (2011). Accumulation of time-dependent strain during dwell-fatigue experiments of iBN-Sylramic melt infiltrated SiC/SiC composites with and without holes. *Composites Part A: Applied Science and Manufacturing*, *42*(12), 2020-2027. https://doi.org/10.1016/j.compositesa.2011.09.008

Griffin Jr, O. H., Kamat, M. P., & Herakovich, C. T. (1981). Three-dimensional inelastic finite element analysis of laminated composites. Journal of Composite Materials, 15(6), 543-560.

Guo, Y. (2000). Eight node solid element for thick shell simulations. In 6th International LS-DYNA conference, Detroit.

Hallquist, J. O. (2006). LS-DYNA theory manual. Livermore software Technology corporation, 3, 25-31.

Hill, R. (1948). A theory of the yielding and plastic flow of anisotropic metals. *Proceedings of the Royal Society of London. Series A. Mathematical and Physical Sciences*, *193*(1033), 281-297.

Holmes, J. W., & Chermant, J. L. (1993). CREEP BEHAVIOUR OF FIBRE-REINFORCED CERAMIC MATRIX COMPOSITE. In High Temperature Ceramic Matrix Composites. Proc. 6 th European Conf. on Composite Materials. Bordeaux (Vol. 20, No. 24).

Holmes, J.W. and Wu, X., 1995. Elevated temperature creep behavior of continuous fiber-reinforced ceramics. In High Temperature Mechanical Behaviour of Ceramic Composites (pp. 193-259). Butterworth-Heinemann. https://doi.org/10.1016/B978-075069399-8/50006-2

Ivanov, I., & Tabiei, A. (2004). Loosely woven fabric model with viscoelastic crimped fibres for ballistic impact simulations. International journal for numerical methods in engineering, 61(10), 1565-1583.

Johnston, J. P., Pereira, J. M., Ruggeri, C. R., & Roberts, G. D. (2018). High-speed infrared thermal imaging during ballistic impact of triaxially braided composites. Journal of Composite Materials, 52(25), 3549-3562.

Jordan, J. L., Foley, J. R., & Siviour, C. R. (2008). Mechanical properties of Epon 826/DEA epoxy. *Mechanics of Time-Dependent Materials*, *12*(3), 249-272.

Kawai, M., Zhang, J. Q., Xiao, Y., & Hatta, H. (2010). Modeling of tension-compression asymmetry in off-axis nonlinear rate-dependent behavior of unidirectional carbon/epoxy composites. Journal of composite materials, 44(1), 75-94.

Kenaga, D., Doyle, J. F., & Sun, C. T. (1987). The characterization of boron/aluminum composite in the nonlinear range as an orthotropic elastic-plastic material. Journal of Composite Materials, 21(6), 516-531.

Kendall, M. J., & Siviour, C. R. (2013). Experimentally simulating adiabatic conditions: approximating high rate polymer behavior using low rate experiments with temperature profiles. *Polymer*, *54*(18), 5058-5063.

Kohlman, L. W. (2012). Evaluation of test methods for triaxial braid composites and the development of a large multiaxial test frame for validation using braided tube specimens. Ph.D. Dissertation, University of Akron.

Kolling, S., Haufe, A., Feucht, M., & Du Bois, P. A. (2005). SAMP-1: A Semi-Analytical Model for the Simulation of Polymers. In: 4th German LS-DYNA Forum (LS-DYNA Anwenderforum), Bamberg, Germany, 20-21 October 2005.

Kolsky H (1949) An investigation of the mechanical properties of materials at very high rates of loading. Proc Phys Soc Lond Sect B 62(11):676–700.

Kraus, H., Creep Analysis, John Wiley, 1980.

Landau, H. G., Weiner, J. H., & Zwicky Jr, E. E. (1960). Thermal stress in a viscoelastic-plastic plate with temperature-dependent yield stress.

Lara-Curzio, E. (1999). Analysis of oxidation-assisted stress-rupture of continuous fiber-reinforced ceramic matrix composites at intermediate temperatures. *Composites Part A: Applied Science and Manufacturing*, *30*(4), 549-554. https://doi.org/10.1016/S1359-835X(98)00148-1

Li, X., Binienda, W. K., and Littell, J. D. (2009). "Methodology for Impact Modeling of Triaxial Braided Composites Using Shell Elements." J Aerosp Eng, 22, 310–317.

Li, Z., & Lambros, J. (2001). Strain rate effects on the thermomechanical behavior of polymers. International Journal of solids and structures, 38(20), 3549-3562.

Littell, J. (2008). The experimental and analytical characterization of the macromechanical response for triaxial braided composite materials. Ph.D. Dissertation, University of Akron.

Littell, J. D., Ruggeri, C. R., Goldberg, R. K., Roberts, G. D., Arnold, W. A., & Binienda, W. K. (2008). Measurement of epoxy resin tension, compression, and shear stress–strain curves over a wide range of strain rates using small test specimens. *Journal of Aerospace Engineering*, *21*(3), 162-173.

Liu, K. C. (2011). Micromechanics Based Multiscale Modeling of the Inelastic Response and Failure of Complex Architecture Composites. Ph.D. Dissertation, Arizona State University.

Liu, K. C., & Arnold, S. M. (2011). *Impact of material and architecture model parameters on the failure of woven ceramic matrix composites (CMCs) via the multiscale generalized method of cells*. NASA/TM—2011-217011. National Aeronautics and Space Administration, Washington, DC.

Liu, K. C., Chattopadhyay, A., & Arnold, S. M. (2011). Impact of material and architecture model parameters on the failure of woven CMCs via the multiscale generalized method of cells. *Developments in strategic materials and computational design II: ceramic engineering and science proceedings*, *32*, 175-192.

Liu, K. C., Chattopadhyay, A., Bednarcyk, B., & Arnold, S. M. (2011). Efficient multiscale modeling framework for triaxially braided composites using generalized method of cells. Journal of Aerospace Engineering, 24(2), 162-169.

Liu, K. C., & Arnold, S. M. (2013). Stochastic Nonlinear Response of Woven CMCs. NASA/TM—2013-217859, National Aeronautics and Space Administration, Washington, DC.

Matzenmiller, A. L. J. T. R., Lubliner, J., & Taylor, R. L. (1995). A constitutive model for anisotropic damage in fiber-composites. *Mechanics of materials*, *20*(2), 125-152.

Menard, K. P., & Menard, N. R. (2020). *Dynamic mechanical analysis*. CRC press.

Meyers, M. A. (1994). *Dynamic behavior of materials*. John wiley & sons.

Mital, S. K., Arnold, S. M., Murthy, P. L., Bednarcyk, B. A., & Pineda, E. J. (2018). Modeling of Time-Dependent Strength Degradation of SiC/SiC Ceramic Matrix Composites via MAC/GMC Computer Code.

Morscher, G. N., Hurst, J., & Brewer, D. (2000). Intermediate-temperature stress rupture of a woven Hi-Nicalon, BN-interphase, SiC-matrix composite in air. *Journal of the American Ceramic Society*, *83*(6), 1441-1449. https://doi.org/10.1111/j.1151-2916.2000.tb01408.x

Mulliken AD, Boyce MC. Mechanics of the rate-dependent elastic–plastic deformation of glassy polymers from low to high strain rates. Int J Solids Struct 2006;43(5):1331–56.

Murthy, P. L. (1986). Integrated composite analyzer (ICAN): users and programmers manual. Defense Technical Information Center.

Naslain, R. and Christin, F., 2003. SiC-matrix composite materials for advanced jet engines. MRS bulletin, 28(9), pp.654-658. https://doi.org/10.1557/mrs2003.193

Naslain, R., 2004. Design, preparation and properties of non-oxide CMCs for application in engines and nuclear reactors: an overview. Composites Science and Technology, 64(2), pp.155-170. https://doi.org/10.1016/S0266-3538(03)00230-6

Norton, F. H. (1929). The creep of steel at high temperatures (No. 35). McGraw-Hill Book Company, Incorporated.

Nutting, P. G. (1921). A new general law of deformation. Journal of the Franklin Institute, 191(5), 679-685.

Nutting, P. G. (1943). A general stress-strain-time formula. *Journal of the Franklin Institute*, *235*(5), 513-524.

Ohnabe, H., Masaki, S., Onozuka, M., Miyahara, K. and Sasa, T., 1999. Potential application of ceramic matrix composites to aero-engine components. Composites Part A: Applied Science and Manufacturing, 30(4), pp.489-496. https://doi.org/10.1016/S1359-835X(98)00139-0

Paley, M., & Aboudi, J. (1992). Micromechanical analysis of composites by the generalized cells model. Mechanics of materials, 14(2), 127-139. https://doi.org/10.1016/0167-6636(92)90010-B

Pan, Z., Sun, B., Shim, V. P., & Gu, B. (2016). Transient heat generation and thermo-mechanical response of epoxy resin under adiabatic impact compressions. International Journal of Heat and Mass Transfer, 95, 874-889.

Penny, R. K., & Marriott, D. L. (2012). Design for creep. Springer Science & Business Media.

Pereira, J. M., Revilock, D. M., Ruggeri, C. R., Roberts, G. D., Kohlman, L. W., & Miller, S. G. (2016). The effects of hygrothermal aging on the impact penetration resistance of triaxially braided composites.

Pereira, J. M., Roberts, G. D., Ruggeri, C. R., Gilat, A., & Matrka, T. (2010). Experimental techniques for evaluating the effects of aging on impact and high strain rate properties of triaxial braided composite materials.

Pindera, M. J., & Bednarcyk, B. A. (1999). An efficient implementation of the generalized method of cells for unidirectional, multi-phased composites with complex microstructures. Composites part B: engineering, 30(1), 87-105.

Pineda, E. J., Bednarcyk, B. A., Mital, S. K., & Arnold, S. M. (2015). The effect of stochastically varying creep parameters on residual stresses in ceramic matrix composites. In *56th AIAA/ASCE/AHS/ASC Structures, Structural Dynamics, and Materials Conference* (p. 0389).

Pineda, E. J., Fassin, M., Bednarcyk, B. A., Reese, S., & Simon, J. W. (2017, July). Comparison of Multiscale Method of Cells-Based Models for Predicting Elastic Properties of Filament Wound C/C-SiC. In Proceedings of the American Society for Composites—Thirty-second Technical Conference.

Poulain, X. (2010). On the thermomechanical behavior of epoxy polymers: Experiments and modeling. Ph.D. Dissertation, Texas A&M University, College Station, TX.

Poulain, X., Benzerga, A. A., & Goldberg, R. K. (2014). Finite-strain elasto-viscoplastic behavior of an epoxy resin: Experiments and modeling in the glassy regime. *International Journal of Plasticity*, *62*, 138-161.

Poulain, X., Kohlman, L. W., Binienda, W., Roberts, G. D., Goldberg, R. K., & Benzerga, A. A. (2013). Determination of the intrinsic behavior of polymers using digital image correlation combined with video-monitored testing. *International Journal of Solids and Structures*, *50*(11-12), 1869-1878.

Reuss, A. (1929). Berechnung der fließgrenze von mischkristallen auf grund der plastizitätsbedingung für einkristalle. ZAMM-Journal of Applied Mathematics and Mechanics/Zeitschrift für Angewandte Mathematik und Mechanik, 9(1), 49-58.

Revilock, D., personal communication, December 11, 2017.

Richeton, J., Ahzi, S., Vecchio, K. S., Jiang, F. C., & Makradi, A. (2007). Modeling and validation of the large deformation inelastic response of amorphous polymers over a wide range of temperatures and strain rates. *International journal of solids and structures*, *44*(24), 7938-7954.

Rittel, D. (1999). On the conversion of plastic work to heat during high strain rate deformation of glassy polymers. *Mechanics of Materials*, *31*(2), 131-139.

Roberts, G. D., Pereira, J. M., Braley, M. S., Dorer, J. D., & Watson, W. R. (2009). Design and testing of braided composite fan case materials and components. NASA/TM—2009-215811, National Aeronautics and Space Administration, Washington, DC.

Robinson, D. N., & Binienda, W. K. (2001). Model of viscoplasticity for transversely isotropic inelastically compressible solids. *Journal of engineering mechanics*, *127*(6), 567-573.

Robinson, D. N., Tao, Q. and Verrilli, M. J. (1994). A hydrostatic stress-dependent anisotropic model of viscoplasticity. NASA/TM–106525, National Aeronautics and Space Administration, Washington, DC.

Rowghanian P., Hoa S.V. (2011). Improvement of Temperature Distribution Across Thick Thermoset Composite Laminates Using Carbon Nanotubes. In: American Society for Composites 26th Technical Conference Proceedings (ASC/26), Montreal, Quebec, Canada, 26-28 September 2011. p. 188-201.

Rugg, K. L. (1997). *Mechanical behavior at high temperatures of single fiber microcomposites*. Ph.D. Dissertation, The Pennsylvania State University.

Rugg, K.L., Tressler, R.E., Bakis, C.E. and Lamon, J., 1999. Creep of SiC–SiC microcomposites. Journal of the European ceramic society, 19(13-14), pp.2285-2296. https://doi.org/10.1016/S0955-2219(99)00118-1.

Santhosh, U., & Ahmad, J. (2013). A model for estimating nonlinear deformation and damage in ceramic matrix composites. Journal of Composite Materials, 47(10), 1257-1272. https://doi.org/10.1177/0021998312446823

Santhosh, U., Ahmad, J., Kalarikkal, S., Ojard, G., & Gowayed, Y. (2018). Time-Dependent Deformation and Damage Modeling of a SiC/SiC Composite. Journal of Aerospace Engineering, 31(6), 04018086. https://doi.org/10.1061/(ASCE)AS.1943-5525.0000921

Siviour, C. R., & Jordan, J. L. (2016). High strain rate mechanics of polymers: a review. *Journal of Dynamic Behavior of Materials*, *2*(1), 15-32.

Skinner, T., & Chattopadhyay, A. (2021). Multiscale temperature-dependent ceramic matrix composite damage model with thermal residual stresses and manufacturing-induced damage. *Composite Structures*, *268*, 114006.

Skrzypek, J. & Hetnarski, R. (1993). Plasticity and Creep Theory Examples and Problems. Boca Raton, FL: CRC Press.

Spriet, P. and Habarou, G., 1996, June. Applications of continuous fiber reinforced ceramic composites in military turbojet engines. In ASME 1996 International Gas Turbine and Aeroengine Congress and Exhibition (pp. V005T13A008-V005T13A008). American Society of Mechanical Engineers. https://doi.org/10.1115/96-GT-284

Spriet, P., 2014. CMC applications to gas turbines. Ceramic Matrix Composites: Materials, Modeling and Technology, pp.591-608. https://doi.org/10.1002/9781118832998.ch21

Spurgeon WA. Thermal conductivities of some polymers and composites (No. ARL-TR-8298). US Army Research Laboratory Aberdeen Proving Ground United States; 2018.

Staehler, J.M. and Zawada, L.P., 2000. Performance of four ceramic-matrix composite divergent flap inserts following ground testing on an F110 turbofan engine. Journal of the American Ceramic Society, 83(7), pp.1727-1738. https://doi.org/10.1111/j.1151-2916.2000.tb01457.x

Stouffer, D. C., & Dame, L. T. (1996). *Inelastic deformation of metals: models, mechanical properties, and metallurgy*. John Wiley & Sons.

Sullivan, R. M. (2016). Time-dependent stress rupture strength of Hi-Nicalon fiber-reinforced silicon carbide composites at intermediate temperatures. *Journal of the European Ceramic Society*, *36*(8), 1885-1892.

Sun, C. T., & Chen, J. L. (1989). A simple flow rule for characterizing nonlinear behavior of fiber composites. *Journal of Composite Materials*, *23*(10), 1009-1020.

Tabiei, A., & Ivanov, I. (2002). Computational micro-mechanical model of flexible woven fabric for finite element impact simulation. *International journal for numerical methods in engineering*, *53*(6), 1259-1276.

Thiruppukuzhi, S. V., & Sun, C. T. (1998). Testing and modeling high strain rate behavior of polymeric composites. *Composites Part B: Engineering*, *29*(5), 535-546.

Trojanowski, A., Ruiz, C., & Harding, J. (1997). Thermomechanical properties of polymers at high rates of strain. *Le Journal de Physique IV*, *7*(C3), C3-447.

Varghese AG, Batra RC. Constitutive equations for thermomechanical deformations of glassy polymers. Int J Solids Struct 2009;46(22):4079–94.

Voight, W. (1887). Theoretische Studien uber die Elasticitatsverhaltnisse des Krystalle, I, II. *Abh. Ges. Wiss., Gottingen*.

Walley, S. M., Field, J. E., Pope, P. H., & Safford, N. A. (1989). A study of the rapid deformation behaviour of a range of polymers. *Philosophical Transactions of the Royal Society of London. Series A, Mathematical and Physical Sciences*, *328*(1597), 1-33.

Wang J, Xiao Y. (2017a). Some improvements on Sun–Chen's one-parameter plasticity model for fibrous composites–Part I: constitutive modelling for tension–compression asymmetry response. J Compos Mater 2017;51(3):405–18.

Wang, J., & Xiao, Y. (2017b). Some improvements on Sun-Chen's one-parameter plasticity model for fibrous composites–Part II: Finite element method implementation and applications. *Journal of Composite Materials*, *51*(4), 533-545.

Weeks, C. A., & Sun, C. T. (1998). Modeling non-linear rate-dependent behavior in fiber-reinforced composites. *Composites Science and Technology*, *58*(3-4), 603-611.

Xiao, X., Kia, H. G., & Gong, X. J. (2011). Strength prediction of a triaxially braided composite. *Composites Part A: Applied Science and Manufacturing*, *42*(8), 1000-1006.

Xu, W., Zok, F. W., & McMeeking, R. M. (2014). Model of oxidation-induced fiber fracture in SiC/SiC composites. *Journal of the American Ceramic Society*, *97*(11), 3676-3683. https://doi.org/10.1111/jace.13180

Yokozeki, T., Ogihara, S., Yoshida, S., & Ogasawara, T. (2007). Simple constitutive model for nonlinear response of fiber-reinforced composites with loading-directional dependence. *Composites Science and Technology*, *67*(1), 111-118.

Zhou, Y., Wang, Y., Xia, Y., & Jeelani, S. (2010). Tensile behavior of carbon fiber bundles at different strain rates. *Materials Letters*, *64*(3), 246-248.